Spectroscopy of ^{250}Fm using Tagging Techniques

Thesis submitted in accordance with the requirements of the University of Liverpool for the degree of Doctor in Philosophy

by

Danielle C. Rostron

Oliver Lodge Laboratory

2009

Abstract

The fermi level of ^{250}Fm lies close to the shell gaps predicted for deformed nuclei around Z=100 and N=150. Observing excitations of deformed nuclei in this region provides information about the single-particle energies around the predicted gap. This not only advances the shell gap calculations for deformed nuclei, but also constrains the theories for spherical nuclei close to the shell closures.

The isomers of ^{250}Fm are investigated experimentally using tagging techniques. An experiment was performed at the University of Jyväskylä Accelerator Laboratory, Finland. γ rays were detected at the target using the JUROGAM array whilst the GREAT spectrometer is situated at the focal plane of the RITU separator. Recoil-isomer tagging identified two ^{250}Fm isomers with half-lives 1.93(5) s and 9(1) μs. Coincidences between internal conversion electrons from isomeric decays and γ decays uncovered two excited bands of ^{250}Fm with K^{π}=2^{-} and 8^{-}. The 1.93(5) s isomer is found to be the band head of the K^{π}=8^{-} band, which decays directly to the ground state and via the K^{π}=2^{-} band.

Decays from the isomer and K^{π}=2^{-} are observed using recoil-isomer tagging of γ rays at the focal plane, whilst the K^{π}=8^{-} band is explored promptly at the target position. Both K^{π}=2^{-} and 8^{-} structures are found to be signature-split rotational bands. Furthermore, dipole and stretched E2 multipolarity γ rays are observed, enabling the intensity ratios of γ decays from one level to be determined. These ratios strongly depend on the internal structure of the nucleus, especially the gyromagnetic ratio, g_K, of the quasiparticles that cause the excitation. The relationship between the γ-ray intensity ratio and g_K is explored. The intensity ratios from the experiment are compared to calculated intensity ratios that would be expected for two-quasiparticle excitations with K^{π}=2^{-} and K^{π}=8^{-} bands. The experimental intensity ratios support the assignment of the K^{π}=8^{-} as a two-neutron quasiparticle excitation with configuration $\{\frac{7}{2}^{+}[624]_{\nu} \otimes \frac{9}{2}^{-}[734]_{\nu}\}^{8-}$. The K^{π}=2^{-} band is expected

to have a mixed configuration, with an octupole vibration and quasiparticle excitation able to produce a $K^{\pi}=2^{-}$ band. However, the intensity ratios measured in this study show that the two-neutron quasiparticle excitation $\{\frac{9}{2}^{-}[734]_{\nu} \otimes \frac{5}{2}^{+}[622]_{\nu}\}^{2-}$ is dominant. The single-particle assignments provide further evidence that the deformed shell gaps exist at Z=100 and N=152.

To my grandmother, Norah Marie Rostron (1924–2007)

Acknowledgments

First and foremost, thank you to Prof. Rodi Herzberg for his guidance and support, especially whilst writing my thesis. Thank you to all the academic and computing staff in the Nuclear Physics Group at the University of Liverpool for their help, with special thanks to Dr. Dave Joss for his encouragement. I would also like to acknowledge Prof. P.J. Nolan for giving me this opportunity at the University of Liverpool and the EPSRC studentship for providing financial support.

Many thanks to everyone at the Physics Department of the University of Jyväskylä for all their help on experiments and for making me feel so welcome - Kiitos! Special thanks to Dr. Paul Greenlees and Steffen Ketelhut for their collaboration and assistance with this research.

A big thank you to Dr. Marcus Scheck, Dr. Tuomas Grahn and Dr. Sarah Rigby for their proof-reading and advice.

Thanks to all the Herzberg students and postdocs over the years for their help with my analysis and their good company on experiments, especially Craig Gray-Jones, Philippos Papadakis and Eddie Parr for sharing my birthdays in Jyväskylä with me.

Thanks to all my fellow Nuclear Physics students for all the hilarity and obscure conversation topics. Special thanks to the girls - Suzanne Critell, Heidi Watkins, Laura Nelson and Sam Colosimo - for all those great nights out, and to my year-mates Laura Bianco, Alex Grint, Ben Pietras and Jimmy Thomson for sharing the best and worst bits with me.

Thank you to my parents, Angela and Dave, for supporting me in whatever I choose to do. I am also very grateful to my sister, Eve, and brother, Ben, for always being on hand to offer their support.

Finally, my biggest and most heart-felt thanks goes to Paul, who has supported me more than anyone over the past 3 and a half years.

Contents

List of Figures

List of Tables

Chapter 1

Introduction

Over recent years, experimental and theoretical studies have been exploring the limits of nuclear structure. One of the most fundamental questions is where the limits of nuclear structure lie. At the extremes of mass number A and charge Z, lie the superheavy nuclei (SHN), which have been studied experimentally at GSI (Germany), RIKEN (Japan), FLNER (Russia), GANIL (France) and LBNL (USA). Using α-α correlation techniques the research group at GSI has identified various nuclei up to Z=112, whilst experiments at FLNER have produced the heaviest nuclei so far, element 118, using a hot fusion reaction [Og06]. The cross sections for these reactions are of the order of picobarns, which allows for the measurement of the α-decay chains from SHN. However, such experiments are time-consuming and the low cross sections mean that very few events are produced.

The interest in SHN is also due to their proximity to the next predicted shell closures for spherical nuclei, above N=82 and Z=50. The theoretical predictions for the next shell closures vary with the type of nuclear model used. Most models agree that the shell closure for neutrons is at N=184, however predictions for the protons range from Z=114 to 126, due to the differing treatment of the surface properties in the various models [Ćw96]. Generally, macroscopic-microscopic models predict a shell gap at Z=114 [Ni69, Ćw96], but self-consistent theories indicate that the proton surface thickness used in these models is too low. When larger values of the

proton diffuseness parameter are used in macroscopic-microscopic models the location of the shell gap increases to Z=120 or 126.

Self-consistent mean-field models have also been applied to SHN [Be01]. Figures 1.1 and 1.2 compare shell-correction energies predicted by non-relativistic and relativistic mean-field models, where the shell-correction energies indicate the location of the shell closures. Figure 1.1 shows the theoretical shell closures for the nuclei at N=82, Z=50, the same calculations but for SHN are plotted in Figure 1.2. The differences between the two figures are quite apparent. The six models consistently predict the same magic numbers for the nuclei around N=82, Z=50, whereas the magic numbers for SHN vary. The shell closures for lighter nuclei are well defined, but for SHN they induce a region of enhanced stability. Theoretical studies of SHN could be advanced greatly with more experimental information, especially about their excited structures. Unfortunately, the SHN that are accessible are neutron-rich and the reaction yields are too low for studying excited structures.

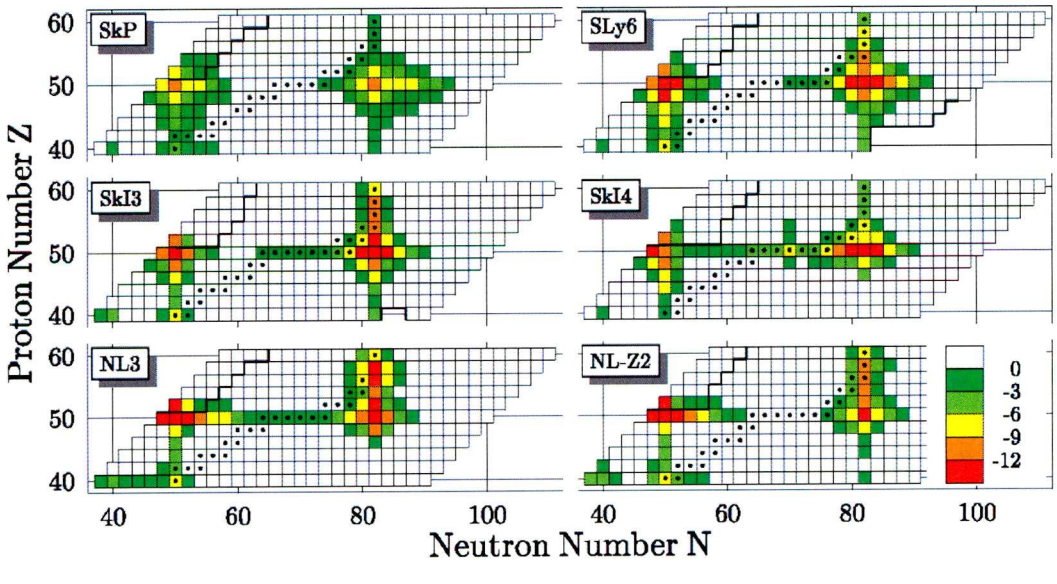

Figure 1.1: Self-consistent mean-field calculations of shell-correction energies, in MeV, for nuclei around N=82, Z=50 [Be01].

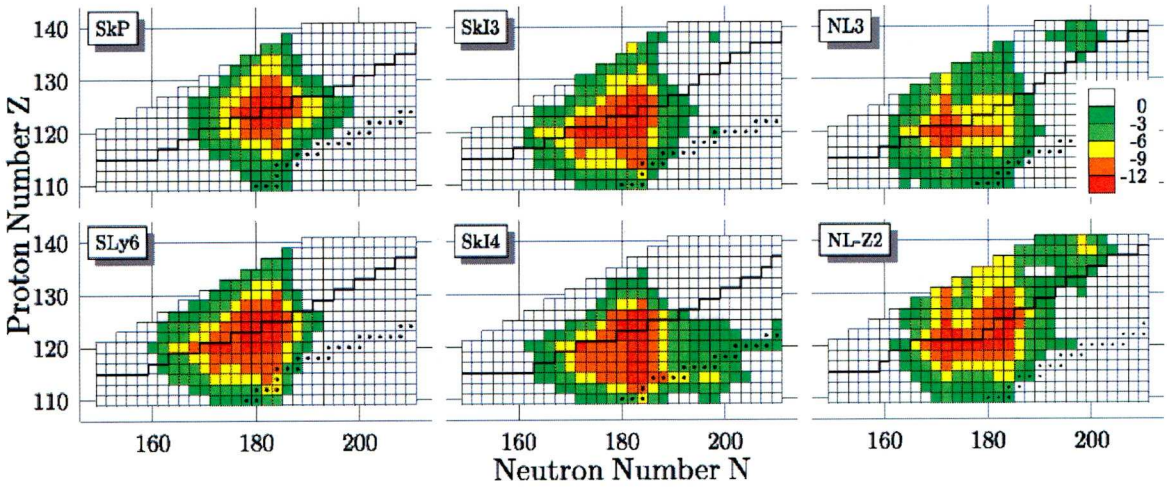

Figure 1.2: Self-consistent mean-field calculations of shell-correction energies in MeV, for SHN [Be01].

The low-Ω orbitals that originate from the subshells for spherical nuclei are shifted to lower energies for prolate deformed nuclei, due to a large overlap of wavefunctions of the single-particle orbitals and the nuclear core. The orbitals involved in the formation of the shell closures for spherical nuclei are responsible for single-particle excitations in nuclei around ^{250}Fm. Therefore, single-particle information that is gained from studying the excited states of nuclei around Z=100 and N=150, informs the theories of the next spherical shell closures. The reactions are more favourable for these lighter nuclei, reaction cross-sections are in order of 100 nanobarns, which is sufficient to obtain nuclear structure information from studying the excited states. ^{250}Fm α-decays from its ground state, as do many of the nuclei in the region. The α-decay energy and half-life provide useful tools for identifying the decays from excited states. In previous studies of ^{250}Fm, recoil-α tagging has revealed the ground-state rotational band [Pr06, Ba06]. Less intense γ-ray transitions were also observed and these are thought to be related to the isomeric state of ^{250}Fm, identified in [Gh73]. A new technique is applied to the study of ^{250}Fm in this work. The internal conversion electrons emitted in the decay of the isomer are used to

perform recoil-isomer tagging, as suggested by Jones [Jo02]. It has been used with great success in the study of ^{254}No [He06, Ta06], where the study of single-particle excitations through recoil-isomer tagging indicate a deformed shell gap at Z=100.

Chapter 2

Nuclear Properties

The simplest description of the nucleus is the liquid drop model (LDM). Treating the nucleus as an incompressible, spherical liquid drop, it successfully predicts fusion, fission and α-decay processes. However, the LDM fails to explain the systematic deviations experimentally observed in nuclear binding energy, nucleon separation energies, nuclear charge radii and the first excited state of the nucleus. The systematic deviations occur at common proton and neutron numbers, or magic numbers 8, 20, 28, 50, 82 (and 126 for N only). These deficiencies in the LDM suggest that protons and neutrons move independently in a nuclear potential, similar to the atomic electrons.

In 1949 the shell model was proposed, to explain the systematic deviations at magic numbers [Ma49]. In the model, the single particles in the nucleus are moving in a spherically-symmetric Wood-Saxon potential, $V(r)$. The interaction between a nucleon's intrinsic spin, $\underline{s}$, and orbital momentum, $\underline{l}$, introduces a spin-orbit term, $V_{\underline{l}.\underline{s}}(r)$, to the potential,

$$V = V(r) + V_{\underline{l}.\underline{s}}(r). \tag{2.1}$$

Using this potential, the model successfully predicts the magic numbers which have been observed experimentally. It also succeeds in explaining the spins and magnetic moments of nuclei near magic numbers. However, large quadrupole moments led to the discovery of ground-state deformed nuclei [To49] which fail to be described by a

spherical potential. For deformed nuclei, the shell model is used with a non-spherical nuclear potential in the Nilsson model [Ni55], discussed in Section 2.1. In general, the shell model successfully explains many of the properties involving nucleons close to the Fermi surface, however it fails to describe the bulk properties. Neither the shell model or the LDM explains both bulk and single-particle properties of the nucleus. To take advantage of the effective features of the LDM and the shell model, Strutinsky [St68] introduced the shell correction procedure. The total binding energy, E_{tot}, is divided into two parts,

$$E_{tot} = E_{LDM} + E_{osc}, \tag{2.2}$$

where E_{LDM} is the binding energy calculated using the LDM, which smoothly varies with nucleon number, A. The oscillations in the binding energy, due to the shell effects, are described by E_{osc}, also referred to as the shell correction energy. This treatment of the nucleus is the basis of the macroscopic-microscopic approach often applied to SHN.

Aspects of nuclear theory that are relevant for the analysis of ^{250}Fm are discussed below. The excited states of ^{250}Fm are labelled using asymptotic quantum numbers defined in the Nilsson model, detailed in Section 2.1. Excited states of ^{250}Fm decay either via γ or internal conversion decays, discussed in Section 2.3 and Section 2.4 respectively. Intensity ratios of γ decays are related to the electromagnetic properties of the nucleus. Transition intensities obtained in the experiment are related to gyromagnetic ratios, g_K, according to the principles described in Section 2.5. Finally, Section 2.6 explains the origin and characteristics of K-isomers.

2.1 The Nilsson Model

The Nilsson model considers single-particle energy levels of all nucleons moving in an axially-deformed harmonic oscillator potential. Consider a prolate deformed nucleus with one single particle orbiting the core. The core possesses angular momentum, $\underline{R}$, and the single particle has angular momentum, $\underline{J}$. The total angular

momentum of the nucleus, $\underline{I}$, is equal to the sum of the two components,

$$\underline{I} = \underline{R} + \underline{J}. \tag{2.3}$$

The projection of $\underline{I}$ onto the symmetry axis (z) is equal to K, as shown in Figure 2.1a. When there are two single particles orbiting the core, $\underline{J}$ is the sum of the single-particle angular momenta $\underline{j}_1$ and $\underline{j}_2$,

$$\underline{J} = \underline{j}_1 + \underline{j}_2. \tag{2.4}$$

Figure 2.1b shows the case when there are two single particles orbiting a prolate nucleus. The projections of $\underline{j}_1$ and $\underline{j}_2$ onto the symmetry axis are equal to Ω_1 and Ω_2, respectively, which sum to K. More generally, for any number of single particles orbiting the core, K is the sum of their angular momentum projections onto z,

$$K = \sum_i \Omega_i. \tag{2.5}$$

A low value of Ω in prolate nuclei translates to a single-particle orbital which has a large overlap with the nuclear core. The opposite is true for high values of Ω, the single-particle orbitals do not overlap as much with the nuclear core.
A single-particle state orbiting the deformed nucleus is completely described by the Nilsson, or asymptotic, quantum numbers,

$$\Omega^{\pi}[Nn_z\Lambda]. \tag{2.6}$$

N is the number of oscillation quanta, n_z is the number of oscillation quanta in the z direction and the parity, π, is defined as $\pi = (-1)^N$. A single particle has both intrinsic spin, $\underline{s}$, and orbital angular momentum, $\underline{l}$, which contribute to its total angular momentum, $\underline{j} = \underline{l} + \underline{s}$. Λ is the projection of the orbital angular momentum along z and Σ is the projection of the intrinsic spin on z, hence

$$\Omega = \Lambda + \Sigma = \Lambda \pm 1/2. \tag{2.7}$$

These labels are used to identify the single-particle states in a Nilsson diagram of deformation plotted against single-particle energy. The Nilsson diagrams for protons ($Z \geq 82$) and neutrons ($N \geq 126$) are shown in Appendix A (Figures 1 and 2).

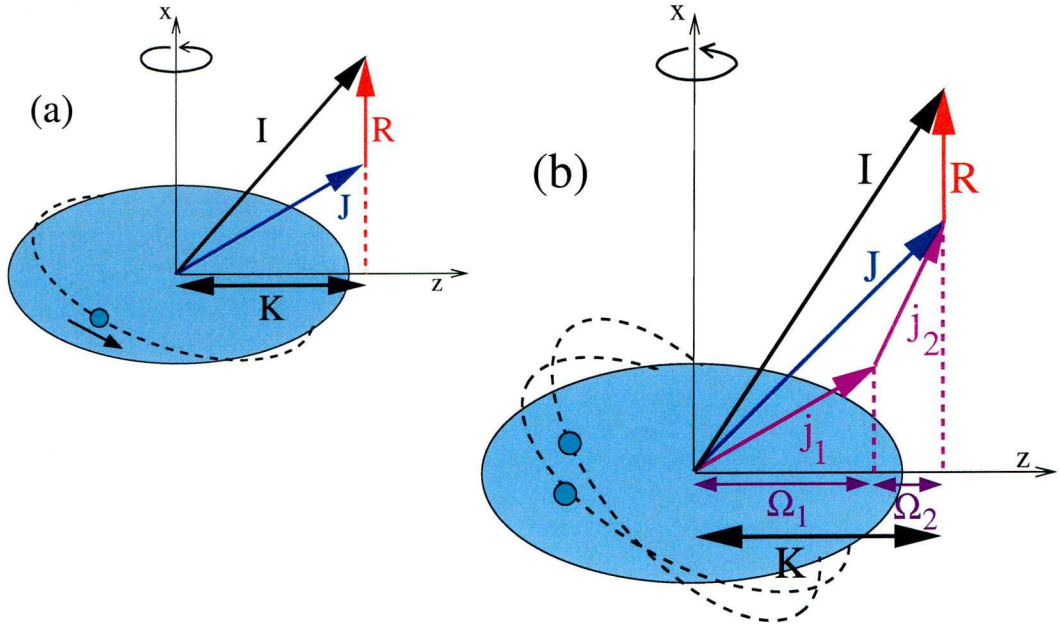

Figure 2.1: Angular momentum of a prolate nucleus with (a) one and (b) two single particles.

2.2 Nuclear Rotation

For a rotating nucleus, only parity and signature are good quantum numbers. The signature quantum number, r, relates to the reflection symmetry (the invariance of the system to rotation by 2π about an axis perpendicular to the symmetry axis). The allowed values of r are

$$r = (-1)^I \tag{2.8}$$

which leads to the selection rules

$$I = 0, 2, 4, \ldots \text{ for } K = 0 \text{ and } r = +1, \tag{2.9}$$

$$I = 1, 3, 5, \ldots \text{ for } K = 0 \text{ and } r = -1. \tag{2.10}$$

This produces two sequences of levels with opposite signature values, known as signature partners. When $K \neq 0$, a rotational band has two sequences with opposite signature and with angular momenta, $I = K, K+2, K+4, \ldots$ and

$I = K+1, K+3, K+5, \ldots$. For the ground state of an even-even nucleus with angular momentum I, the kinetic energy of the levels is given by,

$$E_{rot}^{K=0}(I) = \frac{\hbar^2}{2\Im^{(0)}} I(I+1) \tag{2.11}$$

where $\Im^{(0)}$ is the static moment of inertia, which assumes that the nucleus behaves as a rigid body. A rotational band is formed by a sequence of levels with increasing I and rotational energy E_{rot}. However, for nuclei with $K \neq 0$ particle-rotor coupling occurs which produces different types of rotational bands. In weakly-deformed nuclei or where the particle rotation is fast, there is a weak-coupling or Rotation Aligned (RAL) scheme and bands are determined by the odd particle with spin j, to give states with spins $I = j, j+2, j+4, ...$ and energies

$$E_{rot}^{RAL}(I) = \frac{\hbar^2}{2\Im^{(0)}} (I - j_x)(I - j_x + 1), \tag{2.12}$$

where j_x is the projection of angular momentum of the single particle(s) onto the rotational axis. For these conditions, two rotational sequences of states with different moments of inertia and signature are produced, leading to a large signature splitting. In the so-called Deformation Aligned (DAL) scheme where the nuclei are strongly deformed and where there is strong coupling, K becomes a good quantum number and there is little signature splitting. In this instance,

$$E_{rot}^{DAL} = \frac{\hbar^2}{2\Im^{(0)}} \left[I(I+1) - K^2 \right], \tag{2.13}$$

gives the energies of the rotational band with angular momenta
$I = K, K+1, K+2, ...$
The nucleus rotates with rotational frequency, ω, defined by

$$\hbar\omega = \frac{dE}{dI_x} \tag{2.14}$$

where I_x is the angular momentum projection onto the rotation axis, given by $I_x = \sqrt{I(I+1) - K^2}$. The variation of the moment of inertia with ω is described by the kinematic, $\Im^{(1)}$, and dynamic, $\Im^{(2)}$, moments of inertia, which are given by the

first and second order derivatives of Equation 2.11, respectively. When $I \approx I_x$, the kinematic and dynamic moments of inertia are defined by,

$$\Im^{(1)} = \left(\frac{2}{\hbar^2} \frac{dE(I)}{dI} \right)^{-1} = \hbar \frac{I}{\omega}, \tag{2.15}$$

$$\Im^{(2)} = \left(\frac{1}{\hbar^2} \frac{d^2E(I)}{dI^2} \right)^{-1} = \hbar \frac{dI}{d\omega}. \tag{2.16}$$

Experimentally it is useful to define $\Im^{(1)}$ and $\Im^{(2)}$ in terms of the energy of transition, E_γ, using

$$\Im^{(1)} = \frac{\hbar^2}{E_\gamma}(2I - 1), \tag{2.17}$$

$$\Im^{(2)} = \frac{4\hbar^2}{E_\gamma(I + 2 \rightarrow I) - E_\gamma(I \rightarrow I - 2)}. \tag{2.18}$$

2.3 γ decay

The observation of γ rays emitted from the nucleus uncovers excited states, offering information on the structure and behaviour of the nucleus. The properties of electromagnetic transitions are described in detail in [Ej89], here we discuss those properties relevant to the analysis.

Consider a γ decay from a state with angular momentum I_i to a state with I_f. The multipolarity of the γ transition, L, and parity change, $\Delta\pi$, are subject to the selection rules,

$$|I_i - I_f| \leq \quad L \quad \leq I_i + I_f, \tag{2.19}$$

$$\Delta\pi(EL) = (-1)^L \quad \text{and} \quad \Delta\pi(ML) = (-1)^{L+1}, \tag{2.20}$$

with the exception of monopole (L=0) transitions, which unable to go through γ decay instead decay via internal conversion. The E1, M2, E3 and M4 multipolarity transitions induce a change in parity but M1, E2, M3 and E4 transitions do not. If $L \geq 2$ then more than one multipolarity transition is possible. Stretched transitions induce the maximum change in angular momentum between the initial and final

states, whilst those transitions that change less than the maximum are folded transitions.

Experimentally, the multipole order can be deduced by measuring the angular distribution of the radiation whilst the polarisation of the radiation determines whether the transition is electric or magnetic. Although if statistics are low, neither measurement can be performed and one makes deductions using the transition probabilities and selection rules (Equation 2.20). Transition probabilities are calculated using

$$T_{fi}(\sigma L; I_i \rightarrow I_f) = \frac{8\pi(L+1)}{\hbar L((2L+1)!!)^2}\left(\frac{E_\gamma}{\hbar c}\right)^{2L+1} B(\sigma L; I_i \rightarrow I_f), \tag{2.21}$$

where $B(\sigma L)$ is the reduced transition probability of the decay

$$B(\sigma L; I_i \rightarrow I_f) = \frac{1}{2I_i+1}\left|\left\langle f||\widehat{T}_{\sigma L}||i\right\rangle\right|^2. \tag{2.22}$$

$\widehat{T}_{\sigma L}$ is the electric or magnetic multipole operator.

Transition probabilities are estimated by V. F. Weisskopf for single-particle transitions [We51]. These estimates are based on the shell-model treatment of the nucleus where a nucleon changing state causes the γ transition. Weisskopf single-particle estimates for transition probabilities, T^W, are shown in Table 2.1. Also shown are the Weisskopf units, B_{sp}, which are the reduced transition probabilities for single-particle transitions, estimated by Weisskopf. These values show that electric multipole transitions have higher transition rates than magnetic transitions of the same order, and that generally, lower order decays are more dominant. The estimates are often compared with experimental values, to calculate the hindrance of a transition. For instance, Weisskopf estimates for single-particle transitions are used to calculate the hindrance values of decays from isomeric states, see Equation 2.34.

A different approach is taken by Bohr and Mottelson [Bo99], using the geometric model to calculate the transition probabilities. This calculates the transition rates for collective excitations. The reduced transition probability for electric transitions

σL	T^W (s^{-1})	B_{sp}
E1	1.587×10^{15} E^3 B_{sp}(E1)	6.446×10^{-2} $A^{2/3}$
E2	1.223×10^{9} E^5 B_{sp}(E2)	5.940×10^{-2} $A^{4/3}$
E3	5.698×10^{2} E^7 B_{sp}(E3)	5.940×10^{-2} A^{2}
E4	1.694×10^{-4} E^9 B_{sp}(E4)	6.285×10^{-2} $A^{8/3}$
E1	3.451×10^{-11} E^{11} B_{sp}(E5)	6.928×10^{-2} $A^{10/3}$
M1	1.779×10^{13} E^3 B_{sp}(M1)	1.790
M2	1.371×10^{7} E^5 B_{sp}(M2)	1.650 $A^{2/3}$
M3	6.387×10^{0} E^7 B_{sp}(M3)	1.650 $A^{4/3}$
M4	1.899×10^{-6} E^9 B_{sp}(M4)	1.746 A^{2}
M5	3.868×10^{-13} E^{11} B_{sp}(M5)	1.924 $A^{8/3}$

Table 2.1: Single-particle estimates for transition probability, T^W, where transition energy, E, is in MeV and the Weisskopf units, B_{sp}(EL) and B_{sp}(ML), have units $e^2(fm)^{2I}$ and $\mu_N^2(fm)^{2I-2}$, respectively [Ri80].

are found to be related to the electric quadrupole moment, Q_0,

$$B(E2, I_i \rightarrow I_f) = \frac{5}{16\pi} e^2 Q_0^2 \langle I_i K 20 | I_f K \rangle^2 . \tag{2.23}$$

Whilst magnetic transition rates are dependent on the g factors of the nucleus, g_R, and single particle, g_K,

$$B(M1, I_i \rightarrow I_f) = \frac{3}{4\pi} \left(\frac{e\hbar}{2Mc} \right)^2 (g_K - g_R)^2 K^2 \langle I_i K 10 | I_f K \rangle^2 . \tag{2.24}$$

The g_R and g_K are the gyromagnetic ratios related to the nuclear core and single particle respectively, discussed in Section 2.5. These values are used instead of the single-particle values, B_{sp}, to calculate the transition rates of collective transitions within a band. The B_{sp} value in Table 6.1 is substituted for the B(E2) or B(M1) values calculated by Bohr and Mottelson, to give the collective transition rates, T^{col}.

2.4 Internal conversion decay

Internal conversion (IC) competes with the gamma decay process to a high extent in the isomeric decay of ^{250}Fm. Instead of producing a photon, the electromagnetic multipole field of the nucleus interacts with the atomic electrons. An IC electron is emitted from an atomic orbital, with kinetic energy, T_e,

$$T_e = (E_i - E_f) - B_e \tag{2.25}$$

where B_e is the binding energy of the electron and the energy of the nucleus before and after internal conversion is represented by E_i and E_f, respectively. Note that the binding energy B_e varies with atomic orbital, which means that for one transition the kinetic energy T_e varies. After the electron is emitted, the remaining atomic electrons rearrange to fill the vacancy created in the IC process, yielding X-rays in coincidence with the IC electrons.

The extent to which IC occurs in relation to the gamma decay process is defined by the IC coefficient α,

$$\alpha = \frac{\lambda_e}{\lambda_\gamma} \tag{2.26}$$

where the quantities λ_e and λ_γ are the decay probabilities of internal conversion and gamma decay, respectively. The coefficient is particularly important in this study for the following reasons:

- IC is more prevalent in heavier nuclei ($\alpha \propto Z^3$)
- Low-energy transitions have a higher probability of undergoing internal conversion ($\alpha \propto 1/E$)
- The probability for IC increases for high-L transitions ($\alpha \propto \sigma$L)
- K-shell transitions are the most likely ($\alpha \propto 1/n^3$, where n is the atomic shell number)

For high-multipole, low-energy transitions in heavy nuclei, like ^{250}Fm, the internal conversion rate from the K shell is high. For instance, for the $2^+ \rightarrow 0^+$ ground state band transition of ^{250}Fm $\alpha = 1305$ and as a result the gamma decay is not observed. When a gamma ray transition is detected the total transition intensity λ_{tot}, which includes the conversion process, is calculated using the conversion coefficient

$$\lambda_{tot} = \lambda_\gamma(1 + \alpha). \tag{2.27}$$

This allows the total branching ratio of a decay to be obtained from just the efficiency corrected γ-ray intensity and the internal conversion coefficient.

2.5 Gyromagnetic ratios

The magnetic dipole moment is a measure of the current distribution in the nucleus, which is generated by the intrinsic spin and orbital motion of the nucleons. The magnetic moment induced by orbital motion of a nucleon with angular momentum l is

$$\mu_l = \mu_N g_l l \tag{2.28}$$

in units eV/T. g_l is the gyromagnetic ratio, or g-factor, and μ_N is the magnetic moment produced by the orbital motion of a proton ($\mu_N = \frac{e\hbar}{2m_p}$). Therefore g_l=1 for

protons and, as neutrons have no charge, g_l=0 for neutrons. Similarly, the magnetic moment produced by the intrinsic spin, s, of the nucleons is

$$\mu_s = \mu_N g_s s \tag{2.29}$$

where s=1/2 for fermions. The magnetic moment of a nucleus can be calculated by summing the contributions from the spin and orbital motion of all nucleons

$$\mu = \mu_N \sum_{i=1}^{A} [g_{l,i} l_i + g_{s,i} s_i] \tag{2.30}$$

where A is the number of nucleons. For an even-even nucleus with no intrinsic excitation (K=0) and an angular momentum R, the magnetic moment is generated by the collective motion of the protons in the nucleus

$$\mu = g_R R \mu_N, \tag{2.31}$$

where g_R is the g-factor describing the rotational motion of the core, and is approximately $g_R \sim Z/A$. For excitations in even-even nuclei, or odd nuclei in general, the single-particle and core contributions are taken into account when calculating the magnetic moment,

$$\mu = \left(g_R I + (g_K - g_R) \frac{K^2}{I+1} \right) \mu_N \tag{2.32}$$

where the g-factor, g_K, is the single-particle contribution and I is the total angular momentum of the core and single particle. The g-factor g_K describes the single-particle contribution to the magnetic dipole moment and strongly depends on the single-particle state. The magnetic transition probability of a γ decay is determined by the value of g_K (Section 2.3). Therefore, measuring the probability of magnetic transitions provides information about single-particle states.

2.6 K-Isomerism

Isomeric states in the fermium region are caused by spin traps in which a large change in spin is needed for the isomer to decay; these are commonly observed in

prolate nuclei away from closed shells [Wa99]. When the change in K, $\triangle K$, for a transition is larger than the multipole order λ the transition is K-forbidden. The factor ν defines the degree that a transition is forbidden

$$\nu = \triangle K - \lambda. \tag{2.33}$$

The reduced hindrance value, f_ν, is related to the Weisskopf hindrance value, F_W, by a factor of $\frac{1}{\nu}$ and is a measure of the hindrance per unit of forbiddenness. It is calculated using

$$f_\nu = \left[\frac{t^\gamma_{1/2}}{t^W_{1/2}}\right]^{\frac{1}{\nu}} = [F_W]^{\frac{1}{\nu}}, \tag{2.34}$$

where $t^W_{1/2}$ is the Weisskopf single-particle estimate for the half-life of a decay and $t^\gamma_{1/2}$ is the partial half-life of the γ decay, deduced from experimental data. $t^W_{1/2}$ is calculated using the single-particle transition estimates, see Section 2.3. The value of f_ν is approximately equal to 100, which means that if ν increases by one then the γ-ray transition rate decreases by a factor of two [Wa05].

Chapter 3

Review of Experimental Studies

Many of the studies performed in recent years have shed light on the systematics of the deformed nuclei around Z=100, N=150. Bands with $K^{\pi}=2^{-}$ and 8^{-} have been observed in the N=150 isotones at similar energies, and there are similar results for N=152 isotones. High-K isomers have been observed in the isotones and other nuclei in the region. The properties of the isomers and the excited bands imply that shell gaps exist for deformed nuclei at Z=102 and N=152. Experimental results in the deformed region not only constrain theoretical descriptions of these nuclei, they also have implications for the heavier spherical nuclei close to the next shell gaps. To obtain a more balanced perspective on the regional systematics, it is appropriate to review the experimental data relevant to the study of ^{250}Fm. Therefore, experimental data on N=150 isotones and high-K isomers are discussed in Sections 3.2 and 3.3. The previous studies of ^{250}Fm are discussed in Section 3.1. In Chapter 7, the results of this study are compared to the data discussed here.

3.1 Previous studies of ^{250}Fm

A ^{250}Fm isomeric state was first identified in the 1970s by Ghiorso et al. [Gh73], at the Lawrence Berkeley Laboratory. ^{250}Fm nuclei were produced by a fusion evaporation reaction, in which a ^{12}C beam bombarded a ^{249}Cf target. The ^{250}Fm

nuclei recoiled into a chamber where a helium-gas stream implanted them onto a rotating wheel. Energy and timing measurements were taken using Si(Au) detector stations placed around the wheel (see Figure 3.1). As well as observing the α-decay half-life, a half-life of 1.8(1) s seconds was observed as originating from ^{250}Fm and was attributed to the decay of an isomeric state in ^{250}Fm. In the same study, a ^{254}No isomeric decay with a half-life of 0.28(4) s was observed. It suggests that the isomers are formed by high-spin two-quasiparticle states, which are expected to exist near N=150 and Z=100. Table 3.1 shows the two-neutron and two-proton configurations predicted using the Nilsson model [Ni69]. For the ^{250}Fm isomer, there are two suggestions: a two-neutron quasiparticle state with $I^{\pi}=8^{-}$ or a two-proton quasiparticle state with $I^{\pi}=7^{-}$.

Nucleus	Neutron configuration	Proton configuration
^{250}Fm	$\{\frac{7}{2}^{+}[624]_{\nu} \otimes \frac{9}{2}^{-}[734]_{\nu}\}^{8-}$	$\{\frac{7}{2}^{+}[633]_{\pi} \otimes \frac{7}{2}^{-}[514]_{\pi}\}^{7-}$
^{254}No	$\{\frac{9}{2}^{-}[734]_{\nu} \otimes \frac{7}{2}^{+}[613]_{\nu}\}^{8-}$	$\{\frac{7}{2}^{-}[514]_{\pi} \otimes \frac{9}{2}^{+}[624]_{\pi}\}^{8-}$

Table 3.1: Two quasiparticle states, with K values, predicted using the Nilsson model [Ni69] in [Gh73].

The most recent study of ^{250}Fm [Pr06] observed the ground-state band utilising the JUROGAM+RITU+GREAT set up in Jyväskylä (see Chapter 4). There were also numerous low-energy γ rays that could not be placed in the level scheme. However, a γ-ray transition observed at 835 keV was placed between a 2^{-} state and the 2^{+} ground-state level using Alaga rules, Weisskopf estimates and theoretical calculations, see Section 6.2.1 for more details. An earlier experiment performed by Bastin et al. [Ba06] also observed the ground state band of ^{250}Fm using a similar set up at Jyväskylä. The JUROSPHERE IV array [Gr04] was situated at the target position to measure prompt γ rays. In addition, conversion-electron spectroscopy was performed using the SACRED spectrometer [Bu96] at the target position, thereby confirming the E2 nature of the ground-state decays.

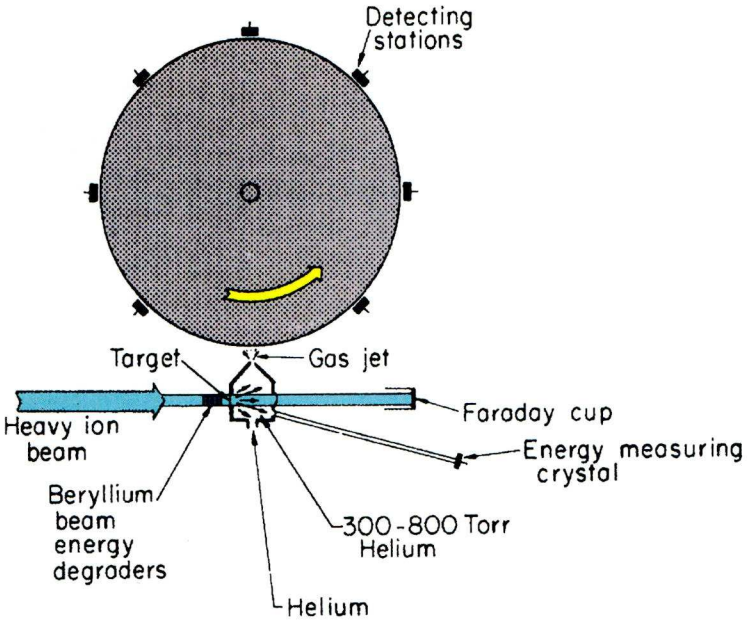

Figure 3.1: The setup of the experiment which first observed the isomeric state of ^{250}Fm [Gh73]. The heavy-ion ^{12}C beam bombarded a ^{249}Cf target to produce ^{250}Fm recoil nuclei. The helium gas jet transferred the recoils onto a rotating wheel which is surrounded by 7 Si(Au) detectors for α-particle measurements.

In these previous studies, recoil events and the subsequent α decays were used to identify γ decays relating to ^{250}Fm. The ^{250}Fm ground-state band is strongly populated in the reaction, making it difficult to observe other structure which relates to the ^{250}Fm isomer. Recently, a novel technique has been suggested by Jones [Jo02], which uses delayed conversion electrons to observe the transitions associated with the isomer only. The method removes the intense ground-state transitions using tagging techniques, discussed in Section 4.3. It has been used to great effect in the study of an isomeric state in ^{254}No [He06, Gr08], and has opened up a new method of analysis for the isomers in the region.

3.2 N=150 isotones

There are four other nuclei with N=150 which have been studied over the range Z=94–102: ^{252}No, ^{248}Cf, ^{246}Cm and ^{244}Pu. Excited bands with $K^{\pi}=2^{-},8^{-}$ have been observed in these N=150 nuclei, and the band heads of the $K^{\pi}=8^{-}$ bands of ^{252}No and ^{246}Cm have been found to be isomeric. Similar high-K isomers could also exist in ^{248}Cf and ^{244}Pu but experiments so far have not been sensitive to isomeric states. The 8^{-} bands are formed by two-neutron quasiparticle excitations whilst the 2^{-} bands are expected to be mixed. Experimental studies indicate that the 2^{-} bands are dominated by single-particle excitations. However, the energies of the 2^{-} bands are lower than expected for a pure single-particle excitation. The low energies can be explained by the mixing of single-particle excitations with K=2 octupole excitations, which are predicted at low energies in these nuclei [Ne70, Su08]. The experimental results and band assignments are now discussed for each N=150 isotone.

The study of ^{252}No by Sulignano et al. identified excited bands, including an isomeric state [Su07]. A ^{206}Pb(^{48}Ca, 2n)^{252}No fusion-evaporation reaction was performed using the SHIP velocity filter at GSI Darmstadt. An isomer was observed with a half life of 110(10) ms at an energy of 1.254 MeV with respect to the ground

state, its decay path is shown in Figure 3.2a. The level scheme was built using γ-γ and electron-γ coincidences, whilst the spin-parity assignments were deduced from the K X-ray intensities. This leads to the configuration assignments of $\{\frac{9}{2}^-[734]_\nu \otimes \frac{7}{2}^+[624]_\nu\}^{8-}$ for the K^π=8^- band, based on constrained Hartree-Fock-Bogolyubov (HFB) mean-field calculations performed by Delaroche et al. using the Gogny D1S force [De06]. In the ^{252}No study, the K^π=2^- side band was assigned as a K=2 octupole vibration, after comparison of the level scheme with other N=150 isotones. However, a recent study by Robinson et al. found that the 2^- octupole states observed in N=150 isotones have major contributions from the $\{\frac{9}{2}^-[734]_\nu \otimes \frac{5}{2}^+[622]_\nu\}^{2-}$ configuration found at low energy [Ro08].

Similar excited structure has also been discovered in ^{246}Cm [Ro08]. A ^{244}Pu(α,pn) reaction was performed at the Argonne National Laboratory, where the excited structure of ^{246}Cm was investigated following the β^- decay of ^{246}Am. The measurement of γ ray and conversion electron coincidences led to the level scheme of ^{246}Cm, shown in Figure 3.2b. A 2^- band was observed at 842 keV and assigned as an octupole vibration but with a major $\{\frac{9}{2}^-[734]_\nu \otimes \frac{5}{2}^+[622]_\nu\}^{2-}$ component. The observed 8^- band at 1180 keV was attributed to the $\{\frac{9}{2}^-[734]_\nu \otimes \frac{7}{2}^+[624]_\nu\}^{8-}$ configuration, as in ^{252}No. The 8^- level was recently found to be isomeric, with a half-life of 1.12(24) s [Ta09].

Less is known about the excited structures of the N=150 isotones ^{248}Cf and ^{244}Pu, however transfer reactions have identified some levels in their excited bands. A ^{249}Cf(d,t) transfer reaction performed in the 1970s found three bands in ^{248}Cf, including a K^π=2^- state at 593 keV [Ya75] which was assigned as the $\{\frac{9}{2}^-[734]_\nu \otimes \frac{5}{2}^+[622]_\nu\}^{2-}$ configuration from single-particle spectra and cross-section calculations. Recently the experimental data has been re-analysed to find two levels at 1261 and 1351 keV, which have been assigned as 8^- and 9^- levels of the $\{\frac{9}{2}^-[734]_\nu \otimes \frac{7}{2}^+[624]_\nu\}^{8-}$ band [Ka08].

Excited levels of ^{244}Pu have also been studied, using a ^{244}Pu(d,d')^{244}Pu reaction [Th75]. The 3^- level of a K^π=2^- band was identified at 957 keV.

Nucleus	$E_x^{2^-}$ [keV]	$E_x^{8^-}$ [keV]	$t_{1/2}$
^{244}Pu	(923)	(1216)	-
^{246}Cm	842	1180	1.12(24) s
^{248}Cf	593	(1261)	-
^{252}No	929	1254	110(10) ms

Table 3.2: The energies of the $K^\pi=2^-$, 8^- band heads in the N=150 nuclei, together with the half-life of the 8^- state where available.

Calculations by Robinson et al. [Ro08] suggest the 2^- level of the band is at 923 keV, which is useful for comparing with the other N=150 isotones. Excited states of ^{244}Pu were also populated in the β^- decay of ^{244}Np [Mo87]. These studies allowed the tentative assignment of a level at 1216 keV with spin 7^+ or 8^+, due to its decay to the 8^+ ground-state level. However with new information about the nuclei in this region, it is more likely that the state at 1216 keV has a spin 8^-, as discussed in [Ro08].
The properties of the excited bands observed in N=150 nuclei are summarised in Table 3.2. Bands with the same spin and parity have been observed experimentally at similar energies in these nuclei. The implications of the excited structures of N=150 nuclei are discussed in Chapter 7, when they are compared to the ^{250}Fm results found in this study.

3.3 Regional systematics

Since the first observation of the ^{250}Fm and ^{254}No isomers [Gh73], other isomeric states have been identified in even-even nuclei in the region. The isomeric states of N=150 nuclei ^{252}No and ^{246}Cm have already been discussed in Section 3.2. Isomers have also been identified in ^{250}No [Pe06], ^{244}Cm [Ho84, Ha63], ^{248}Fm [?], ^{256}Fm [Ha89], ^{248}Cm [Ta09] and ^{270}Ds [Ho01]. The high-K isomers offer information about single-particle energies in the deformed region close to predicted shell gaps.

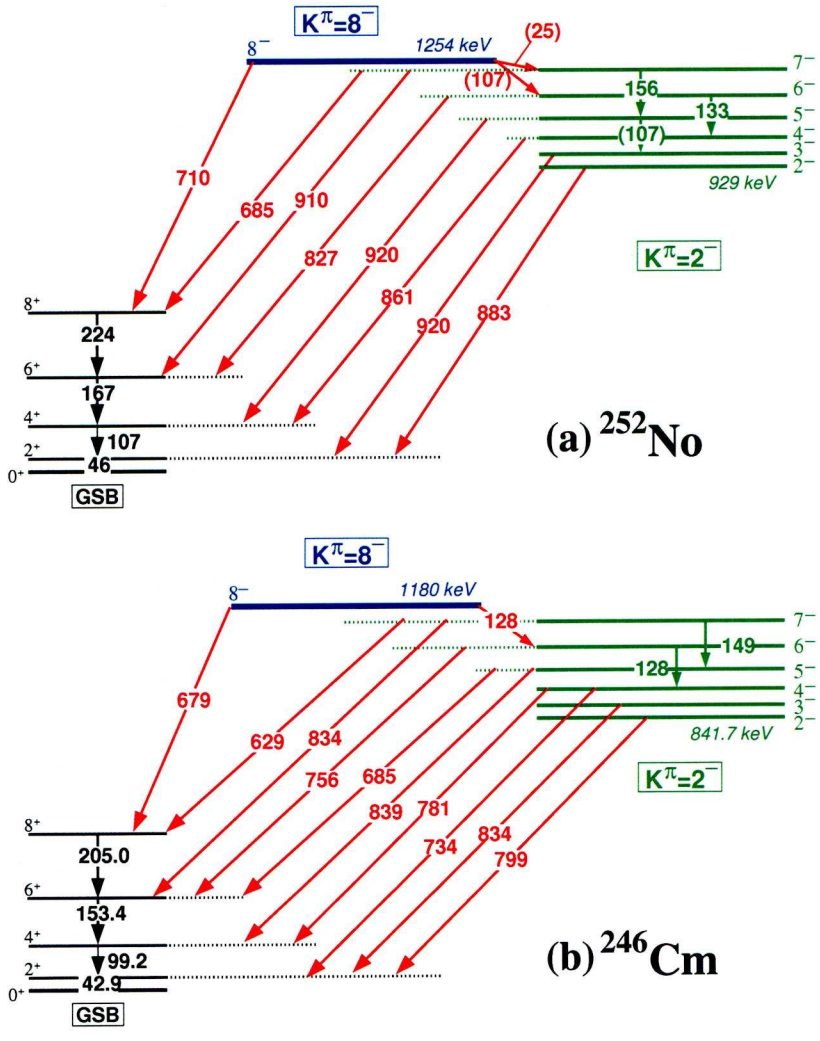

Figure 3.2: The level schemes of (a)^{252}No and (b) ^{246}Cm from [Su07] and [Ro08], respectively. Only the ground-state levels fed by the non-yrast decays are shown (black). The K^{π}=2^{-} side band (green) and the 8^{-} isomeric level of the K^{π}=8^{-} band (blue) have been identified, using interband transitions (red).

The experimental data of the isomers is summarised in Table 3.3, in order of neutron number. Information about ^{250}Fm is taken from the first observation of the isomer [Gh73], the new data found in this study is considered in Chapter 7. The isotones of ^{250}Fm, ^{246}Cm and ^{252}No, have been assigned as $\{\frac{7}{2}^+[624]_\nu \otimes \frac{9}{2}^-[734]_\nu\}_{8^-}$ bands. As a result, the ^{250}Fm isomer is expected to be an 8^- state with the same configuration. However, the configuration assignments of ^{246}Cm and ^{252}No are based on theoretical predictions and systematics. A goal of these studies is to use recoil-isomer tagging techniques to obtain γ-ray intensity ratios and thereby determining the single-particle configuration unambiguously. This has already been performed for ^{254}No to give an unambiguous assignment of the 8^- isomer [Gr08]. So far, ^{270}Ds is the heaviest nucleus in which a high-K isomer has been found. It α decays with half-life $t_{1/2}$=$6.0^{+8.2}_{-2.2}$ ms, which is longer than the ground-state α decay ($t_{1/2}$=100^{+140}_{-40} μs). Xu et al. performed potential-energy surface calculations of multi-quasiparticle configurations to investigate the inversion of stability observed in ^{270}Ds. The study found that long lifetimes of the high-spin isomers are caused by an increase in the height of the fission barrier along with a reduction in α decay probability.

Figure 3.3, taken from [De06], shows the experimental excitation energies for heavy nuclei with long-lived isomers, compared with two-quasiparticle excitation energies calculated using a constrained HFB mean-field method with a Gogny force. The energy of the 8^- band of ^{250}Fm is predicted to be between 1 and 1.5 MeV. A two-neutron quasiparticle excitation with K^π=8^- is predicted for ^{250}Fm, at >200 keV lower than the average value of 1.25 MeV indicated by experiment. For ^{256}Fm, a two-neutron quasiparticle excitation with K^π=7^- is predicted at >200keV above the experimental energy. There are no two-quasiparticle excitations predicted with K^π=8^- for ^{254}No, although a two-proton quasiparticle excitation is predicted at >300 keV above the 3^+ band observed in experiments. However, the predictions of the single-particle excitation energies for the lighter nuclei are in good agreement with the experimental values. The single-particle states that form the excited bands

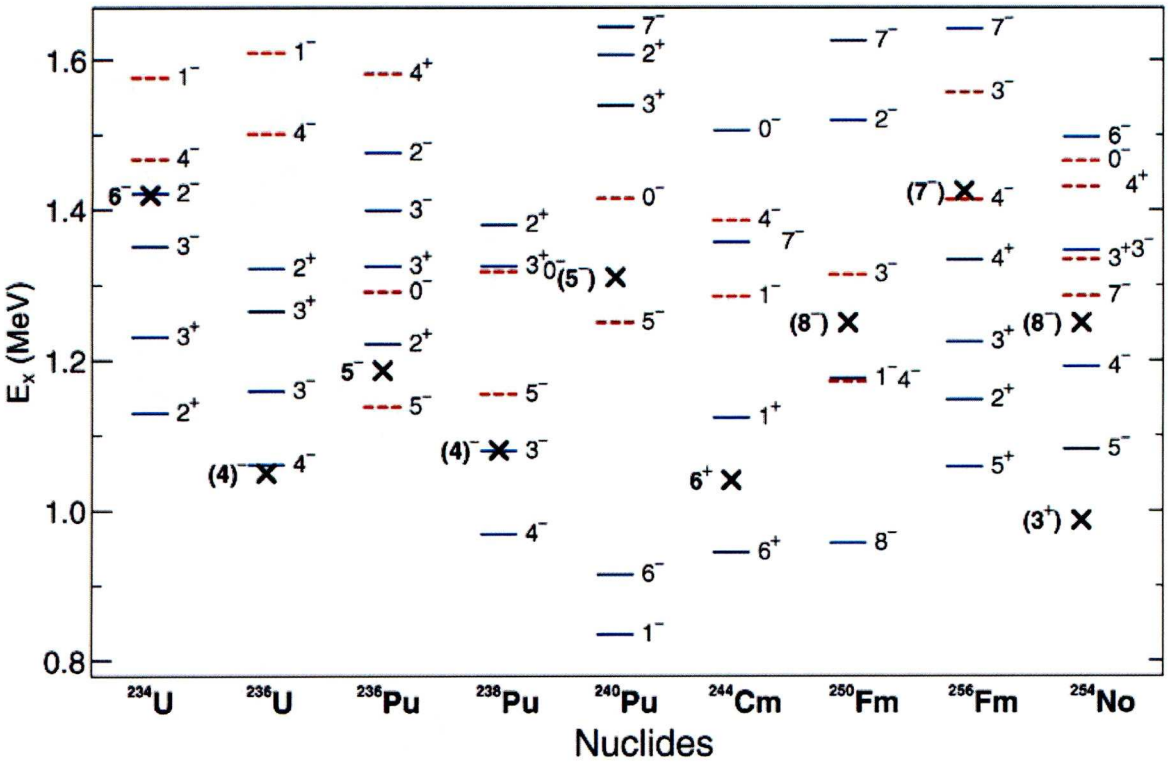

Figure 3.3: Experimental excitation energies (crosses) compared with the energies of two-quasiparticle excitations calculated for proton (dashed lines) and neutrons (solid lines), taken from [De06].

in the lighter nuclei originate from low-j orbitals. When states from high-j orbitals are involved, for ^{250}Fm, ^{256}Fm and ^{254}No 8^- bands, the theoretical predictions can not reproduce experimental data. Experimental data obtained on the high-K isomers in the region informs the theoretical calculations of isomers and provides essential tests for the theories.

Isotone	Nucleus	K^π	E_x	Half-life	Configuration	Ref.
148	^{244}Cm	6^+	1040 keV	34 ms	$\frac{5}{2}^+[622]_\nu \otimes \frac{7}{2}^+[624]_\nu$	[Ho84, Ha63]
	^{248}Fm	-	-	~8 ms	-	[?]
	^{250}No	(6^+)	-	42 µs	$(\frac{5}{2}^+[622]_\nu \otimes \frac{7}{2}^+[624]_\nu)$	[Pe06]
150	^{246}Cm	8^-	1180 keV	1.1 s	$\frac{7}{2}^+[624]_\nu \otimes \frac{9}{2}^-[734]_\nu$	[Ro08, Ta09]
	^{250}Fm	7 or 8^-	-	1.8 s	$\frac{7}{2}^+[633]_\pi \otimes \frac{7}{2}^-[514]_\pi$ or $\frac{7}{2}^+[624]_\nu \otimes \frac{9}{2}^-[734]_\nu$	[Gh73]
	^{252}No	8^-	1254 keV	110 ms	$\frac{7}{2}^+[624]_\nu \otimes \frac{9}{2}^-[734]_\nu$	[Su07, Ro08]
152	^{248}Cm	8^-	1459 keV	146 µs		[Ta09]
	^{254}No	8^-	1296 keV	266 ms	$\frac{7}{2}^-[514]_\pi \otimes \frac{9}{2}^+[624]_\pi$	[He06, Gr08]
		-	~2.5 MeV	184 µs		
156	^{256}Fm	7^-	1425 keV	70 ns	$\frac{7}{2}^+[633]_\pi \otimes \frac{7}{2}^-[514]_\pi$	[Ha89]
160	^{270}Ds	9 or 10^-	~1.13 MeV	6 ms	$\frac{11}{2}^-[725]_\nu \otimes \frac{7}{2}^+[613]_\nu$ or $\frac{11}{2}^-[725]_\nu \otimes \frac{9}{2}^+[615]_\nu$	[Ho01]

Table 3.3: Properties of the isomers in nuclei above Z=98, N=148.

Chapter 4

Experimental Details

Information about the reaction, apparatus and techniques used in this experiment are presented here. The experimental techniques first used in the study of the K-isomer of ^{254}No [He06, Ta06] are now employed in the study of ^{250}Fm. The observation of the K-isomers is facilitated by the unique setup of the implantation detector, detailed in Section 4.2, and the recoil-isomer tagging technique (see Section 4.3). A brief description of the reaction and apparatus are discussed in Section 4.1, although they are very similar to those used in previous studies of ^{250}Fm [Pr06, Ba06].

4.1 An overview of the experiment and apparatus

The ^{204}Hg(^{48}Ca, 2n)^{250}Fm* fusion-evaporation reaction was performed at the Accelerator Laboratory at the University of Jyväskylä (JYFL). A $^{48}Ca^{10+}$ ion beam produced by the 14.5 GHz Electron Cyclotron Resonance Ion Source (ECRIS) was incident on a 500 μg/cm^2-thick mercury sulphide (HgS) target, which was coated on both sides with a 30 μg/cm^2 layer of carbon. The target was isotopically enriched and contains 90.5 % ^{204}Hg and 9.5 % ^{202}Hg. The relationship between the beam energy and the cross section of the ^{204}Hg(^{48}Ca, xn) reaction was studied in a previous experiment by Bastin et al. [Ba06]. The results of the study are shown in

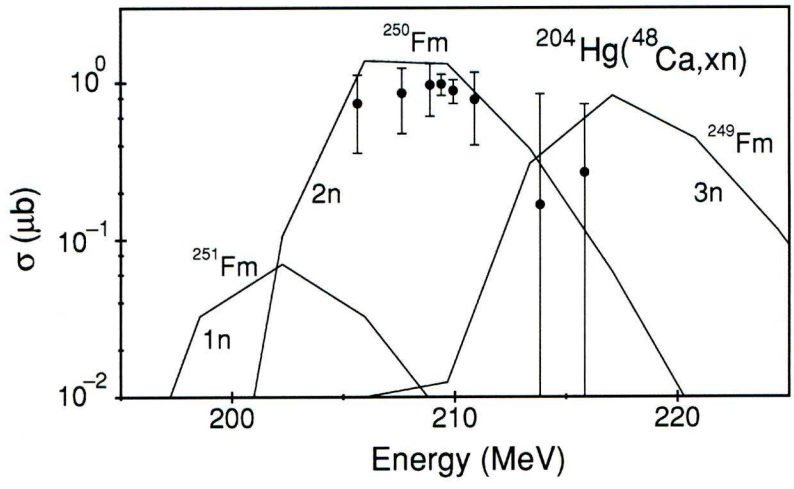

Figure 4.1: The cross section of the ^{204}Hg(^{48}Ca,xn) reaction as measured in a previous experiment (circles) and calculated using the HIVAP code (lines), taken from [Ba06].

Figure 4.1. A beam energy of 211 MeV was used and after roughly 160 hours of irradiation ~13,000 ^{250}Fm 7.43 MeV α particles were detected. A beam current above 15 pnA caused the target to sublimate, therefore the average beam current used was 9 pnA.

For this experiment, the JUROGAM+RITU+GREAT setup is used, see Figure 4.2. The JUROGAM array of 43 compton-suppressed, high-purity germanium detectors surround the target position in order to detect gamma radiation emitted promptly after the reaction. The array is made up of Eurogam Phase I and GASP-type detectors which are coaxial n-type crystals, 70 mm in diameter and 75 mm long with a tapered front end to achieve closer packing in the array [No94]. The detectors are placed in rings around the target chamber, using a supporting frame, at angles 72.1°, 85.8°, 94.2°, 107.9°, 133.6° and 157.6° with respect to the beam direction. The absolute efficiency of the JUROGAM array was measured at the start of the experiment to be 3.6% at 1.3 MeV, see Section 5.2.

The ^{250}Fm recoil ions are separated from the scattered beam using the Recoil Ion Transport Unit, RITU [Le95, Le97]. It consists of three quadrupole magnets and one dipole magnet, and is filled with low-pressure, helium gas. The RITU dipole magnet

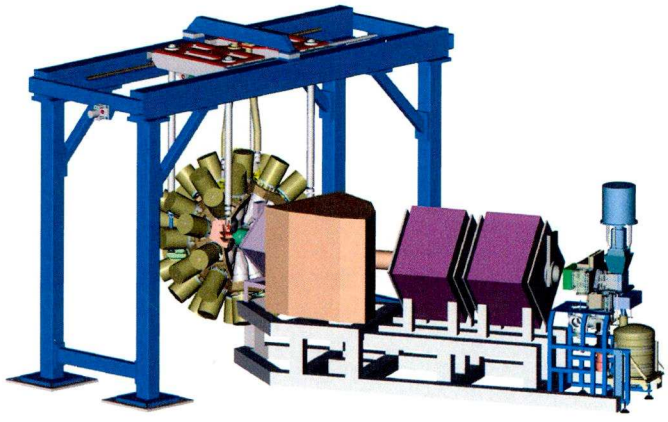

Figure 4.2: The experimental setup at the University of Jyväskylä, where the beam line enters from the left. It includes tha germanium array, JUROGAM (left), the recoil separator, RITU (centre) and a cluster of focal-plane detectors collectively named the GREAT spectrometer (right). Note that the two additional VEGA detectors are not shown in this figure [Se05].

uses magnetic rigidity to separate the fusion evaporation residues from the primary beam, whilst the two remaining quadrupole magnets focus the recoiling ion beam horizontally and vertically. A quadrupole magnet placed between the target and dipole magnet focusses the beam, matching it to the angular acceptance of the dipole magnet. This increases the transmission efficiency of RITU and makes it an ideal separator for heavy element experiments. Evaporation residues are transported through the separator with a flight time $t{\sim}1$ µs, and implanted into the focal-plane detectors. Whilst travelling through RITU, evaporation residues collide with the charged gas particles producing a beam with an average charge, which leads to more recoil ions being transmitted compared with vacuum separators. Generally, gas-filled separators have high transmission efficiencies but low mass resolving power. This does not pose a problem for heavy element studies, as there are few reaction channels open and recoil identification can be achieved using characteristic recoil and decay properties.

There are 5 detectors positioned at the focal plane of RITU, collectively known as the GREAT spectrometer [Pa03, An04]. The important components are described below:

- The multi-wire proportional counter (MWPC) identifies evaporation residues using energy loss, position and time measurements. It is positioned after RITU and is used in the distinction between recoil and decay events in GREAT.

- The ions implant into the double-sided silicon strip detectors (DSSD) which detect recoil implantations and subsequent α particles and internal conversion (IC) electron decays. The setup of the DSSD detectors is discussed in more detail later (see Section 4.2) as it differs from the conventional setup and is the key to the detection of the isomer. There are two DSSD detectors side-by-side, each has 60 vertical and 40 horizontal 1 mm-wide strips, providing 4800 position and time-sensitive pixels overall, useful for recoil-decay tagging (see Section 4.3). All the signals produced in the DSSDs are referred to as 'events' and are stored in order to perform spatial and temporal correlations.

- A planar germanium detector is located down the beam-line from the DSSD. It detects X-rays and low-energy γ rays, and has a high efficiency at low energies ($<$ 300 keV), see Section 5.2.

- The GREAT clover germanium detector is situated above the DSSD and planar detectors. In addition, two VEGA detectors, on loan from GSI, are placed on either side of GREAT to improve focal-plane statistics of high-energy γ rays. Both clover and VEGA germanium detectors are coaxial, n-type detectors which have a higher efficiency at high energy than the planar germanium detector.

- In addition, there are PIN diode detectors surrounding the DSSD which conventionally detect high-energy IC electrons. Low-energy conversion electrons released in the decay of heavy nuclei, see Section 2.4, are more likely to be absorbed in the DSSD rather than the PINs. Furthermore, using the DSSD

to detect the conversion electrons enables the recoil-isomer tagging method described in Section 4.3.

All the events that occur in the detectors are time-stamped and recorded using the Total Data Readout method, summarised in Figure 4.3 and discussed in more detail in [La01]. The signals from the detectors are manipulated by linear amplifiers and constant-fraction discriminators (CFD) before being converted to digital signals in the Analogue-to-Digital Converters (ADCs). For low channel numbers (<1000), the relationship between the analogue signal and digital output is non-linear. This discrepancy is dealt with in the post-experimental analysis by applying a correction to the energy calibration, as described in Section 5.1. Signals are time-stamped in 10 ns bins and sent to a buffer. The events are put back in time order in the event builder and then stored ready for analysis.

4.2 Detection of internal conversion electrons

IC electrons are used to observe isomeric decays of nuclei in the ^{250}Fm mass region because, as outlined in Section 2.4, internal conversion is more prevalent in heavy nuclei for low-energy transitions. If a ^{250}Fm isomer is populated, IC electrons are detected at the focal plane subsequent to a recoil implantation. Delayed IC electrons can therefore be used as a tool to reveal the decays associated with isomeric states which would otherwise be hidden under ground-state decays. This leads to the application of recoil-isomer tagging, which is discussed in Section 4.3.
The recoil implants into the DSSD of GREAT and emits IC electrons and/or α particles, which can all be detected by the DSSD (see Figure 4.4). The recoil implantations have energies of up to 14 MeV which are similar to the α-particle energies (3 to 9 MeV), however the IC electrons are emitted with much lower energies (below 900 keV). The substantial energy difference between electron events and α and recoil events makes it difficult to detect in the same detector. This difficulty is overcome using a method suggested by Jones [Jo02], where the DSSD is used to

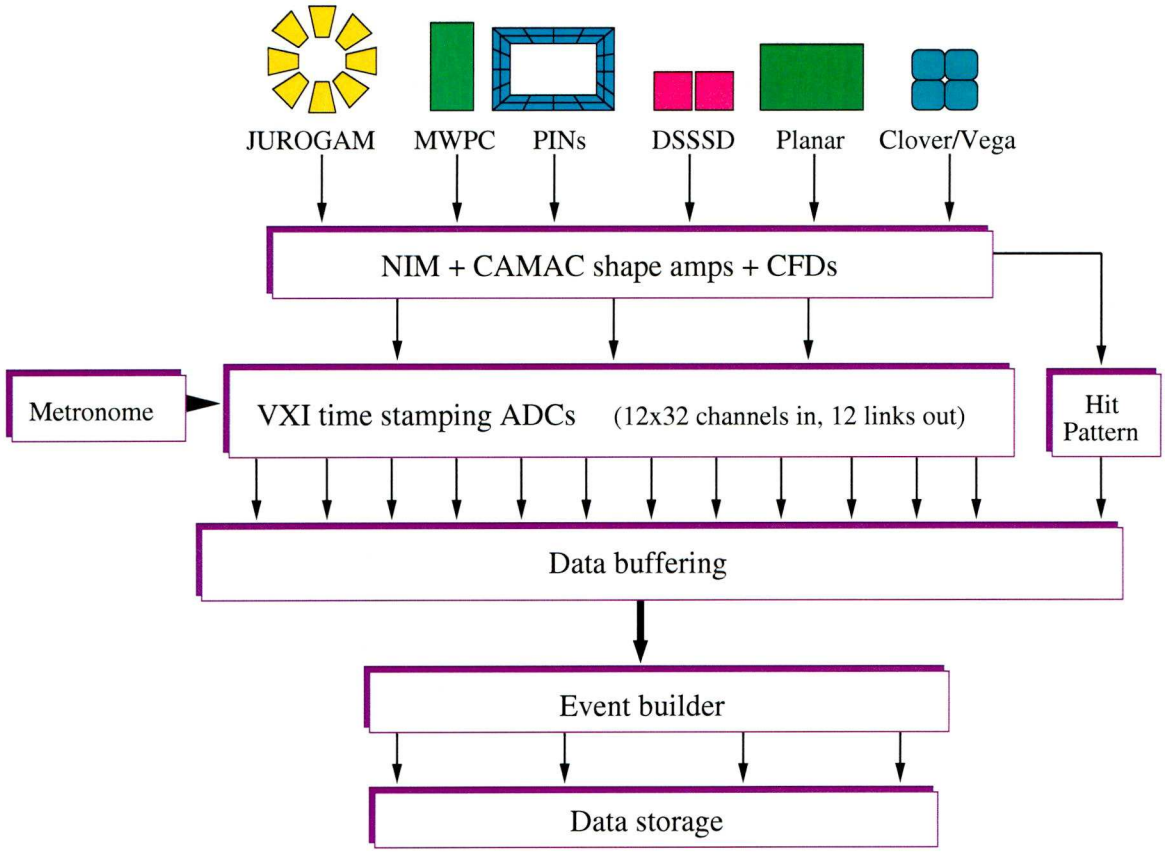

Figure 4.3: A schematic diagram of the Total Data Readout method of data acquisition system, as in [La01]. The signals from all the detectors are fed through amplifiers and CFDs before being time stamped in the Analogue-to-Digital Converters (ADCs). The event builder rebuilds the events ready for storage.

detect IC electrons whilst maintaining its ability to detect recoil implantations and α events. The location of an electron event can be identified in the DSSD, allowing correlations between recoil implantations and IC decays to be performed.
To detect α particles and recoil events the gain settings of the DSSDs are adjusted to detect an energy range of 0–20 MeV, however this means that the IC electrons would appear in a low-energy peak (0 to 600 keV). Therefore, the gain settings are adjusted so that the strips on the Y-side of the DSSDs detect events up to 20 MeV, whereas the strip on the X-side are sensitive to events with energies 0–1 MeV. If an

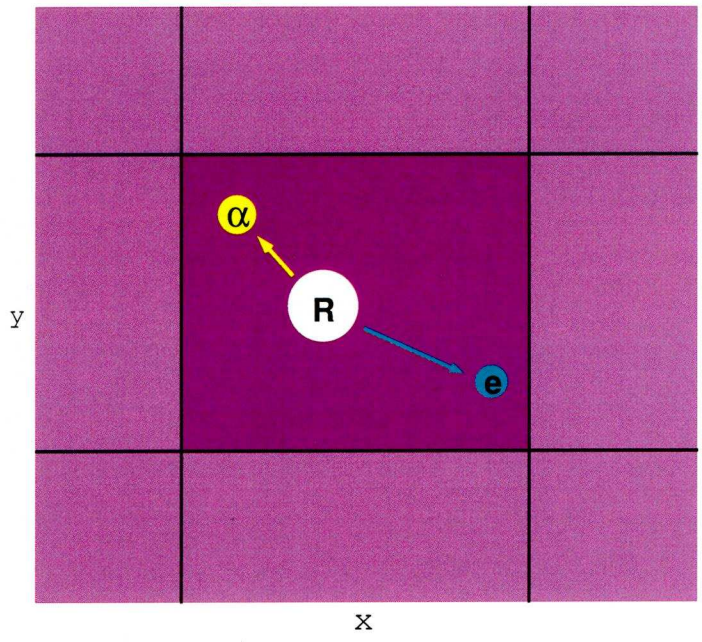

Figure 4.4: The events detected within a DSSD pixel. The α and electron decays are associated with the recoil implantation if they are detected in the same pixel within 5 half lives.

event occurs outside the respective energy ranges, the event is observed but the enrgy is not measured. For instance, the DSSD-Y energy spectrum shows the α and recoil energies, but as they are outside the range of the X-side, these events produce a high-energy peak in the DSSD-X energy spectrum, vice versa for ic events. The energy spectra of the X and Y strips are very different but the X-Y position of an event can be identified using timing measurements. For instance, an IC event is detected in an X-strip, the X-Y position is found by searching for a coincident event in the noise of the Y-strips. This allows spatial and temporal correlations to be performed and used in recoil-electron tagging, discussed in the next section.

Event	Gates/conditions
Recoil implantation	Coincident MWPC event
	TOF, MWPC energy loss and DSSD energy gates
α decay	No coincident MWPC event (Anticoincidence)
	α energy
	α half-life
IC electron	No coincident MWPC event (Anticoincidence)
	Electron energy
	Isomer half-life

Table 4.1: The gates that identify the recoil, electron and alpha events in GREAT, where signals from the MWPC and DSSD are used.

4.3 Recoil-decay tagging

The gain settings and pixellated nature of the DSSDs enables correlations between recoil implantations, α decays and IC electrons. All signals produced in the DSSD, whether α decays, electrons or recoil implantations, are referred to as 'events' and defined later in the data analysis as recoils, α or electrons if they pass certain conditions or 'gates', see the summary in Table 4.1.

Both IC electrons and γ rays are emitted in the decay of the isomeric state. These decays are delayed by about 2 s and are therefore observed at the focal plane. The flight time through the separator is known, so the delayed events can be associated with prompt γ rays at the target position. For instance, prompt γ rays are recoil-tagged if they are in delayed coincidence with a recoil implantation. The recoil-decay tagging, or RDT, method is commonly used to perform recoil-α tagging [Pa95]. Previous studies of ^{250}Fm have used recoil and recoil-α tagging techniques, which have led to the identification of the ground-state band. The objective of this study is to identify γ rays that are coincident with the isomer using the recoil-isomer tagging method described in [Jo02]. Energy and time gates are

applied to the electron events in the DSSD to select the isomeric decay of ^{250}Fm. This method is most useful at the target position where 30% of ^{250}Fm ions produced are in the isomeric state and take approximately 2 s to decay. The ground state of ^{250}Fm is produced more frequently and is therefore more prominent in the prompt recoil-tagged γ spectrum. There is no way to distinguish between γ rays from the ground and isomeric decays using only the events at the target position, instead decays at the focal plane are used to make the distinction. If the ground-state band is populated then the recoil implantation in GREAT is followed by α emissions. However, isomers populated in the reaction survive until they reach GREAT, where they emit a succession of γ rays and IC electrons followed by α decays. Therefore, a recoil implantation and a subsequent IC electron event, within a $5T_{1/2}$ time window, signifies that the isomeric state was populated and can be used to 'tag' coincident γ-ray events.

The events produced by the reaction products are summarised in Figure 4.5. When the ground-state band is populated, recoil and α events are observed at the focal plane. On average, there were 1.5 ^{250}Fm α events per minute detected in the DSSD. This translates to 45 α decays in the 30 min α decay half-life, which distributed over 4800 pixels, enables recoil-α tagging. However, it is only necessary to perform recoil-isomer tagging, where the 2 s half-life does not pose such a problem. If the recoil implants into the DSSD in an isomeric state, IC electron and α events are detected in GREAT. Recoil gates discussed Section 5.3.1 select ^{250}Fm recoil implantations. An IC electron energy gate and a 10 s time gate identifies the isomeric electrons. The recoil-isomer events identify whether the γ rays at the target were emitted from the ground state band or from above the isomeric state.

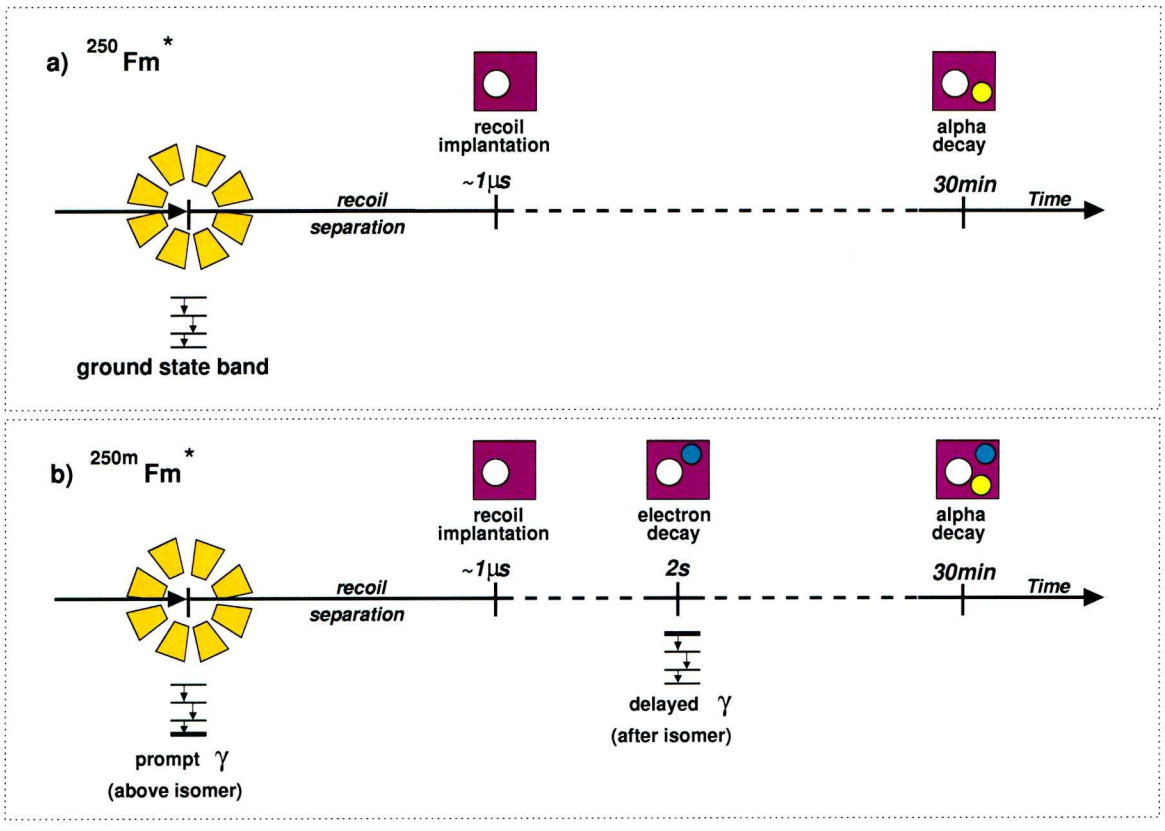

Figure 4.5: A schematic diagram of the observed events when a) the ground state band is produced and b) when the isomer is populated. The main difference is that IC electrons, in coincidence with γ rays, are observed after a recoil implantation when an isomer is produced.

Chapter 5

Data Analysis

The analysis was performed using the GRAIN package [Ra07] which reconstructs the experimental data using the spatial and temporal information. Before results are extracted from the experimental data, calibrations and preliminary measurements are carried out. To optimise the resulting histograms the detectors are calibrated individually, this is discussed in the first section (5.1) along with the Doppler Shift Correction applied to JUROGAM. The efficiency of the γ-ray detectors is discussed in Section 5.2 and is important for the accurate measurement of γ-decay intensity. Finally in Section 5.3, time and energy gates are applied in order to perform RDT measurements and to clean up the γ-ray spectra.

5.1 Calibration of the detectors

The energy of the x side of the DSSD is calibrated using the IC electrons emitted from the ^{133}Ba source, whilst a triple α source (^{239}Pu, ^{241}Am, ^{244}Cm) is used for the calibration of the y side. The calibration of the DSSD is not so important as the energies of the α decays are well established. It is instead to identify the α decay peaks for gating purposes, therefore a simple linear calibration is applied.
On the other hand, γ-ray energies are being measured accurately and so the calibration of the JUROGAM, planar and clover germanium detectors is more

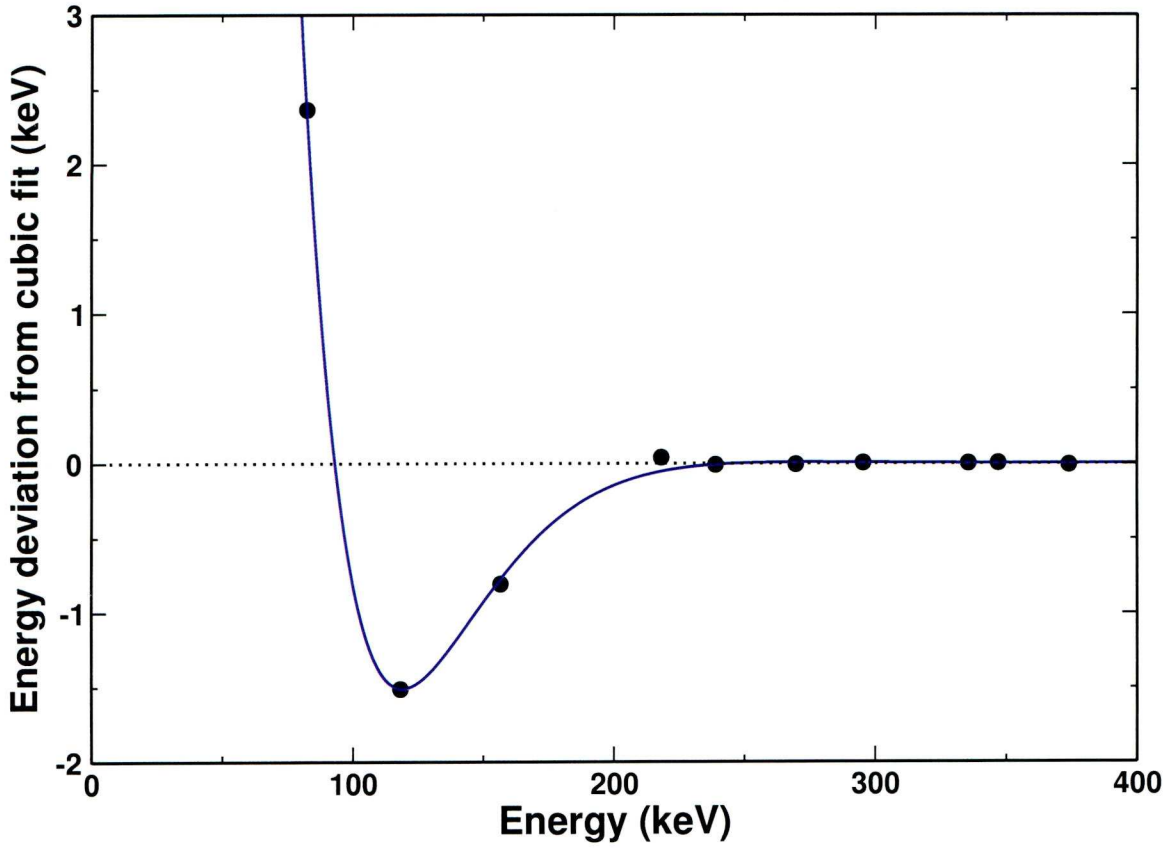

Figure 5.1: The deviations of the low-energy calibration from the cubic fit against energy for a JUROGAM detector (black points). The purple line shows how the relationship is described by a damped-sine function.

thorough. Tabulated γ-ray energies of the ^{152}Eu and ^{133}Ba sources are used to calibrate the energy scale of the γ-ray detectors. As discussed in Section 4.1, the ADCs cause the low-energy scale to vary non-linearly. This effect is eliminated using the method described below, leading to an improvement in the resolution of the γ-ray peaks in the JUROGAM and focal-plane clover detectors.

In raw JUROGAM spectra above ADC channel 2000, approximately 200 keV, the relationship between channel and energy is described well by a cubic function. However this relationship cannot be extended to the low-energy γ rays and X rays, thus the low energies are dealt with separately. The cubic fit is extrapolated down to the low-energy region and the difference between the cubic fit value and the

known value, from [Fi96], is calculated. In Figure 5.1, the ADC channel number for a JUROGAM detector is plotted against the energy deviation from the cubic fit (black points). The purple line shows a damped sine function fitted to all the data points. The complete energy-channel relationship is described by a cubic function with a damped sine correction, i.e.

$$E = \underbrace{(a + bx + cx^2 + dx^3)}_{\text{Cubic fit}} - \underbrace{(e \cdot \exp(-fx) \cdot \sin(gx + h))}_{\text{Damped-sine correction}} \tag{5.1}$$

where E is the energy, x is the channel number and parameters a to h are constants. The low-energy calibration is improved by correcting the cubic function with a damped sine function. The correction is applied to JUROGAM and the GREAT planar and clover detectors. As this non-linear effect is caused by the ADC, it will be eliminated in the future by the introduction of purely digital electronics.
As well as an energy calibration, an additional correction is required for JUROGAM measurements. The recoiling ions are moving whilst emitting γ rays, leading to a Doppler shift in γ-ray energy which is dependent on the velocity of the recoil, ν, and the angle at which the γ ray is emitted, θ. This is corrected using

$$E_\gamma = E'_\gamma(1 + \beta \cdot cos\theta), \tag{5.2}$$

where the γ-ray transition energy is E'$_\gamma$ and the Doppler shifted energy detected by JUROGAM is E$_\gamma$. The ratio ν/c is expressed as β and is calculated using the principles of energy and momentum conservation. Neglecting the evaporated neutrons, the momentum of the Ca nuclei in the beam is equal to the momentum of Fm nuclei created at the target, giving $\nu = 0.0196c$ at the centre of the target. Hence, as the angle of the JUROGAM detectors relative to the beam line is known, the γ-ray energies can be corrected.

5.2 γ-ray detection efficiency

It is important to consider the detection efficiency, especially when measuring the relative intensities of γ-ray transitions. The efficiency of JUROGAM to detect γ rays is determined using calibration sources placed at the target position, the method is discussed in Section 5.2.1. The focal-plane efficiency is more difficult to establish, as γ rays are emitted from inside the DSSD and attenuated through layers of material before being detected. For that reason, calculations performed by Andreyev et al. are used to adjust γ intensities observed in the GREAT planar and clover detectors. The simulated efficiencies for the clover and planar detectors are shown in Figure 5.2, along with the total. The absolute efficiency has been calculated using GEANT Monte Carlo simulations [An04]. There were three clover germanium detectors present for this experiment, therefore the absolute efficiency is calculated by summing the efficiencies at the three detector positions. The simulations show the planar detector to have a higher efficiency for low-energy γ-ray detection than

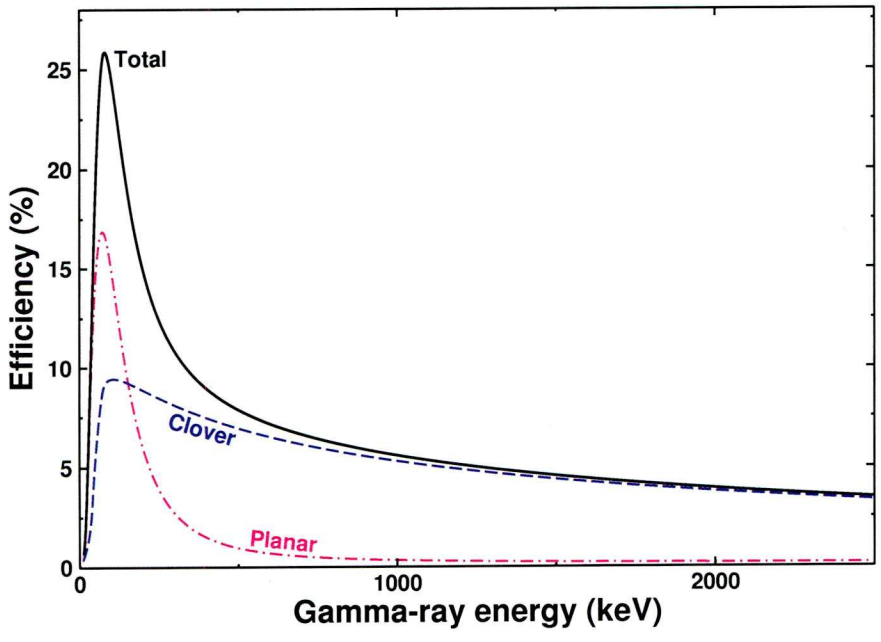

Figure 5.2: The total efficiency of γ-ray detection, calculated from the sum of the planar and clover efficiencies using GEANT Monte Carlo simulations [An04].

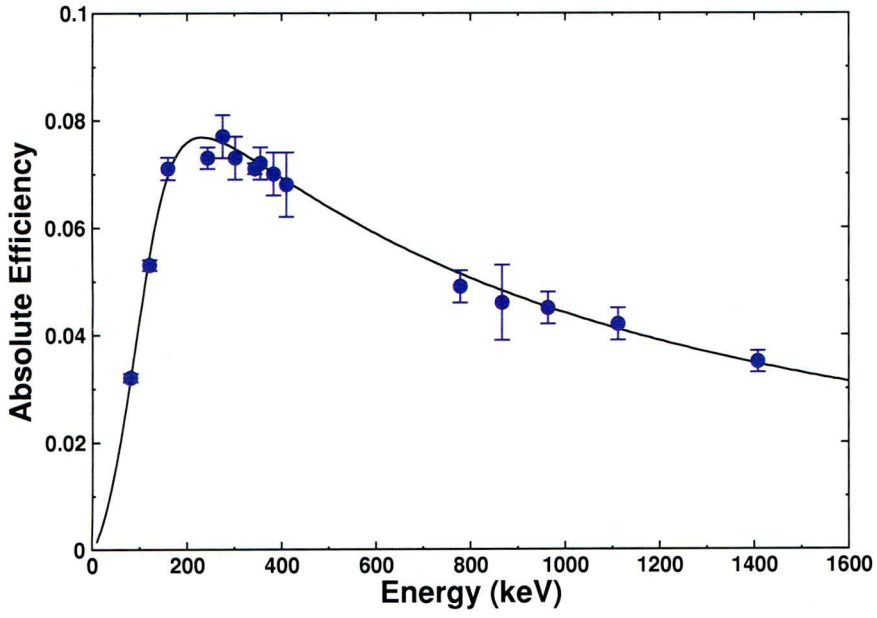

Figure 5.3: The absolute efficiency of the JUROGAM germanium array as a function of γ-ray energy. The circles are the results obtained using the calibration sources and the fit is shown as the solid line.

the clover detector. At higher energies, however, the clover exceeds the planar in detection efficiency. This leads to the application of different energy ranges on the planar and clover detectors. The energy range of the planar and clover detectors are set to 0–400 keV and 0–2 MeV respectively, in order to take advantage of the detector efficiencies. This means that the planar detector is used to detect low-energy γ rays and X rays, whilst the clover detector is used to detect the higher-energy γ rays.

5.2.1 JUROGAM efficiency measurements

To calculate the efficiency of the JUROGAM detectors, ^{152}Eu and ^{133}Ba sources were placed in the centre of the germanium array. The relative efficiency is calculated by comparing the number of γ rays detected by JUROGAM, N, when the sources are present with the tabulated intensities of the γ-rays, I, from [Fi96]. The calibration sources have known activities, A, hence the absolute efficiency, ε_{abs}, of JUROGAM

can be calculated, using

$$\varepsilon_{abs} = \frac{N}{A \cdot t \cdot I}, \tag{5.3}$$

where t is the length of time of the calibration measurement. The results are shown in Figure 5.3 along with a function that describes the experimental data. The formula of the function is

$$\varepsilon_{fit} = K \cdot \exp[(A + Bx + Cx^2)^{-G} + (D + Ey + Fy^2)^{-G}]^{-1/G}, \tag{5.4}$$

where $x = \ln(E_\gamma/100)$ and $y = \ln(E_\gamma/1000)$, and E_γ is the γ energy in keV. The fitted parameters A to K are:

A=3.81(7)	B=1.5(3)	C=0.0(0)*	D=3.81(10)
E= −0.65(4)	F= −0.17(5)	G=15.0(0)*	K=0.0097(8).

The starred parameters are fixed to 0 and 15 respectively in order to reproduce the shape of the efficiency curve. This fit is used later to correct the intensities of the observed γ ray transitions in ^{250}Fm. Note that the efficiency at 1.3 MeV was measured to be 3.6%, which is less than usually available 4.2% at JYFL, because some of the detectors where subject to noise and gain drift during the experiment.

5.3 Energy and time gates

The main reason to apply energy and time gates is to select a specific decay and be sure of its origin. As a result gating is a major part of the RDT procedure as it allows the identification of the source of a decay. It is important to validate both the recoil nuclei and the IC electrons emitted from the isomer for recoil-electron tagging. Recoil identification is achieved using the method described in Section 5.3.1, where the α decays are used to construct two-dimensional gates which identify the ^{250}Fm nuclei by their characteristic properties. Two isomers are indicated in the analysis by the half-life of IC electron decays. The α decays verify that the isomers do indeed originate from ^{250}Fm (see Section 5.3.2).

Another important application of applying energy and time gates is to reduce the number of random events and improve the peak-to-background ratio. Time gates are a crucial clean-up method at the target position where many γ rays are produced, leading to a large background. The best way to reduce the background and improve the peak-to-background ratio is to apply recoil-γ time gates. Recoil ions take a finite time to travel through RITU, therefore recoil implantations will be detected at a set time after the recoil was produced. A gate is applied to the time difference between the detection of prompt γ rays and the recoil implantation in the DSSD, which removes much of the background. At the focal plane a similar gate is applied, however it is more straightforward as the γ decays will occur in prompt coincidence with the IC electrons.

5.3.1 Recoil identification

As discussed in Section 4.3, events are identified by their characteristic signals, for example α decays are defined as DSSD strip-y events with no coincident MWPC event, also referred to as an anticoincidence condition. Figure 5.4 shows the effect of this selection by comparing the energies detected in strip-y of the DSSD both with and without the anticoincidence condition. Once the recoil decays are removed, α-decay peaks become clearer and more defined. The tabulated energies and half-lives of the α decays taken from [Fi96] are detailed in Table 5.1 along with the source of the decay. In the ^{204}Hg + ^{48}Ca reaction, both ^{250}Fm and ^{248}Fm recoil nuclei are produced, hence the α decays from these nuclei or nuclei which are part of their α-decay chains are observed. The α decays are important because they can identify the implanted recoil nucleus.

The MWPC is used in conjunction with the DSSD to identify the recoiling nuclei entering GREAT . The ^{250}Fm α events, defined by their energy and half-life, are used to establish which events are ^{250}Fm recoil implantations. Three properties of the recoil nuclei are measured:

1. The time-of-flight (TOF) of the recoil between the MWPC and the DSSD .

α decay	Energy (keV)	Intensity of α (%)	Half-life	Source
^{250}Fm	7430 (20)	83 (calc)	30 (3) m	reaction product
^{246}Cf	6750.2 (10)	79.3 (10)	35.7 (5) h	^{250}Fm α-decay daughter
	6798.4 (10)	20.6 (10)		
^{242}Cm	6112.72 (8)	74.0 (5)	162.8 (2) d	^{250}Fm α-decay granddaughter
	6069.42 (12)	25 (5)		
^{248}Fm	7870 (20)	~80	36 (3) s	reaction product
	7830 (20)	~20		
^{244}Cf	7213 (2)	75 (3)	19.4 (6) m	^{248}Fm α-decay daughter
	7176 (4)	25 (3)		

Table 5.1: The tabulated energy and half-life of all the α decays observed in Figure 5.4 taken from [Fi96].

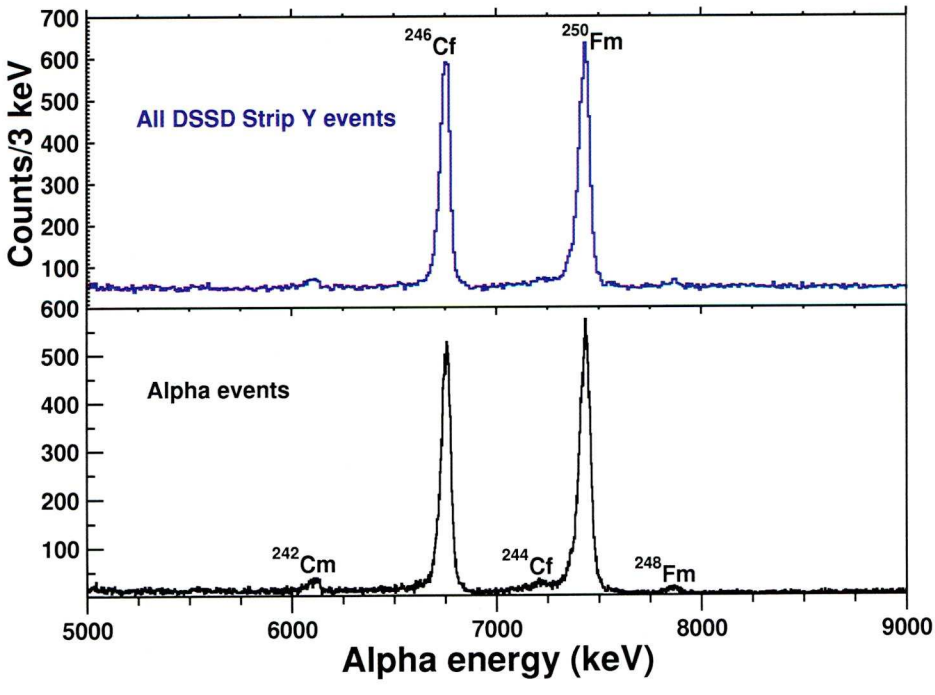

Figure 5.4: The energy of the recoil and α decays detected in strip-Y of the DSSD (purple). The α decays are selected by applying an MWPC anticoincidence gate (black).

2. The energy loss of the recoil through the MWPC.

3. The energy that is deposited by the recoil when implanting into a DSSD strip.

In Figure 5.5 the 2D matrices show how each of these measurements relates to the other by plotting TOF vs. energy loss ((a) and (b)), strip energy vs. TOF ((c) and (d)) and strip energy vs. energy loss ((e) and (f)). The three matrices (a), (c) and (e) show all the recorded events, whereas matrices (b), (d) and (f) show only events that are followed by ^{250}Fm α decays in the DSSD , which are labelled as ^{250}Fm recoil implantations. The dotted lines represent the gates applied in GRAIN to select ^{250}Fm recoil ions. The α decays highlight the characteristic signals of the implanting ^{250}Fm recoil nuclei and are therefore used to define ^{250}Fm recoil gates.

5.3.2 Isomer identification

Recoil gating, signifying the occurrence of a recoil implantation, is used in conjunction with electron gates to identify decays coincident with the ^{250}Fm isomer. Whether at the target position or the focal plane, both energy and time gates can distinguish events which are associated with the isomer. The energy gate is determined by the energy of the IC electrons (<900 keV) whilst the time gate is determined by the isomer $T_{1/2}$ and is set to $5T_{1/2}$. The α decays are used to verify that the IC decays originate from the ^{250}Fm nucleus. Figure 5.6 shows four α decay spectra with various tagging conditions that show α decays originating from different decay chains. Figure 5.6a shows the α decays which follow a recoil implantation in the same pixel of the DSSD, as were observed in Figure 5.4. The other spectra shown in Figure 5.6 show α decays that occur within 60 min of recoil implantations. In Figure 5.6b the intensity of the ^{246}Cf peak is reduced, showing the effect of the recoil-α time gate. Figure 5.6c and Figure 5.6d both show α decays which follow recoil-isomer events but with different time gates, referring to the different half lives of the two isomers. Figure 5.6c shows α decays following 2 s isomers and 60 min recoils, whilst Figure 5.6d shows α events following 6 µs-isomers

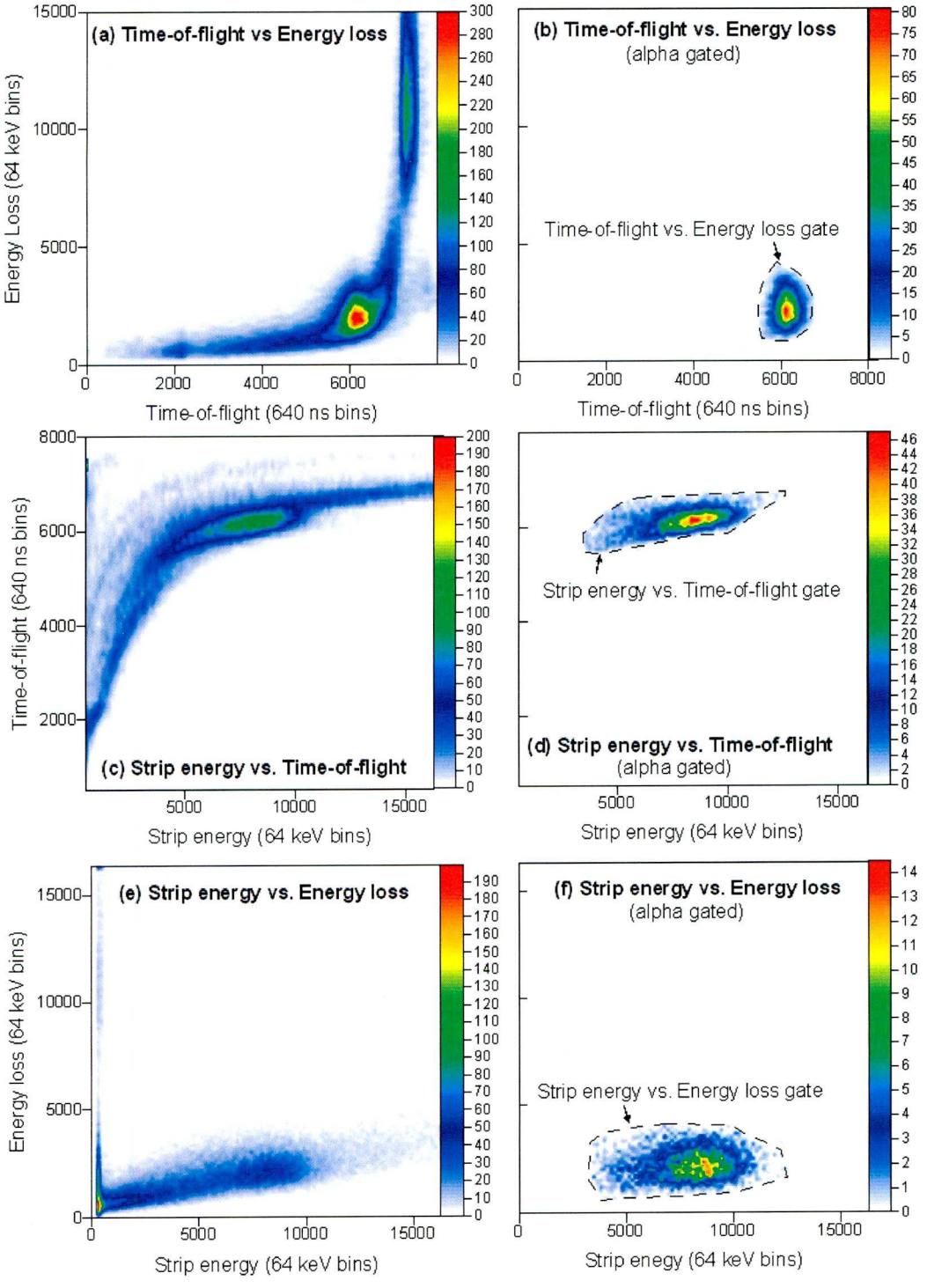

Figure 5.5: The total energy of the recoils, the energy loss of the recoils through the MWPC and their time-of-flight characterise the recoils entering GREAT. The relationship of these properties to one another for all events are shown in the 2D matrices (a), (c) and (e). The ^{250}Fm alpha gated matrices (b), (d) and (f) demonstrate the signals produced by the ^{250}Fm recoils.

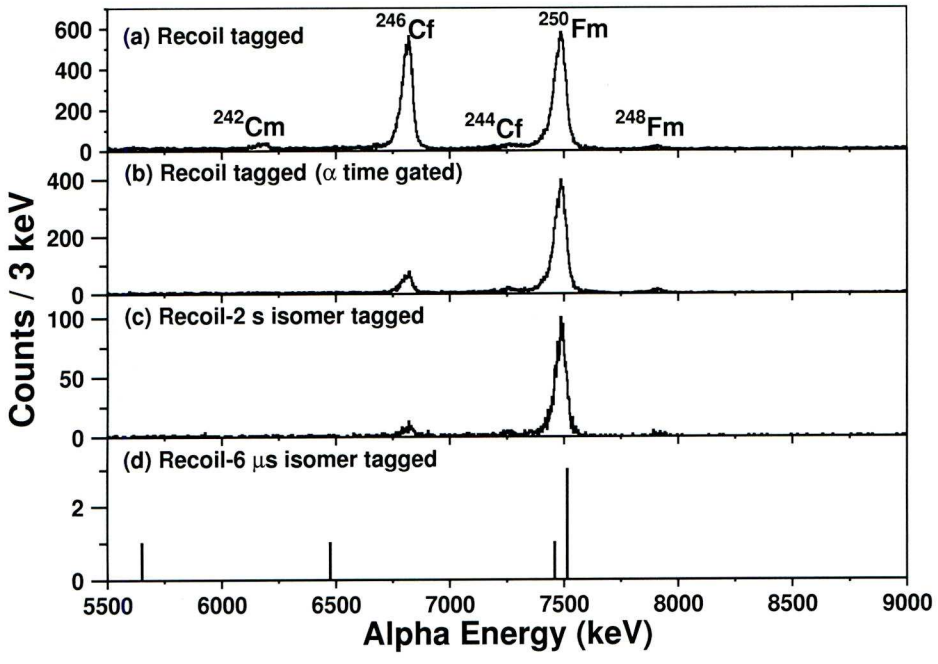

Figure 5.6: The α decays observed after (a) a recoil implantation and (b) a recoil within 60 min. The α decays in (c) and (d) follow a recoil implantation, within 60 min, and a IC electron with (c) a 2 s half-life and (d) a 6 μs halflife.

and 60 min recoils. The α energies observed in the recoil-electron tagged spectra confirm that both isomers originate from ^{250}Fm, supporting further recoil-electron tagging and coincidence analysis.

5.4 Analysis of γ rays

The energies and intensities of the tagged γ rays are measured using the TV package [Th93]. An example of the fit applied in TV is shown in Figure 5.7. The data is shown in black with the gaussian fit overlaid in blue. To perform the fit some information about the peak is needed. Firstly, the dashed red lines mark regions of background input by the user, TV then estimates the background for the intervening regions (solid red line). The limits of the peak are also input, along with the number of peaks present, which is useful if two peaks overlap or are very close together. The program is able to perform a gaussian fit to the data using this information. Energy,

intensity and width of the peak are output and used in the analysis in Chapter 6. The low cross-section of the reaction means that γ-ray statistics are low and that γ-γ coincidence measurements are inconclusive. However, gating on transitions is informative if the resulting spectra are added together. Multiple energy gates are applied to spectra to select the γ-ray transitions in a band. The resulting spectrum can identify other transitions in coincidence with the band.

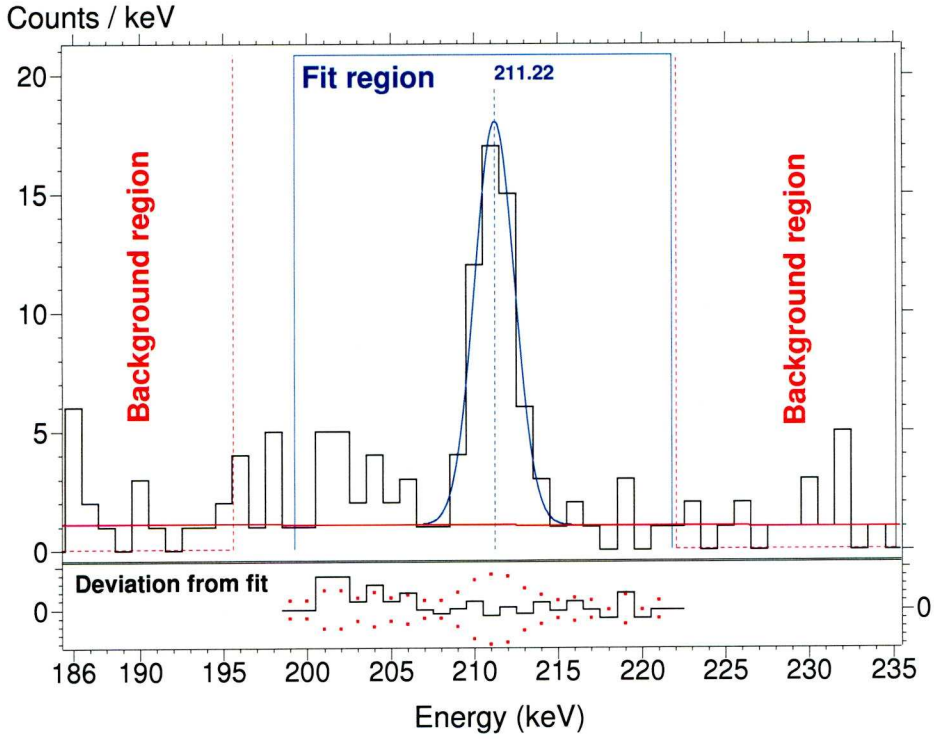

Figure 5.7: A gaussian fit performed in TV, the background (red) and fit (blue) regions are indicated. The bottom panel shows the deviation of the data from the fit.

Chapter 6

Results

The majority of ^{250}Fm evaporation residues that are created in the reaction are excited into their ground-state band, and decay promptly at the target position. However, approximately 30% of the ^{250}Fm evaporation residues are isomeric and these are transported to the focal-plane detectors in one of the isomeric states. Internal conversion (IC) decays compete with γ decays especially for low-energy transitions in heavy nuclei, as discussed in Section 2.4. Therefore recoil implantations at the focal plane followed by IC electron events, indicate that a ^{250}Fm implant is isomeric and the focal-plane γ rays which are coincident with IC electrons are emitted in the isomeric decay. Furthermore, the information is used to identify γ rays associated with the creation of ^{250}Fm isomers at the target position. This pinpoints the γ rays which are emitted before the isomeric state is populated, allowing one to explore the structure populated above the isomer for the first time. Two isomeric states have been established in ^{250}Fm, with half lives 1.93(5) s and 9(1) μs (Section 6.1). The 9(1) μs isomer cannot be placed in the level scheme due to a lack of statistics. However, more information about the 1.93(5) s isomer is obtained from the analysis of γ rays, both at the target position, in JUROGAM, and at the focal plane, in GREAT. In Sections 6.2 and 6.4 2 bands of ^{250}Fm are newly identified using recoil-isomer tagging.

The level scheme of ^{250}Fm, known so far, is shown in Figure 6.1, where the black

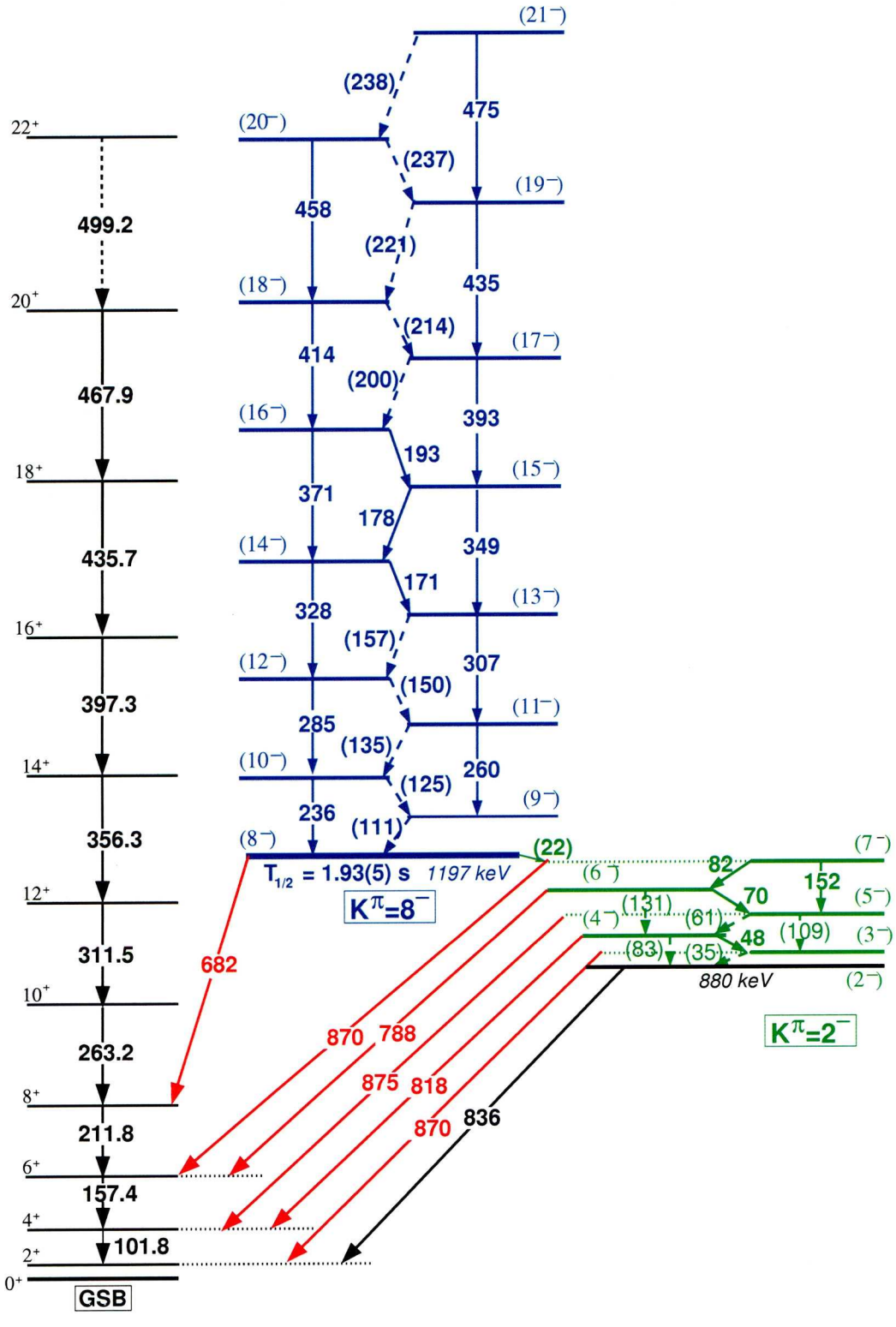

Figure 6.1: The proposed level scheme of ^{250}Fm. The black transitions/levels have been observed previously. Green transitions/levels are associated with the K=2 band whilst the K=8 band is shown in blue. Newly observed transitions that link the $K^{\pi} = 2^{-}$ and $K^{\pi} = 8^{-}$ band to the ground state are shown in red.

transitions have been observed previously. The structure and decays that are related to the $K^{\pi}=2^{-}$ band are shown in green, the $K^{\pi}=8^{-}$ band is shown in blue and the new transitions that link both structures to the ground state are in red. As a result of the γ-ray analysis, the 1.93(5) s isomer is established as the band head of a $K^{\pi}=8^{-}$ band, which is a tentatively-assigned rotational band identified up to spin 21^{-}. The isomer is found to decay via two routes: one decays to the 8^{+} level of the ground-state band (22%) via a 682 keV γ decay and the other populates a $K^{\pi}=2^{-}$ side band by an unobserved 22 keV transition (78%). In Section 6.3 hindrance values for the isomeric decays are calculated to be $f_{\nu}(22\,\mathrm{keV})$ =197 and $f_{\nu}(682\,\mathrm{keV})$ =206. The γ-ray intensities can also provide information about the structure of the bands. The γ-ray intensity ratios of $K^{\pi}=2^{-}$ and $K^{\pi}=8^{-}$ in-band transitions indicate which single-particle states form the bands. In Section 6.5 the intensity ratios of the stretched E2 to dipole transitions are calculated for the two bands in ^{250}Fm. The relationship between γ-ray intensity ratios and single-particle states, is discussed in the Chapter 7.

6.1 Isomer half-lives

The half-life of the isomeric state is measured using the DSSD at the focal plane. The recoil ions implant into the DSSD detector and, if the nucleus is in an isomeric state, conversion electrons are emitted within the DSSD. The half-life of an isomeric state is measured from the time difference between the recoil implantation and the IC electron event. There are approximately 6,000 electrons detected in the DSSD which are correlated with recoil implantations, approximately 97% of the electrons have a half live of 1.93(5) s and the rest decay with a 9(1) μs half-life. The half-life values are calculated by fitting an exponential function to the experimental data of recoil-electron time differences.

The half-life measurements of the two isomers are shown in Figures 6.2a and 6.2b, along with the corresponding energies of the electrons (inset). In the fast-isomer

(a) The (slow) 1.93(5) s isomer

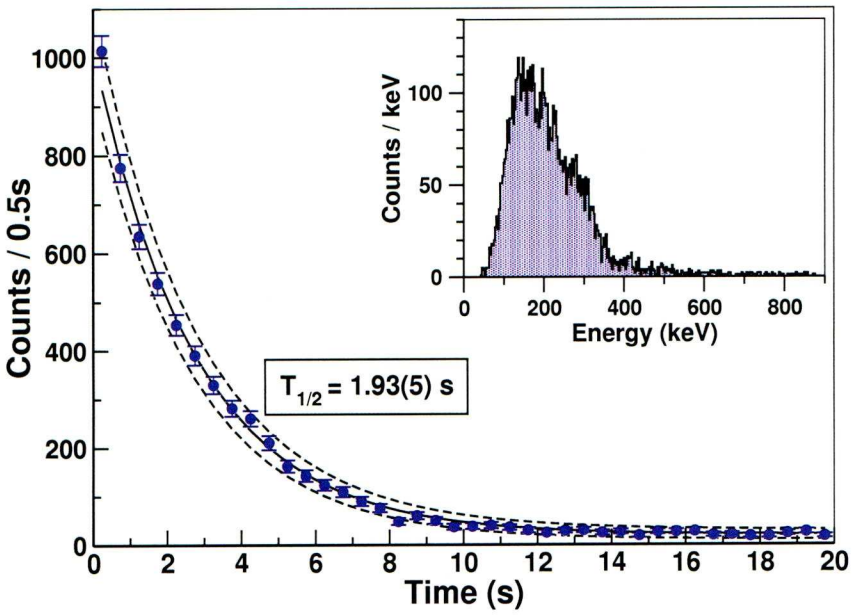

(b) The (fast) 9(1) μs isomer

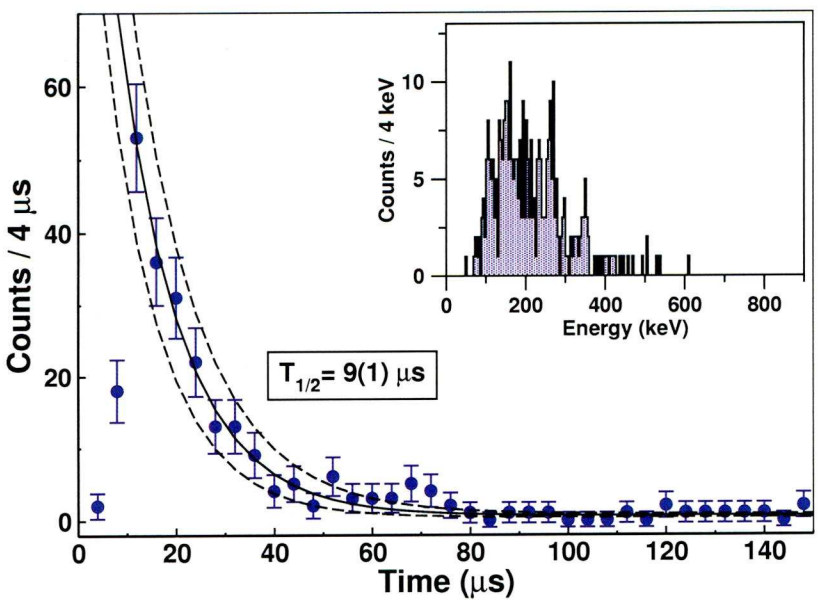

Figure 6.2: An exponential function (line) is fitted to the experimental half-life measurements (circles) for (6.2a) the 1.93(5) s and (6.2b) 9(1) μs isomers. The energy of the IC electrons is inset for each isomer.

spectrum, the first few measurements do not fit the exponential trend, this is caused by a dead time which is related to the analogue shaping and conversion time of GREAT [TD09]. The first two data points in the fast isomer spectrum were not used to obtain the half-life. The half-life, $T_{1/2}$, is calculated using an exponential function that relates the number of counts, N, to the time difference of the recoil and electron events, Δt, by

$$N = A \cdot \exp\left(\frac{\Delta t \cdot \ln(2)}{T_{1/2}}\right) + B \tag{6.1}$$

with constant A and the background B, estimated to be constant for this time scale. The 1.93(5) s half-life is consistent with the 1.8(1) s isomer which was observed by Ghiorso et al. [Gh73]. Time and energy gates are applied, establishing the prompt structure above the isomer (Section 6.4) and delayed structure following the decay of the isomeric state (Section 6.2). For the first time, γ rays have been observed in coincidence with the 1.93(5) s isomer, identifying two excited bands, see Figure 6.1. The previously unobserved 9(1) μs isomer is observed weakly with no coincident γ rays. However, the majority of fast isomer events have one more electron event stored in the tagger compared with the slow isomer. This leads to the conclusion that the 9(1) μs isomer feeds the 1.93(5) s isomer. With more statistics some related decays of the fast-decaying isomer could be established using recoil-electron tagging.

6.2 Isomeric decay: focal plane γ rays

The detection of IC electron events in the GREAT DSSD signifies that isomeric evaporation resdiues have implanted into the DSSD. The decay of the isomeric ^{250}Fm nucleus is explored by observing the recoil-electron tagged γ rays at the focal plane. GREAT has two germanium detectors—the clover and planar detectors—which are suited to detect γ rays of different energy ranges, as discussed in Section 5.2. The planar detector detects low-energy γ rays and X-rays, whilst the clover detector is configured to detect higher-energy γ rays.

All the recoil-electron tagged γ rays detected at the focal plane are shown in Figure 6.3. Figure 6.3a shows the X rays and low-energy γ rays detected in the planar detector, including Fm X rays ($L_{\alpha,\beta}$ and K_α), yrast transitions and previously unobserved γ decays. The high-energy spectrum is shown in Figure 6.3b, the γ decays observed at energies 681.7, 787.6, 817.5, 835.5 and 870.0 keV are placed in the level scheme as decays from the side band to the yrast band. The focal plane γ rays, observed in the planar and clover detectors, have led to the building of the 2^- side band and the spin-parity assignment of the isomer, discussed in Section 6.2.2. The 2^- level was assigned in previous work [Pr06], but as it is the basis of the other assignments, the reasoning is reviewed in Section 6.2.1.

6.2.1 Spin-parity assignment of the 2^- level

The statistics were too low in the previous study of ^{250}Fm [Pr06] to perform either angular distributions or $\gamma - \gamma$ coincidences, therefore the spin-parity assignment of the 2^- level is based on Weisskopf lifetime estimates, theoretical calculations and Alaga rules, the conclusions of which are supported by systematic arguments. The reasons behind the 2^- spin assignment are repeated here since the spin assignments of other levels rely upon the correct determination of the spin and parity of the 2^- level.

σL	T^W [s^{-1}]	$t^W_{1/2}$ [s]	σL	T^W [s^{-1}]	$t^W_{1/2}$ [s]
E1	$2.368(2)\times10^{15}$	$2.927(2)\times10^{-16}$	M1	$1.857(1)\times10^{13}$	$3.732(3)\times10^{-14}$
E2	$4.658(3)\times10^{12}$	$1.488(1)\times10^{-13}$	M2	$3.655(3)\times10^{8}$	$1.896(1)\times10^{-9}$
E3	$6.012(4)\times10^{7}$	$1.153(1)\times10^{-8}$	M3	$4.717(3)\times10^{3}$	$1.469(1)\times10^{-4}$
E4	$5.239(4)\times10^{-1}$	$1.323(1)\times10^{-1}$	M4	$4.111(3)\times10^{-3}$	$1.686(1)\times10^{2}$
E5	$3.259(2)\times10^{-6}$	$2.127(2)\times10^{5}$	M5	$2.556(2)\times10^{-8}$	$2.712(2)\times10^{7}$

Table 6.1: The transition probability T^W and half-life $t^W_{1/2}$ of the 835 keV transition for a range of multipolarities using Weisskopf estimates [We51].

(a) Low-energy region

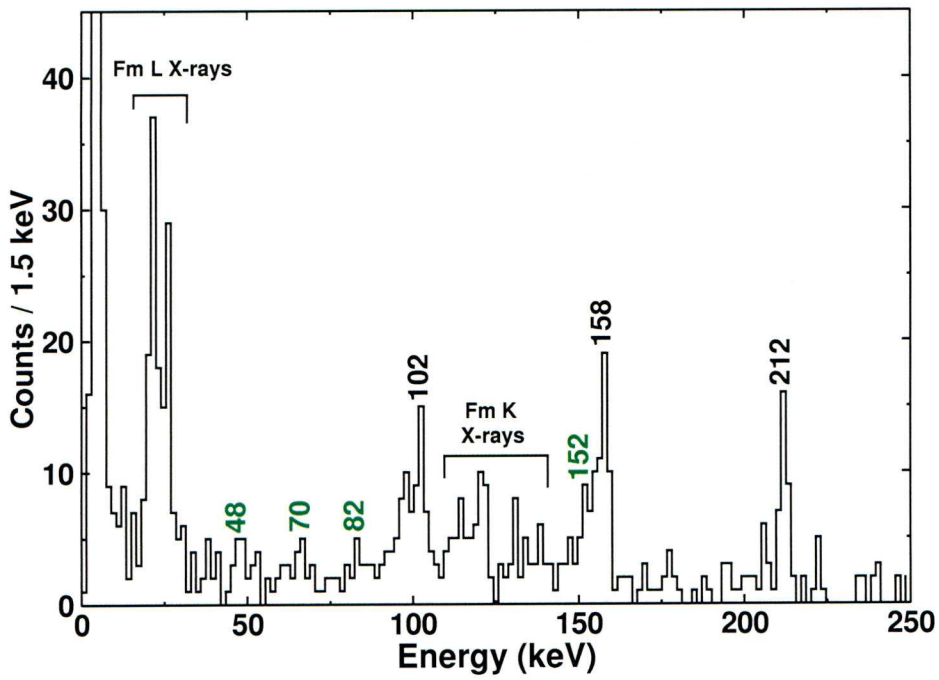

(b) High-energy region

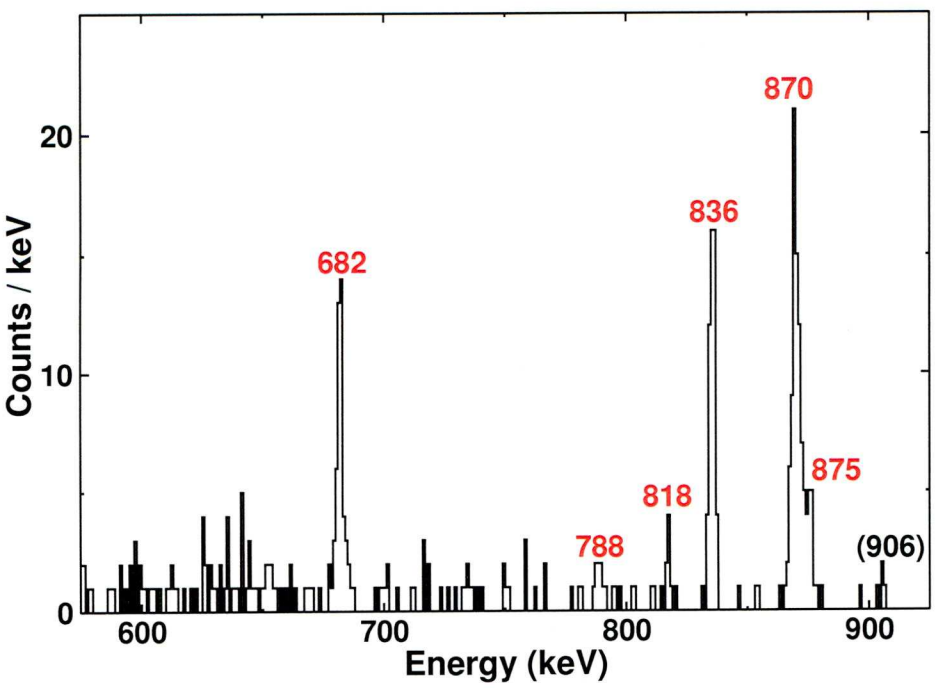

Figure 6.3: Recoil-electron tagged γ rays observed at the focal plane in 6.3a the planar detector, where the low-energy γ rays along with the $L_{\alpha,\beta}$ and $K_{\alpha,\beta}$ X-rays are observed, and 6.3b the clover detector, showing the high-energy γ-ray transitions. Ground-state transitions are observed and new γ transitions 48, 70, 82 and 152 keV γ are found to be 2^- band transitions (green).

The 835.5 keV γ ray is the only high-energy γ transition observed at the target position (see Section 6.4.1), consequently the transition must have a short lifetime. Weisskopf lifetime estimates calculated for the 835.5 keV γ transition are shown in Table 6.1. The lifetimes indicate that the transition must be of either E1, M1, E2 or M2 multipolarity in order for the γ rays to be observed at the target.
A decay from a $K^{\pi}=3^{+}$ band can be discounted when looking at the prompt γ rays. If a $K^{\pi}=3^{+}$ band exists, two γ decays to the ground-state band would be observed, which would have an energy difference equal to difference in energy between the 4^{+} and 2^{+} ground-state levels. Only one high-energy γ ray is observed at the target position, which rules out the $K^{\pi}=3^{+}$ band. A similar argument can be made for a band with $K=1$, where one would expect to observe two γ decays with an energy difference equal to $0^{+}\rightarrow 2^{+}$ yrast transition (44 keV). Furthermore, theoretical studies indicate that a 2^{-} vibrational band exists at low energy for ^{250}Fm [Ne70, Su08]. If a $K^{\pi}=2^{+}$ band exists then the γ decay is most likely to be E2 multipolarity. Alaga rules [Al55] are employed to calculate transition intensities from the $K^{\pi}=2^{+}$ state. The intensity ratio of the $2^{+}\rightarrow 4^{+}$, $2^{+}\rightarrow 2^{+}$ and $2^{+}\rightarrow 0^{+}$ decays are 5:100:70 respectively, meaning that at least two γ rays would be observed. As only one is observed, an E2 γ transition is discounted in favour of an E1 decay, which is the most likely alternative. This would therefore mean a parity change in the 835.5 keV decay, leading to the spin and parity assignment of the 2^{-} level.
The spin assignment is supported by similar bands in neighbouring even-even nuclei. $K^{\pi}=2^{-}$ bands have been found in ^{250}Cf, ^{246}Cm and ^{252}No, whereas $K^{\pi}=2^{+}, 3^{+}$ have been observed in ^{256}Fm, ^{252}Cf and ^{254}No. A trend is observed in which nuclei with 152 neutrons have positive-parity side bands and those with 150 neutrons have negative-parity side bands. As ^{250}Fm has 150 neutrons, it is likely that the band has $K^{\pi}=2^{-}$ and that the 835.5 keV transition decays from the band head.

(a) Low-energy γ rays detected in the planar detector

Transition	E_γ [keV]	$\sigma\lambda$	α	Efficiency, ε [%]	$I_\gamma(\varepsilon)$	$I(\varepsilon,\alpha)$
$4^- \rightarrow 3^-$	48 (1)	E2/M1	145 (13)	13.1	18 (6)	1298 (421)
$6^- \rightarrow 5^-$	70 (1)	E2/M1	37 (2)	16.8	14 (5)	265 (88)
$7^- \rightarrow 6^-$	82 (1)	E2/M1	21.7 (1.0)	16.7	10 (5)	108 (55)
$4^+_{\text{gsb}} \rightarrow 2^+_{\text{gsb}}$	102.1 (4)	E2	24.2 (12)	14.9	43 (11)	520 (39)
$6^- \rightarrow 4^-$	131 (1)	E2	7.7 (3)	11.6	19 (11)	80 (28)
$7^- \rightarrow 5^-$	152 (1)	E2	4.08 (13)	9.5	39 (11)	95 (28)
$6^+_{\text{gsb}} \rightarrow 4^+_{\text{gsb}}$	157.2 (3)	E2	3.56 (11)	9.1	89 (20)	196 (44)
$8^+_{\text{gsb}} \rightarrow 6^+_{\text{gsb}}$	211.9 (2)	E2	1.07 (3)	5.4	100 (24)	100 (24)

(b) High-energy γ ray detected in the clover detector

Transition	E_γ [keV]	$\alpha\ E1_{tot}$	Efficiency, ε [%]	$I(\varepsilon,\alpha)$
$8^- \rightarrow 8^+_{\text{gsb}}$	681.7 (2)	0.0099 (4)	6.19	58.8 (2)
$6^- \rightarrow 6^+_{\text{gsb}}$	787.6 (4)	0.00769 (11)	5.84	5.8 (5)
$4^- \rightarrow 4^+_{\text{gsb}}$	817.5 (3)	0.00721 (11)	5.75	7.2 (4)
$2^- \rightarrow 2^+_{\text{gsb}}$	835.5 (1)	0.00695 (10)	5.70	58.1 (2)
$7^- \rightarrow 6^+_{\text{gsb}}/3^- \rightarrow 2^+_{\text{gsb}}$	870.0 (2)	0.00648 (9)	5.61	100.0 (2)
$5^- \rightarrow 6^+_{\text{gsb}}$	875.0 (4)	0.00642 (9)	5.59	27.7 (2)

Table 6.2: Energies and intensities of the γ rays detected in GREAT. The γ-ray intensities have been normalised to the 211.9keV and 870.0keV transitions, for planar and clover γ rays respectively.

6.2.2 The $K^{\pi}=2^{-}$ band

The above arguments have established that the 835.5 keV γ ray is the decay from the band head of a $K^{\pi} = 2^{-}$ side band. The observation of the 835.5 keV transition at the target position signifies that the 2^{-} level is populated in the reaction. However, the transition is also observed in coincidence with IC electrons at the focal plane, leading to the conclusion that the isomer populates the 2^{-} level in its decay. The γ rays observed in coincidence with isomeric decays are shown in Figure 6.3. γ-ray transitions are observed at energies 681.7, 787.6, 817.5, 870.0, 875.0 and 906 keV (Figure 6.3b). The appearance of the ground-state transitions in the low-energy spectrum, Figure 6.3a, imply that the high-energy transitions link the side band to the ground-state band. The partial level scheme observed at the focal plane is shown in Figure 6.4. All the high-energy γ transitions are placed in the level scheme, except the 906 keV γ ray.

Table 6.2a shows the energies of the low-energy γ transitions with the peak intensities, normalised to the 48 keV transition intensity. The γ-ray intensities, I_{γ}, are corrected for the efficiency of the planar detector and are used to calculate γ-ray intensity ratios in Section 6.5. The total decay intensities, I, are corrected for efficiency and IC, where the multipole mixing ratio δ=0.33 is calculated assuming that the band has the same single-particle structure as the $K^{\pi}=2^{-}$ bands found in other N=150 isotones. The newly observed γ-ray transitions in the low-energy spectrum are decays in a rotational band built on the 2^{-} level, with increasing level-energy gaps. Although the statistics are low, the definite L X-ray peaks at $\sim$20 keV provide confidence in the low-energy calibration. The 48, 70, 82 keV transitions, observed in the low-energy spectrum, are assumed to be in-band transitions of the $K^{\pi}=2^{-}$ band with mixed E2/M1 multipolarity. The 70 and 82 keV transitions sum to 152 keV, as a result it is tentatively assigned as the $7^{-} \rightarrow 5^{-}$ E2 transition. The $4^{-} \rightarrow 3^{-}$ dipole transition is observed at 48 keV, implying that the energy difference between the 5^{-} and 3^{-} levels is 109 keV although a transition of this energy is not observed. More is learnt about the side

band by examining the high-energy γ decays.

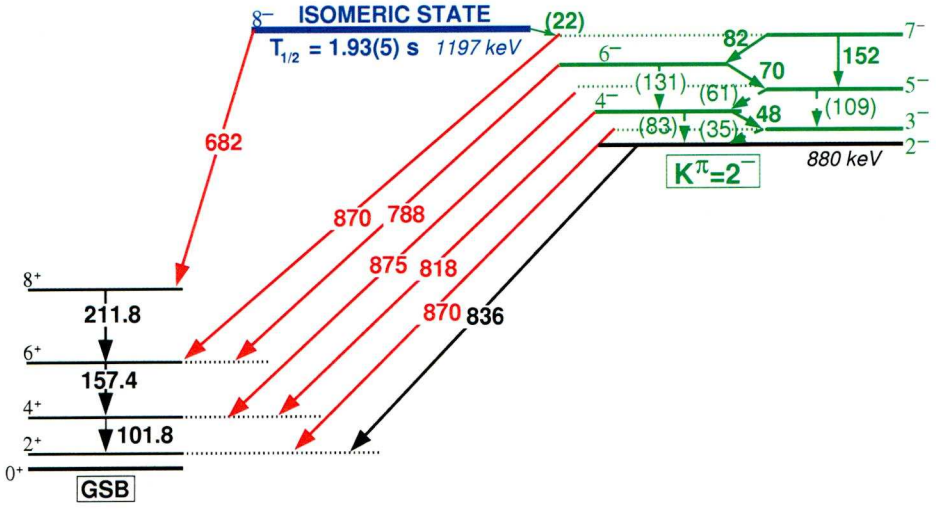

Figure 6.4: A partial level scheme of ^{250}Fm that shows the decay of the isomeric state (blue) and previously observed states and γ rays in black. The γ rays/levels associated with the $K^{\pi}=2^{-}$ band are shown in green and the high-energy interband decays are shown in red.

Table 6.2b lists the transition energies of the high-energy transitions along with the efficiency and IC corrected intensities, normalised to the 870 keV transition. Again by using energy-sum arguments, the high-energy transitions can be identified in the level scheme. The energy differences of the ground-state and 2^{-} band levels are taken into account when placing the γ rays as links between the 2 bands. For instance, there is an energy difference of 82 keV between 788 and 870 keV γ rays implying that they are transitions from the 6^{-} and 7^{-} levels ($K^{\pi}=2^{-}$) to the 6^{+}_{gsb} level. In a similar way, the 875 and 818 keV transitions are identified as the decays to the 4^{+}_{gsb} level from 4^{-} and 5^{-} levels. The 835.5 keV transition has already been assigned but the transition from the 3^{-} level to the ground-state band has not been identified previously. The 870 keV γ ray is expected to be a doublet that decays to the 2^{+}_{gsb} level from the 3^{-} level of the $K^{\pi}=2^{-}$ band.

The $4^{+}\rightarrow 2^{+}$, $6^{+}\rightarrow 4^{+}$ and $8^{+}\rightarrow 6^{+}$ ground-state transitions observed in the GREAT planar spectrum. As the $10^{+} \rightarrow 8^{+}$ ground-state transition is not observed in

coincidence with IC electrons, the isomer cannot have a spin greater than or equal to 9. Likewise the 8^+ ground-state level would not be observed if the isomeric spin is less than or equal to 7. Therefore the isomeric state is proposed to have spin and parity 8^-. The high-energy γ decays from the isomer and the $K^\pi=2^-$ band (681.7, 787.6, 817.5, 870.0 and 875.0 keV) are assumed to be stretched E1 transitions.

6.3 Isomer branching ratios and hindrance values

The 1.93(2) s ^{250}Fm isomer decays both directly and indirectly to the ground-state band. The 682 keV γ ray, detected in the GREAT clover detector, links the 8^- isomeric state directly to the 8^+ ground-state level. The isomeric state also decays to the 7^- level of the $K^\pi=2^-$ band via a 22 keV transition, which is not observed due to its low energy and high IC coefficient. However, subsequent decays from the 7^- level are observed in the form of the low-energy in-band decays and the high-energy linking transitions. It is the high-energy γ-ray intensities, in Table 6.2b, that are used to calculate the branching ratio of the 1.93(2) s isomeric decay. The γ-decay branching ratios are BR(22 keV,M1)=23(3)% and BR(682 keV,E1)=77(8)%. In addition to the measured half-life of the isomeric state, $t_{1/2}^{\text{level}}$, each decay branch has a partial γ-ray half-life which can be deduced from γ ray intensity ratios, I_γ, using

$$t_{1/2}^{\gamma} = t_{1/2}^{\text{level}} \frac{\Sigma I_\gamma (1+\alpha)}{I_\gamma} \tag{6.2}$$

where I_γ is corrected for the efficiency of the detector. The IC coefficient, α, is applied to the γ-ray intensity to obtain the sum of both γ and IC decays. Hindrance values are calculated from the ratio of $t_{1/2}^{\gamma}$ and the theoretical half-life, $t_{1/2}^{W}$, calculated from Weisskopf estimates (see Section 2.3).

The reduced hindrance values are calculated for the 682 keV E1 and 22 keV dipole transitions, using Equation 2.34. The results are shown in Table 6.3, with a summary of all the values used in the calculation. The reduced hindrance values are adjusted for the amount that the decays are forbidden. The degree to which a decay

Decay	Energy [keV]	σL	$t^{\gamma}_{1/2}$ [s]	$t^{W}_{1/2}$ [s]	$K^{\pi}_{s.b.}$	ν	f_{ν}
$8^- \rightarrow 8^+_{gsb}$	682	E1	8.58 (10)	7.75×10^{-16}	-	7	**196 (2)**
$8^- \rightarrow 7^-$	(22)	M1	577 (12)	1.79×10^{-9}	1^-	6	82.8 (17)
					2^-	**5**	**200 (4)**
					3^-	4	753 (15)
					4^-	3	6856 (140)

Table 6.3: The partial half lives, $t^{\gamma}_{1/2}$, Weisskopf half-life estimates, $t^{W}_{1/2}$, and hindrance values, f_{ν}, calculated for decays from the 8^- isomeric state. The f_{ν} value for the 22keV decay is calculated using a range of K values, $K^{\pi}_{s.b.}$, for the side band.

is forbidden is described by $\nu=\Delta K-L$, where ΔK is the change in K of the transition and L is the multipole order of the transition. Assuming that the decays from the isomeric state have E1 and M1 multipolarities, then L=1. The hindrance value for the 682 keV E1 transition is f_{ν}(682 keV,E1)=196(2), for the decay from the 8^- isomeric state to the 8^+ yrast state. Hindrance values for the 22 keV M1 decay to the side band are calculated using values of $K^{\pi}=1^-$, 2^-, 3^-, 4^- for the side band. The side band is unlikely to have $K^{\pi}=3^-$ or 4^-, due to the large hindrance values. Instead, a side band with $K^{\pi}=1^-$ or 2^- is more feasible. The hindrance value calculated for a $K^{\pi}=2^-$ band, f_{ν}(22 keV,M1)=200(4), is consistent with the value calculated for the 682 keV E1 transition directly to the yrast band. This supports the previous $K^{\pi}=2^-$ assignment of the side band in Section 6.2.1, where K=1 was discounted due to the observation of only one high-energy γ decay at the target position. The results are discussed in Section 7.1, which includes comparisons of hindrance values of similar nuclei.

6.4 Prompt γ rays in JUROGAM

The JUROGAM detector array placed around the target position detects the prompt γ rays produced in the reaction. Events at the focal plane are used to identify the

source of the prompt γ rays. For instance, a ^{250}Fm recoil implantation signifies that a ^{250}Fm* nucleus was created 1 μs earlier at the target position. All the γ rays emitted from ^{250}Fm* nuclei are observed in recoil-tagged spectra, in which the strongest decays are the ground-state transitions (see Section 6.4.1). The ground-state decay results are in agreement with those of previous studies [Pr06, Ba06].

In Section 6.4.2 the recoil-electron tagging technique is applied to ^{250}Fm γ rays at the target position for the first time. Many γ rays which are observed weakly in the recoil-tagged spectrum appear strongly in the recoil-electron tagged spectra, as the technique removes the ground-state band from spectra. The γ rays indicate a signature-split rotational band built on top of the 8^{-} isomeric state, observed for the first time. The intensities of the recoil-electron tagged γ rays are used in Section 6.5 to calculate intensity ratios of dipole and stretched E2 transitions, which are used later to compare with theoretical calculations and make single-particle assignments (Section 7.2).

6.4.1 Prompt recoil-tagged γ rays

A recoil-tagged γ spectrum is shown in the Figure 6.5. The top panel (a) shows the total recoil-tagged spectrum, where yrast decays are labelled with the transition and other decays are labelled with energy. The four large intensity peaks between 110 and 150 keV, labelled $K_{\alpha,\beta}$, are the Fermium K X-rays. The γ-ray peak at 436 keV is broad due to the Coulomb excitation of the first 2^{+} state of ^{204}Hg. The bottom panel (b) shows the γ rays coincident with yrast transitions, labelled with their energies. This shows that the known yrast decays are in strong coincidence with each other but not with the other transitions. In the high-energy spectrum (inset) a peak at 835.7 keV is observed with four possible peaks at 771, 790, 856 and 870 keV. The γ-ray peak at 835.7 keV is also observed in the delayed clover spectrum in Figure 6.3b, and has been identified as the decay from the 2^{-} level to the 2^{+} yrast state. The other high-energy decays are less intense and difficult to distinguish from

the background. However, in the focal-plane spectrum the 870 keV transition is observed strongly, implying that the 870 keV peak here is also caused by the decay from the 2^- band to the yrast band.

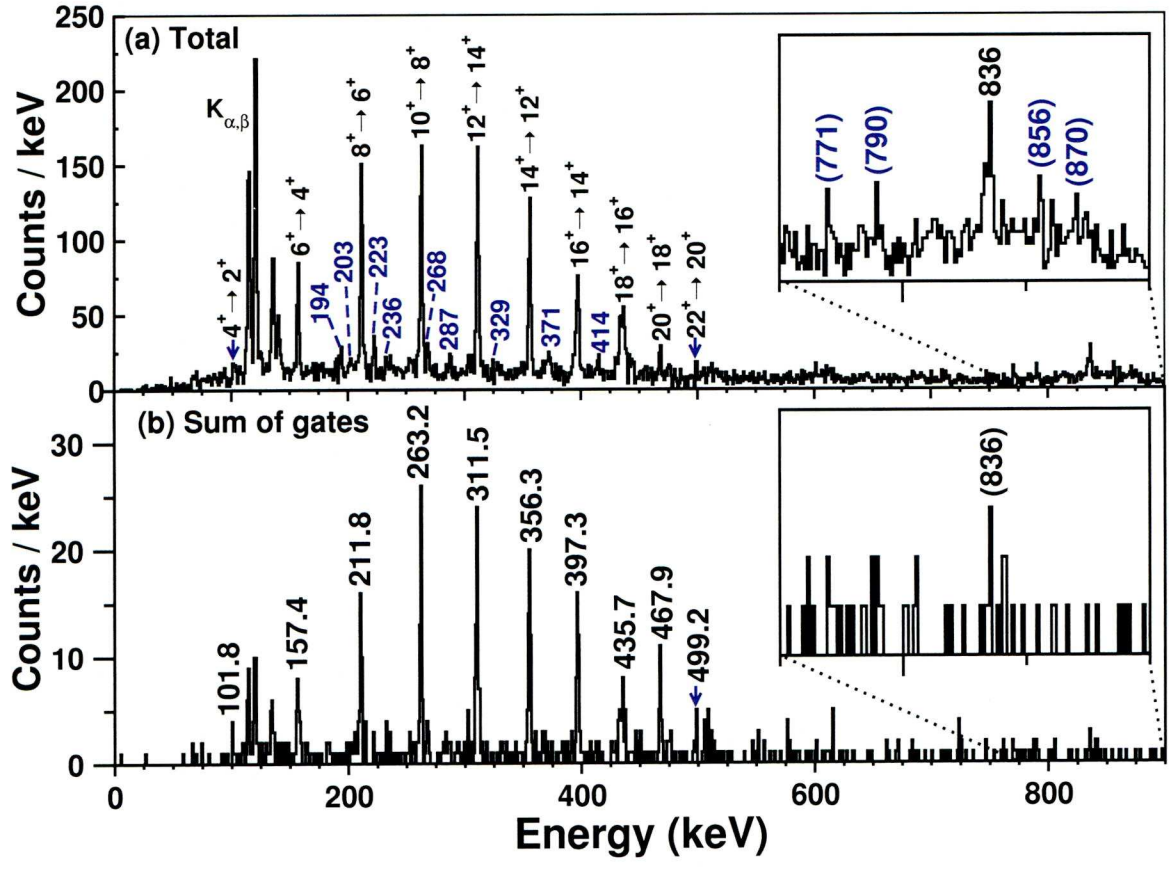

Figure 6.5: Recoil-tagged γ transitions observed with the JUROGAM array at the target position. The total γ-ray spectrum is shown in (a), yrast decays are labelled with their transition and non-yrast transitions are labelled with their energies. The γ-rays coincident with ground-state band decays are shown in (b).

Figure 6.5(b) shows the γ rays in coincidence with ground-state transitions, produced by gating on the ground-state band transition energies, listed in Table 6.4. The individual gated spectra have been summed to produce a total or 'sum of gates' spectrum. It shows that there is a coincidence between all the yrast transitions. The intensity of the K X-rays has decreased when compared with the total spectrum in Figure 6.5a, indicating that the K X-rays are related to non-yrast structures of

^{250}Fm. Table 6.4 shows the energies and relative intensities measured in the experiment. The energies of the yrast transitions are accurate to < 0.5 keV, which shows no improvement on previous results. The measured intensities of the γ rays, N_γ, are corrected for JUROGAM efficiency, ε, and IC using

$$I = \frac{N_\gamma}{\varepsilon}(1 + \alpha_{tot}) = I_\gamma(1 + \alpha_{tot}), \tag{6.3}$$

$$I_\gamma = \frac{N_\gamma}{\varepsilon}. \tag{6.4}$$

Where α_{tot} is the IC coefficient obtained from [Ki08]. To calculate the γ-ray intensities, I_γ, the measured intensity of the γ rays, N_γ, is corrected for efficiency. Correcting the intensities for the efficiency and IC yields the total decay intensity, I. In Table 6.4, both intensity calculations are normalised to the 311.5 keV γ-ray transition.

The energies and intensities of the non-yrast transitions, observed in the recoil-tagged spectrum, are listed in Table 6.5. The intensities are normalised to the K^π=8$^-$ band transition at 311.5 keV for easy comparison with ground-state transitions. All except one of the decays are identified as transitions in the 8$^-$ band built on top of the 1.93(5) s isomer, in Section 6.4.2, using recoil-electron tagging methods. The 268 keV γ decay is the only non-yrast decay to be observed in the recoil-tagged spectrum but not the recoil-electron tagged spectrum. It also appears in Figure 6.5(b), which suggests that the decay is in coincidence with the yrast decays. One possibility is that there is another structure populated in the reaction which decays promptly and populates the ground-state band.

6.4.2 Prompt recoil-electron tagged γ rays

This is the first study to apply the recoil-isomer tagging method to ^{250}Fm. A recoil implantation followed by an IC electron in GREAT signifies that ^{250}Fm was implanted in an isomeric state. However, the reaction does not produce recoiling ions in an isomeric state directly, it feeds levels above the isomeric state which decay instantly

Transition	E_γ [keV]	α_{tot}(E2)	Efficiency, ε [%]	$I_\gamma(\varepsilon)$	$I(\varepsilon,\alpha)$
$4^+ \rightarrow 2^+$	102.4 (4)	24.3	4.37	17 (5)	334 (89)
$6^+ \rightarrow 4^+$	157.4 (1)	3.52	7.83	44 (5)	156 (14)
$8^+ \rightarrow 6^+$	211.8 (1)	1.07	8.90	80 (5)	129 (7)
$10^+ \rightarrow 8^+$	263.2 (1)	0.486	8.84	95 (6)	111 (6)
$12^+ \rightarrow 10^+$	311.5 (1)	0.278	8.48	100 (6)	100 (5)
$14^+ \rightarrow 12^+$	356.3 (1)	0.185	8.07	81 (5)	75 (4)
$16^+ \rightarrow 14^+$	397.3 (1)	0.1354	7.70	58 (5)	52 (4)
$18^+ \rightarrow 16^+$	435.7 (2)	0.1058	7.36	45 (6)	39 (5)
$20^+ \rightarrow 18^+$	467.9 (2)	0.0881	7.10	18 (3)	15 (2)
$22^+ \rightarrow 20^+$	499.2 (2)	0.0751	6.87	9 (2)	7 (2)

Table 6.4: Energies and intensities of the yrast transitions in recoil-tagged spectrum. I is corrected for efficiency, ε, and IC whereas I_γ is only corrected for efficiency. All intensities are normalised to the 311.5 keV γ-ray intensity.

E_γ [keV]	Efficiency, ε [%]	$I_\gamma(\varepsilon)$
194.3 (2)	8.74	8 (2)
202.8 (7)	8.83	6 (2)
222.6 (2)	8.94	14 (3)
235.7 (9)	8.95	12 (4)
268.6 (3)	8.81	14 (3)
287.3 (2)	8.68	8 (2)
328.7 (5)	8.32	5 (2)
371.9 (5)	7.93	21 (4)
414.2 (6)	7.55	15 (4)
(771)	-	-
(790)	-	-
835.7 (4)	5.12	42 (6)
(856)	-	-
(870)	-	-

Table 6.5: Energies and intensities of non-yrast transitions in recoil-tagged spectrum. I_γ is corrected for efficiency and normalised to the 311.5 keV ground-state intensity.

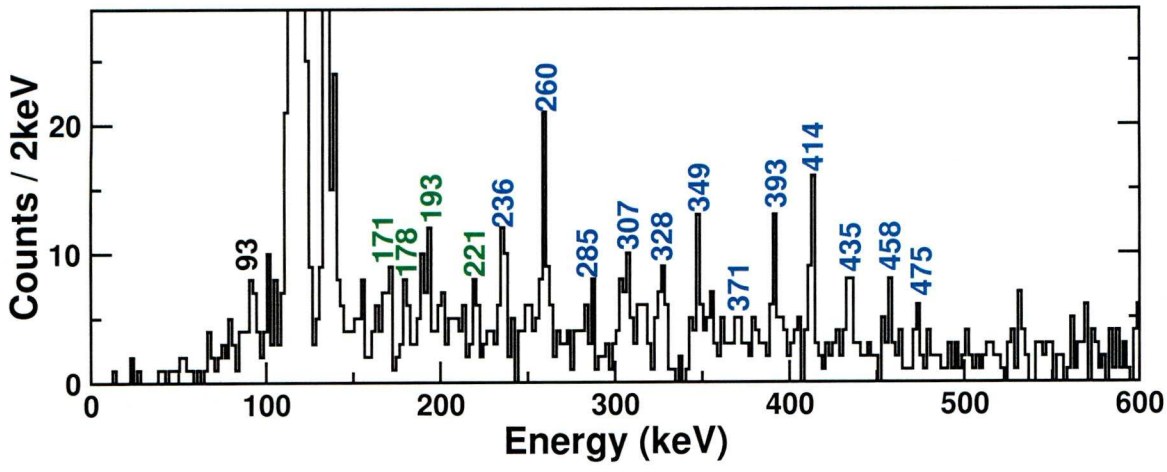

Figure 6.6: Recoil-electron tagged γ transitions observed with the JUROGAM array at the target position. Some γ-ray transitions have been tentatively assigned as stretched E2 transitions (blue), others are dipole transitions (green) of the $K^{\pi}=8^{-}$ band. The 93 keV transition (black) has not been assigned.

to the isomer. Delayed coincidences between prompt γ rays and recoil-electron events probe the structure above the isomer which is populated in the reaction. Table 6.6 lists the energies and intensities of the non-yrast transitions observed in the recoil-isomer tagged spectrum displayed in Figure 6.6. Equation 6.4 is used to correct the γ-ray intensity, I_{γ}, for efficiency. The total decay intensity, I, is corrected for efficiency and IC using Equation 6.3. A mixing ratio of δ=0.34 is used to calculate the IC coefficient for the mixed multipolarity transitions. All the intensities are normalised to the 260 keV $K^{\pi}=8^{-}$ band transition intensity. Errors are large on both the energies and the intensities, this is mainly due to the low statistics of the γ ray peaks. Despite this, a rotational band has been established, built on top of the 8^{-} isomeric state (see Figure 6.1). Most of the γ rays observed are assigned as stretched E2 transitions in the $K^{\pi}=8^{-}$ band. The low-energy 171, 178 and 193 keV transitions are placed as dipole transitions, as their energies add up to the stretched E2 transitions 349, 371 and 393 keV. The dynamic moments of inertia, $\Im^{(2)}$, are plotted against rotational frequency, ω, for the proposed $K^{\pi}=8^{-}$ band in Figure 6.7. The values are compared to the dynamic moments of inertia for

Transition	E_γ [keV]	$\sigma\lambda$	α_{tot}	Efficiency, ε [%]	$I_\gamma(\varepsilon)$	$I(\varepsilon,\alpha)$
-	93.1 (4)	-	-	3.65	68 (26)	-
$14^- \rightarrow 13^-$	171 (2)	E2/M1	9.51 (24)	8.21	22 (16)	150 (109)
$15^- \rightarrow 14^-$	178 (2)	E2/M1	7.74 (15)	8.52	32 (13)	186 (78)
$16^- \rightarrow 15^-$	192.7 (7)	E2/M1	6.54 (12)	8.72	29 (5)	145 (26)
$19^- \rightarrow 18^-$	221 (1)	E2/M1	4.45 (9)	8.94	32 (13)	117 (45)
$10^- \rightarrow 8^-$	236.4 (6)	E2	0.709 (12)	8.94	59 (17)	67 (19)
$11^- \rightarrow 9^-$	260.4 (6)	E2	0.504 (9)	8.86	100 (25)	100 (25)
$12^- \rightarrow 10^-$	283.7 (14)	E2	0.376 (9)	8.71	37 (15)	34 (13)
$13^- \rightarrow 11^-$	307.4 (20)	E2	0.290 (5)	8.51	60 (19)	51 (16)
$14^- \rightarrow 12^-$	327.7 (7)	E2	0.237 (4)	8.33	32 (15)	27 (12)
$15^- \rightarrow 13^-$	348.8 (4)	E2	0.197 (3)	8.14	50 (15)	40 (12)
$16^- \rightarrow 14^-$	371.0 (6)	E2	0.164 (3)	7.93	50 (13)	39 (10)
$17^- \rightarrow 15^-$	392.5 (4)	E2	0.140 (2)	7.74	55 (16)	42 (13)
$18^- \rightarrow 16^-$	413.9 (4)	E2	0.121 (2)	7.55	68 (19)	51 (14)
$19^- \rightarrow 17^-$	435.3 (5)	E2	0.106 (2)	7.37	49 (16)	36 (12)
$20^- \rightarrow 18^-$	458.5 (6)	E2	0.093 (1)	7.18	32 (13)	23 (9)
$12^- \rightarrow 10^-$	474.5 (7)	E2	0.085 (1)	7.05	26 (12)	19 (8)

Table 6.6: Energies and intensities of the 8^- band transitions, as measured by JUROGAM. The intensity I is corrected for efficiency, ε, and IC whereas I_γ is only corrected for efficiency. Both intensities are normalised to the 260.6 keV γ-ray intensity.

the ground-state band and the $K^\pi=2^-$ band.

The assignment of the 171, 178 and 193 keV transitions fixes the energy values of the other dipole transitions in the band. Most of the dipole transitions are not observed, but a γ ray is observed at 221 keV, which is assigned as the $19^- \rightarrow 18^-$ mixed transition. The lowest energy $\Delta I=1$ are hidden underneath Fm X-rays between 115 and 140 keV. Higher energy $\Delta I=1$ transitions are hidden under the

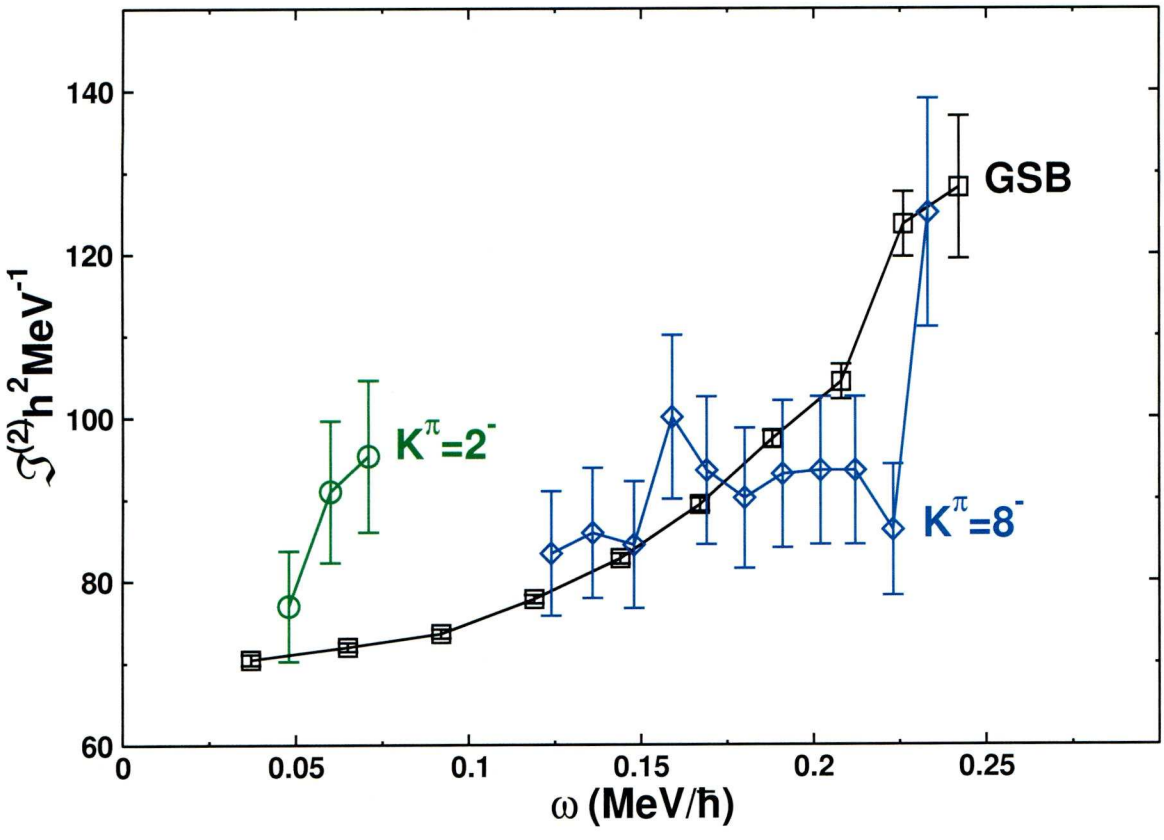

Figure 6.7: The dynamic moment of inertia, $\Im^{(2)}$, against the rotational frequency, ω, of the ground-state, $K^\pi=2^-$ and $K^\pi=8^-$ bands.

stronger E2 transitions. The γ-ray intensity ratios of $\Delta I=1$ compared to stretched E2 transitions are calculated for 14^-, 15^- and 16^- levels in Section 6.5. These are used to make single-particle assignments in Section 7.2.

6.5 Intensity ratios of intra-band transitions

The ratios calculated here are used in Section 7.2 to constrain the gyromagnetic ratios, g_K, of the band. The experimental g_K values are compared to those of possible single-particle states. This yields unambiguous single-particle assignments for the two excited bands of ^{250}Fm.

The $K^\pi=8^-$ signature-split rotational band is built on top of the isomeric state.

Figure 6.6 shows the γ rays observed in the 8^- band, with most transitions assigned with E2 multipolarity. There are four low-energy γ transitions at energies 171, 178, 193 and 221 keV, which have been assigned as ΔI=1 dipole transitions between the signature partners. The other dipole transitions are unobserved either due to high conversion coefficients or because they cannot be resolved from strong γ or X ray transitions. The observation of two γ transitions from each of the 14^-, 15^- and 16^- levels allows the experimental branching ratios,

$$R_{ex} = \frac{I_\gamma(I \rightarrow I-1)}{I_\gamma(I \rightarrow I-2)}, \tag{6.5}$$

to be calculated, for the decays of states with spin I and intensity I_γ. The experimental ratios R_{ex} of the K^π=8^- band are calculated using the γ-ray intensity ratios shown in Table 6.6.

Dipole and stretched E2 multipolarity transitions are also observed from the same state in the K^π=2^- side band in Figure 6.3a. High conversion coefficients make it difficult to observe the low-energy transitions. Indeed only one E2 transition and three dipole multipolarity transitions are observed in this band: the 48, 70 and 82 keV (dipole) transitions and the 152 keV transitions. Hence, the value of R_{ex} is calculated for the 7^- state of the K^π=2^- side band in ^{250}Fm, using intensities in Table 6.2a. All the R_{ex} values calculated for the bands in ^{250}Fm are shown in Table 6.7. A comparison of these results with theoretical values leads to single-particle assignments in Section 7.2.

Band	Initial level	$I_\gamma(E_\gamma)/I_\gamma(E'_\gamma)$	R_{ex}
2^-	7^-	$I_\gamma(82)/I_\gamma(152)$	$0.25^{+0.29}_{-0.16}$
	14^-	$I_\gamma(171)/I_\gamma(328)$	$0.7^{+1.4}_{-0.6}$
8^-	15^-	$I_\gamma(178)/I_\gamma(349)$	$0.6^{+0.7}_{-0.4}$
	16^-	$I_\gamma(193)/I_\gamma(371)$	$0.6^{+0.3}_{-0.2}$

Table 6.7: The experimental intensity ratios R_{ex} for all measurable levels of the K^π=2^-, 8^- bands of ^{250}Fm.

Chapter 7

Discussion

$K^\pi=2^-$ and $K^\pi=8^-$ bands are observed in ^{250}Fm with band heads located at 880 keV and 1197 keV, respectively. The band-head of the 8^- band is isomeric with a 1.93(5) s half-life, confirming the observation of the 2 s isomer by Ghiorso et al. [Gh73]. The recoil-electron tagging method has made it possible to observe the rotational structure of both excited bands. Furthermore, the intensity ratios, R_{ex}, are calculated for $\Delta I=1$ and $\Delta I=2$ decays from the same state. In Section 7.2, the R_{ex} values are used to determine gyromagnetic ratios, g_K, which are then compared to theoretical single-particle g_K values. The 8^- band is assigned as a two-neutron quasiparticle excitation with configuration $\left\{\frac{7}{2}^+[624]_\nu \otimes \frac{9}{2}^-[734]_\nu\right\}^{8-}$, whilst the 2^- band is dominated by the $\left\{\frac{9}{2}^-[734]_\nu \otimes \frac{5}{2}^+[622]_\nu\right\}^{2-}$ two-quasiparticle structure. The reduced hindrance values are also discussed in Section 7.1.

The experimental results for ^{250}Fm are compared to similar observations in the $N=150$ and $N=152$ isotones in Section 7.3. The systematic data has implications for the single-particle structure in the deformed region around ^{250}Fm. These results provide more experimental evidence for the $N=152$ and $Z=100$ shell gaps for deformed nuclei. The energies and configurations of excitations observed in these nuclei are excellent tests for model calculations.

7.1 Hindrance values

The 8^- isomer of ^{250}Fm exists due to a spin trap, discussed in Section 2.6. In order for the K-isomer to decay, the nucleons need to realign along the symmetry axis to generate a change in K. In ^{250}Fm the isomer must undergo a change in K of either ΔK=6 to decay to the side band or ΔK=8 for a decay to the ground-state band. The transition rates for these decays depends on the degrees of forbiddenness ($\nu = \lambda - \Delta K$), it was found that they reduce by a factor of 100 for each extra unit of ν [Lo68]. Calculating the reduced hindrance values, f_ν, eliminates the dependence on ν and allows for the comparison of transitions with different degrees of forbiddenness. The hindrance values vary considerably from a 10 to several 100, with a rough estimate $f_\nu \approx$100.

In Section 6.3 the reduced hindrance values of the 8^- isomeric decays are calculated to be $f_\nu(\Delta K$=6,M1)=200(4) and $f_\nu(\Delta K$=8,E1)=196(2). The hindrance values are in the expected range and the values are similar, indicating that the assigned multipolarity of the transitions are correct. Similar f_ν values are observed for the isomers of other nuclei in the region. f_ν values are calculated for the two decays from the 8^- isomer of ^{254}No, $f_\nu(\Delta K$=8,E1)=210 and $f_\nu(\Delta K$=5,E1)=804 [Ta06, Gr08]. For the decay from the 8^- isomer of ^{252}No to the 2^- side band, $f_\nu(\Delta K$=6,M1)=140 [Su07]. Studies of the Hafnium (Z=72) isomers found that reduced hindrance values increase with mass number due to the variation in K-mixing [Wa94]. Although they are in different regions of the nuclear chart, the f_ν values in the ^{250}Fm region are higher than for the lighter Hafnium isotopes, which is in line with the increasing trend for larger nuclei.

7.2 g_K values

The γ-ray intensity ratios, R_{ex}, measured in Section 6.5, are used to determine g_K for the K^π=2^- and K^π=8^- bands. For the collective transitions in the rotational bands built on top of the quasiparticle excitations, the ratio of ΔI=1 to ΔI=2 γ

transitions depends strongly on the g_K value of the band. The experimental result R_{ex} gives two possible g_K values, which are compared to the g_K values for possible quasiparticle excitations. This comparison unambiguously establishes that the K^π=8$^-$ band is formed by the $\frac{7}{2}^+[624]_\nu \otimes \frac{9}{2}^-[734]_\nu$ configuration and the K^π=2$^-$ band is dominated by the $\frac{9}{2}^-[734]_\nu \otimes \frac{5}{2}^+[622]_\nu$ configuration. Details of the calculations are now explained, along with the reasoning behind the assignments. The g_K values are calculated using the geometric collective model of the nucleus, discussed in Section 2.3. The collective transition probabilities, $T(\sigma L)$, for collective M1 and E2 transitions are

$$T(M1) = 1.779 \times 10^{13} E_\gamma^3 B(M1) \tag{7.1}$$

$$T(E2) = 1.223 \times 10^{9} E_\gamma^5 B(E2), \tag{7.2}$$

taken from Table 2.1, where $B(\sigma L)$ are the reduced transition probabilities for collective decays, calculated using Equations 2.23 and 2.24 by the program BM1BE2 [Pa09] which uses equations described in [Dö83, Dö87]. The probabilities $B(\sigma L)$ depend on the electric quadrupole moment, Q_0, and the g factors, g_K and g_R, where Q_0=12.6 eb and g_R=Z/A=0.4 for ^{250}Fm. The calculations are repeated with a quenching factor of 0.8 applied to g_R(=0.8×Z/A=0.32). The quenching value of 0.8 is based on the g_R values measured for first 2$^+$ states in even-even nuclei shown in Figure 7.1, where rotational nuclei with 140≤A≤200 are found to have values consistently lower than g_R=Z/A [Bo99].

The intra-band transitions are collective in nature but the band heads are caused by two-quasiparticle excitations. The experimental intensity ratios and g_K values are compared to the theoretical values for possible two-quasiparticle excitations in Figures 7.2 and 7.3. The g_K values of the single-particle orbitals involved in the excitations are calculated using the *swbeta* program [Ćw87]. As there are two single-particle orbitals involved in these excitations, the values are combined to give the g_K values of the excitations. The g_K value of a two-quasiparticle excitation, g_J, with spin J, is calculated from the g_K values of the single-particle states using the

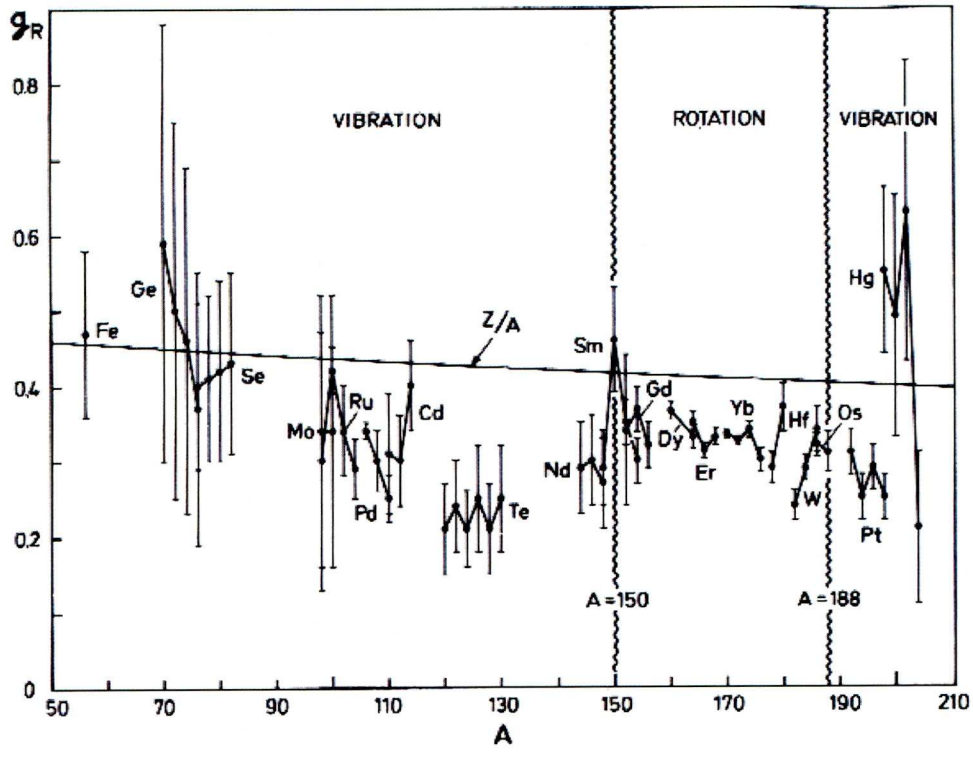

Figure 7.1: The g factors for the first excited 2^+ states in even-even nuclei, taken from [Bo99].

Landé formula

$$g_J = \frac{1}{2}(g_1 + g_2) + \frac{1}{2}(g_1 - g_2)\left[\frac{j_1(j_1+1) - j_2(j_2+1)}{J(J+1)}\right] \tag{7.3}$$

where g_1 and g_2 are the g_K values of the quasiparticle states and j_1 and j_2 are their spins [Kr88]. Experimental results for the K^π=8^- band are compared to two-quasiparticle configurations: $\frac{7}{2}^+[624]_\nu \otimes \frac{9}{2}^-[734]_\nu$ and $\frac{9}{2}^+[624]_\pi \otimes \frac{7}{2}^-[514]_\pi$, which have$g_K$ values -0.03 and 1.02 respectively. There is only one two-quasiparticle excitation for the K^π=2^- band, the $\frac{9}{2}^-[734]_\nu \otimes \frac{5}{2}^+[622]_\nu$ configuration with g_K= -0.31. There are no two-proton quasiparticle configurations predicted at low energies with K^π=2^- for ^{250}Fm.

The results for the K^π=2^- and K^π=8^- bands are shown in Figures 7.2 and 7.3 respectively, for both unquenched and quenched calculations. There are three measurable intensity ratios for the K^π=8^- band. The errors on the experimental

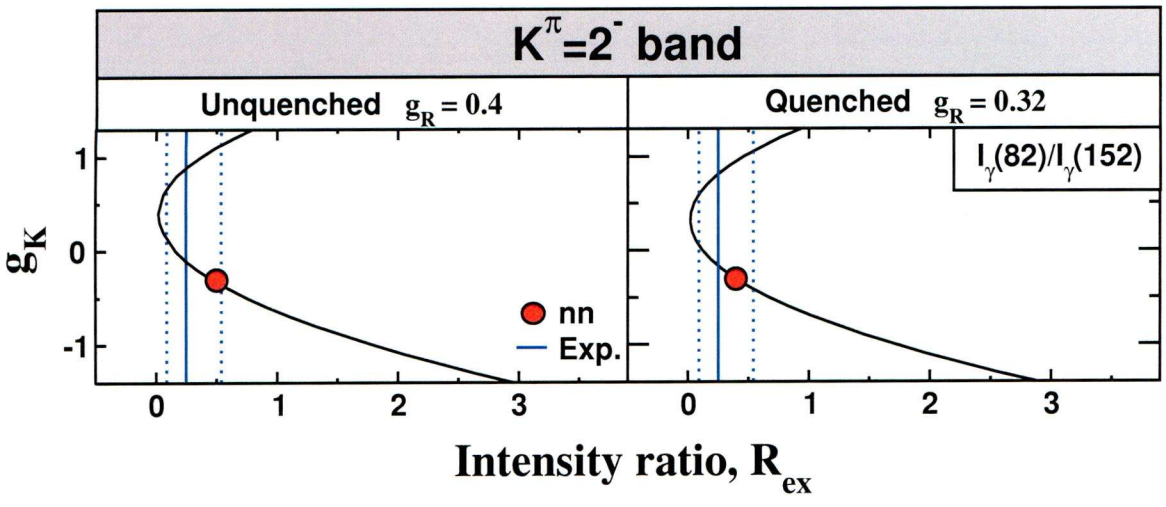

Figure 7.2: The relationship between intensity ratio, R_{ex}, and g_K, for the 7^- state of the $K^\pi=2^-$ band. Calculations are performed with g_R=Z/A=0.4 (left) and with a quenched value g_R=0.32(=0.8×Z/A) (right). Experimental result (blue lines) are compared to the $\frac{9}{2}^-[734]_\nu \otimes \frac{5}{2}^+[622]_\nu{}^{8-}$ configuration (red circles).

intensity ratios vary. For the $\frac{I(171)}{I(328)}$ ratio the error is large, corresponding to a large error on the 171 keV γ-ray intensity. There are also wide uncertainties in the $\frac{I(178)}{I(349)}$ ratio, due to the 178 keV γ-ray intensity error. Despite the errors, the three ratios show similar results. The unquenched experimental results show good agreement with the two-neutron excitation and the quenched results favour the two-neutron excitation over the two-proton. Therefore, experimental results indicate that $K^\pi=8^-$ band is formed by the neutron configuration $\frac{7}{2}^+[624]_\nu \otimes \frac{9}{2}^-[734]_\nu$.
There is only one two-quasiparticle excitation which would produce a $K^\pi=2^-$ band at such a low energy. Figure 7.2 shows the two experimental ratios that are measured for the $K^\pi=2^-$ band, compared with the $\frac{9}{2}^-[734]_\nu \otimes \frac{5}{2}^+[622]_\nu$. The experimental value shows good agreement with the two-neutron configuration, for both unquenched and quenched results the configuration result lies within the error bars. Although there is only one configuration for comparison with experimental data, the agreement between the two values is good. The band is expected to be formed by a mixing of an octupole vibration and a quasiparticle excitation, see

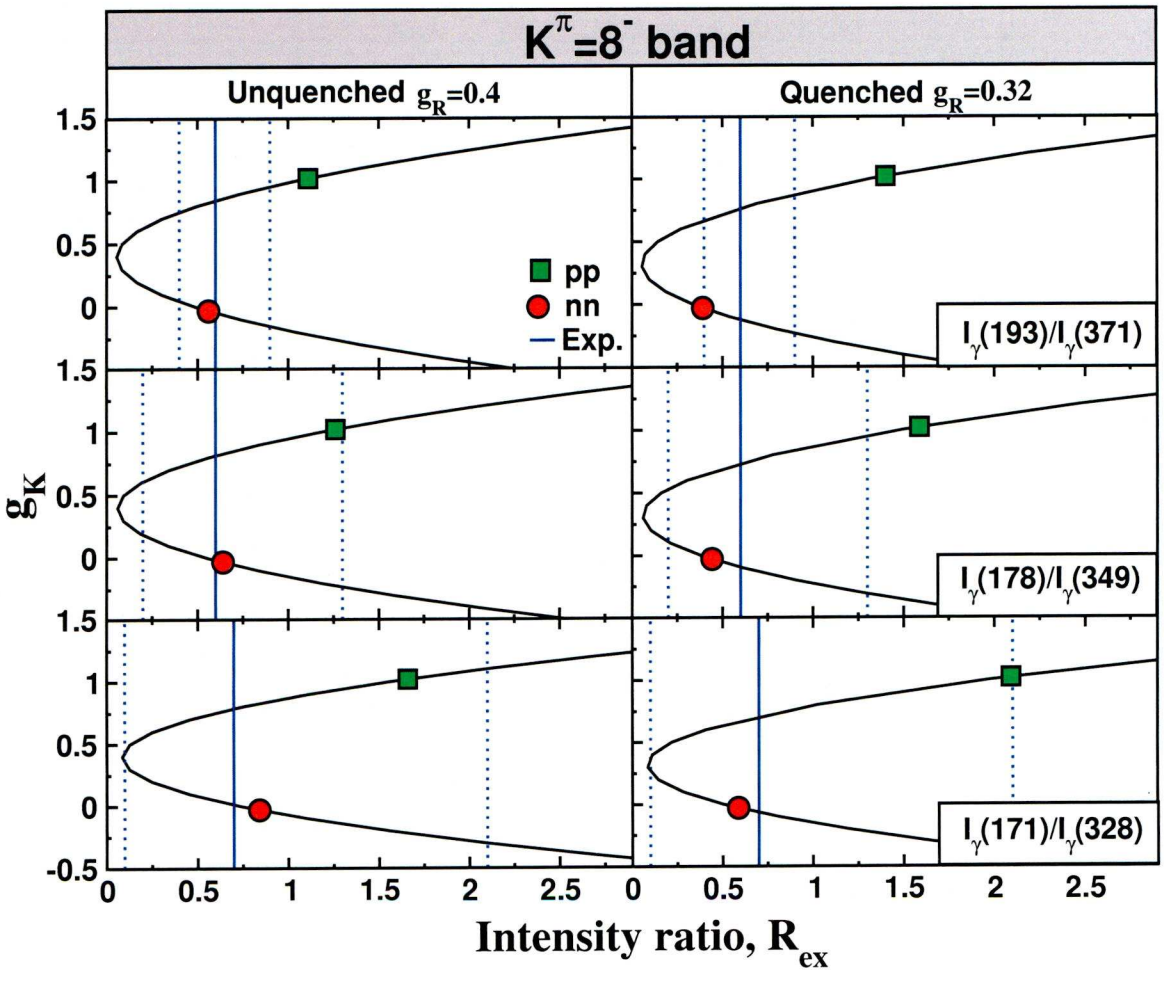

Figure 7.3: The relationship between intensity ratio, R_{ex}, and g_K, for the 16^-, 15^- and 14^- states of the $K^\pi=8^-$ band. Calculations are performed with g_R=Z/A=0.4 (left) and with a quenched value g_R=0.32(=0.8×Z/A) (right). Experimental results (blue lines) are compared to the $\frac{7}{2}^+[624]_\nu \otimes \frac{9}{2}^-[734]_\nu$ configuration (red circles) and the $\frac{7}{2}^-[514]_\pi \otimes \frac{9}{2}^+[624]_\pi$ configuration (green squares).

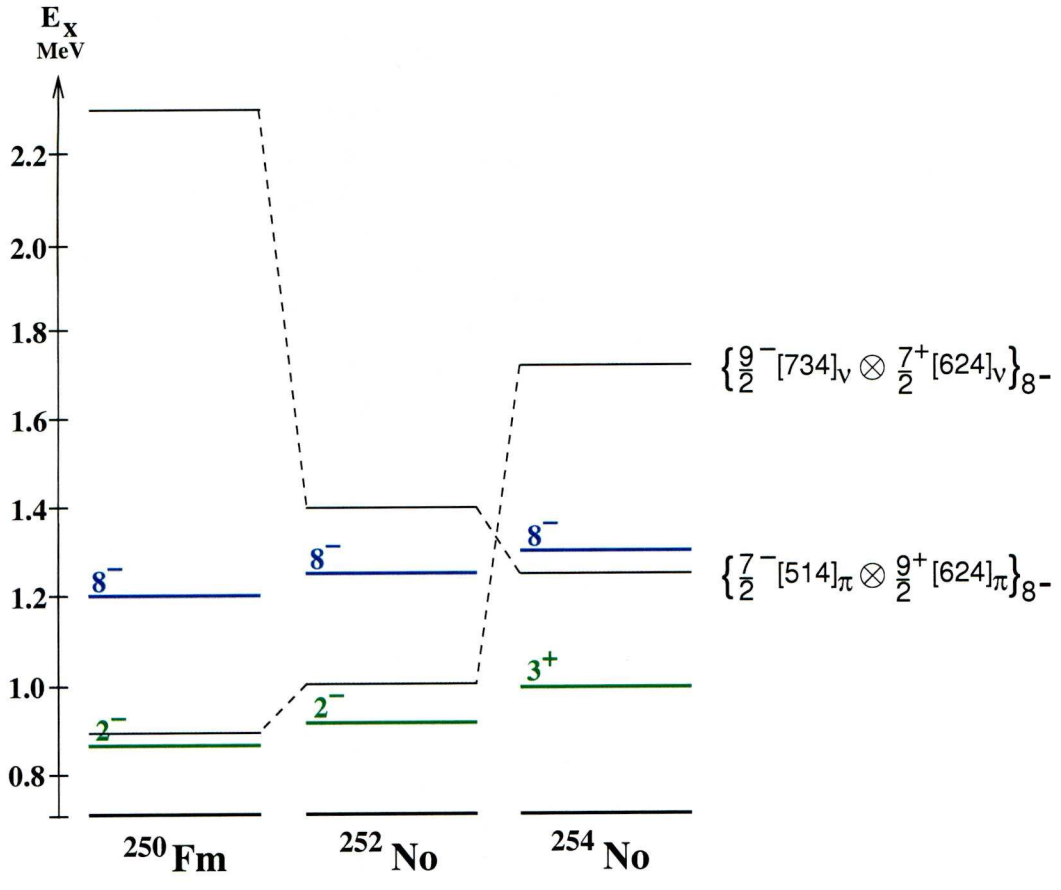

Figure 7.4: Comparison of experimental energies and two-quasiparticle excitation energies calculated for ^{250}Fm, ^{252}No and ^{254}No.

Section 3.2. The experimental results show that the 2^- band is dominated by the $\frac{9}{2}^-[734]_\nu \otimes \frac{5}{2}^+[622]_\nu$ quasiparticle excitation.

The excited bands of ^{250}Fm are formed by two-neutron quasiparticle states, as in ^{252}No and the other N=150 isotones. However, two-proton quasiparticle states are responsible for the excited bands of ^{254}No [He06, Ta06]. The reason for this difference can be understood using Figure 7.4, where the energies of the the excited bands observed in experiments are plotted for ^{250}Fm, ^{252}No and ^{254}No. The energies of the two-quasiparticle states, $\frac{7}{2}^+[624]_\nu \otimes \frac{9}{2}^-[734]_\nu$ and $\frac{7}{2}^-[514]_\pi \otimes \frac{9}{2}^+[624]_\pi$, are calculated using a Wood-Saxon potential and "Universal" parametrisation, for comparison with experimental values. Energies of the single-particle states, ϵ_{sp}, are calculated using *swbeta* [Ćw87] where the deformation parameters are taken

from [Ćw94]. The quasiparticle state energies, E_{qp}, can be determined using

$$E_{qp} = \sqrt{(\epsilon_{sp} - \lambda)^2 + \Delta^2} \tag{7.4}$$

where λ is the fermi energy and Δ is the pairing gap parameter, which is taken from [Mö97] and quenched by 0.6 to take into account the effect of blocking. The $K^\pi=8^-$ two-quasiparticle energies of ^{252}No and ^{254}No have been reproduced with 100 keV using this approach [Ro08, Ta06]. The calculated quasiparticle energies for $K^\pi=8^-$ states shown indicate that the two-neutron quasiparticle state lies at low energy for ^{250}Fm and ^{252}No, but with the addition of two neutrons, for ^{254}No, the energy increases dramatically. This implies there is large shell gap for deformed nuclei at Z=102. The similar increase in energy for the two-proton quasiparticle state between ^{252}No and ^{250}Fm implies a shell gap at N=152. Further evidence is found when comparing the experimental data of all the N=150 and N=152 isotones.

7.3 Systematic Comparisons

In Section 3.2, experimental results from the other N=150 isotones are discussed. All isotones, including ^{250}Fm, are found to have a low-lying $K^\pi=2^-$ band and a band with $K^\pi=8^-$. The energies of the bands are compared in Figure 7.5. The energies of the 8^- states of the N=150 isotones, across Z=94–102, vary by less than 100 keV. The 8^- states of the N=150 isotones are assigned as two-neutron quasiparticle excitations with configuration $\left\{\frac{7}{2}^+[624]_\nu \otimes \frac{9}{2}^-[734]_\nu\right\}^{8-}$, supported by the consistency of the 8^- energies.

The energies of the 2^- states observed in N=150 isotones are too low to be pure two-quasiparticle states. Instead these states are expected to have mixed origins with quasiparticle excitations and octupole vibrations. The analysis of g_K values performed in Section 7.2, indicates that the ^{250}Fm 2^- state is dominated by the $\frac{9}{2}^-[734]_\nu \otimes \frac{5}{2}^+[622]_\nu$ quasiparticle excitation. In Figure 7.5, it is noticed that the ^{248}Cf 2^- excited state is slightly lower in energy, this is due to both proton and neutron configurations contributing to 2^- octupole collectivity at Z=98. Other 2^-

states in the N=150 isotones have consistent energies, which supports the common origin of the states.

Whilst the excited states of N=150 nuclei are found to be caused by neutron quasiparticle excitations across a range of Z, the excited states of N=152 isotone ^{254}No are caused by proton excitations. The 8^- isomer discovered in ^{254}No has been attributed to the two-proton excitation $\frac{7}{2}^-[514]_\pi \otimes \frac{9}{2}^+[624]_\pi$ [He06, Ta06]. The configuration of the 3^+ state observed in ^{254}No has been identified as $\left\{\frac{1}{2}^-[521]_\pi \otimes \frac{7}{2}^-[514]_\pi\right\}^{3+}$ [He06, Ta06].

The difference between N=150 and N=152 isotones can be explained using Figure 7.6, where the single-particle energies for ^{250}Fm are calculated using a Wood-Saxon potential with "Universal" parameters [Ćw94]. The Fermi level (λ) for ^{250}Fm protons is located in the centre of a large shell gap at Z=100. On the other hand, the gap is smaller for neutrons and the neutron Fermi level passes close to the first unfilled orbital $\frac{9}{2}^-[734]$. Therefore, less energy is required to excite the neutrons than protons in ^{250}Fm. For the other N=150 isotones, mainly neutron

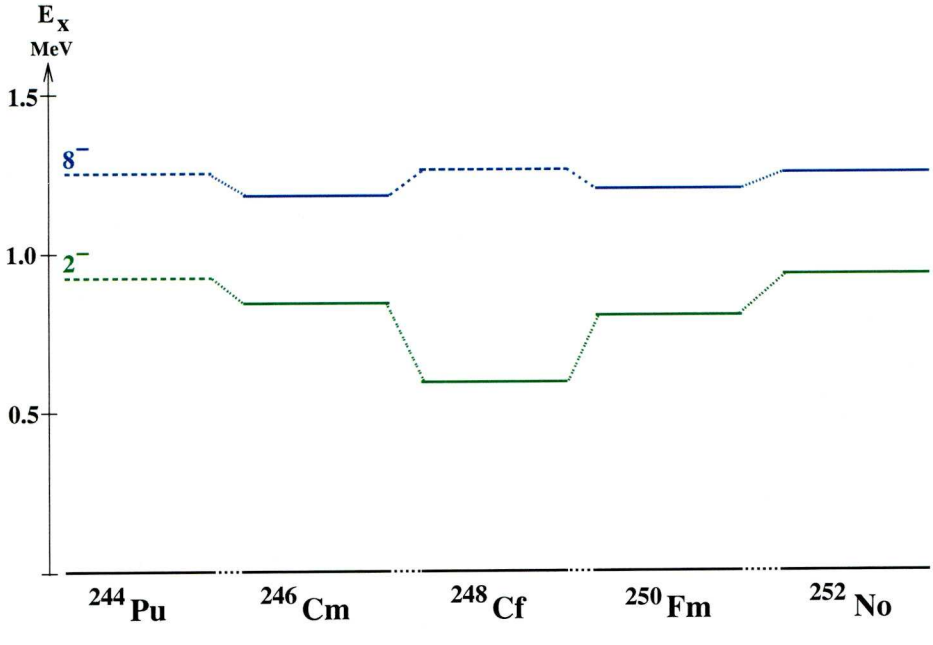

Figure 7.5: The excitation energies of K^π=2^- and 8^- states of the N=150 isotones. The dashed lines indicate that the energies are calculated and not measured.

excitations are observed due to the sparse distribution of the proton shells in comparison to the $\frac{9}{2}^-[734]$ and $\frac{7}{2}^+[624]$ neutron orbitals. For nuclei with N=152, the neutron shell gap becomes larger than the proton shell gaps. Therefore, proton quasiparticle excitations are more prevalent.

The experimental results suggest that shell closures for deformed nuclei occur at N=152, between the $\frac{9}{2}^-[734]$ and $\frac{1}{2}^+[620]$ orbitals, and at Z=100, between the $\frac{7}{2}^+[633]$ and $\frac{1}{2}^-[521]$ orbitals. Calculations using the Wood-Saxon potential predict the deformed shell gaps at N=152 and Z=100 and reproduce the experimental excitation energies for N=150 isomers [Ro08] and the ^{254}No isomer [Ta06]. Self-consistent mean-field models are less successful at reproducing experimental data, they predict shell closures at N=150 and Z=98,104 [De06, Ch06]. Figure 7.7 shows the single-particle diagrams for ^{250}Fm protons and neutrons, produced using Haretree-Foch-Bogolyubov (HFB) calculations with the Skyrme SLy4 interaction [Ch06]. To match the experimental results and create a shell gap for

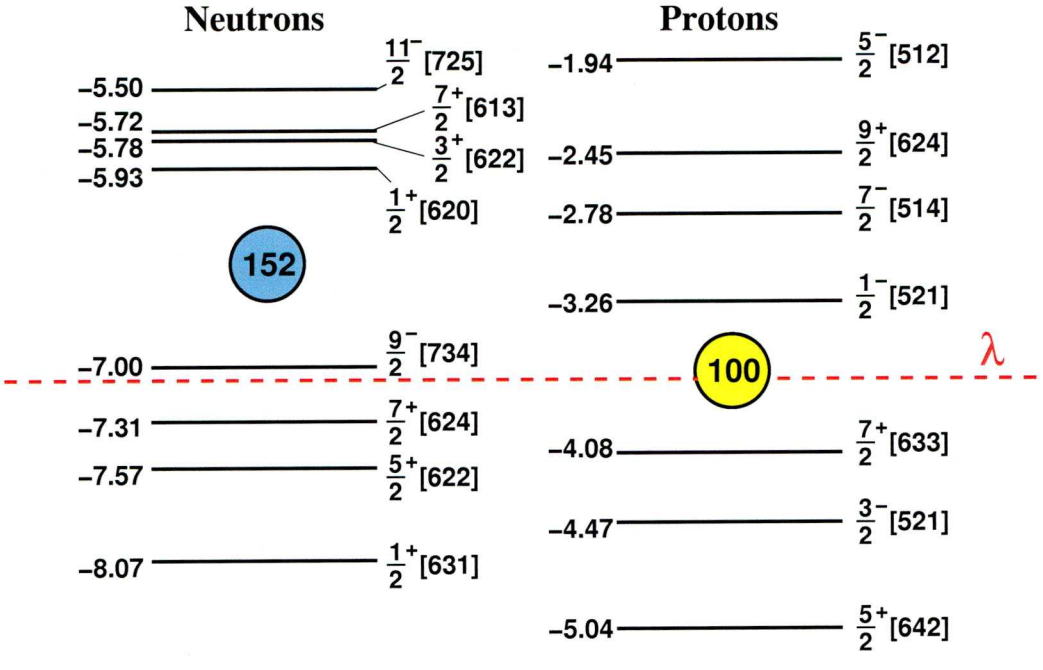

Figure 7.6: The single-particle energies calculated for ^{250}Fm using a Wood-Saxon potential with universal parameters.

neutrons at N=152, one could lower the energy of the $\frac{9}{2}^-[734]$ neutron orbital. Similarly for protons, the $\frac{9}{2}^+[624]$ orbital is too high in energy to reproduce the experimental energies of the ^{254}No 8^- isomer. Lowering the $i_{13/2^+}$ level would make the excitation energies closer to experimental values and would open up a shell gap at Z=100. The experimental results of ^{250}Fm and its neighbours highlight the deficiencies in the current nuclear models for the heavy and superheavy nuclei. It is hoped that the experimental data discussed here will instigate adjustments to the theoretical models and provide tests for their predictions.

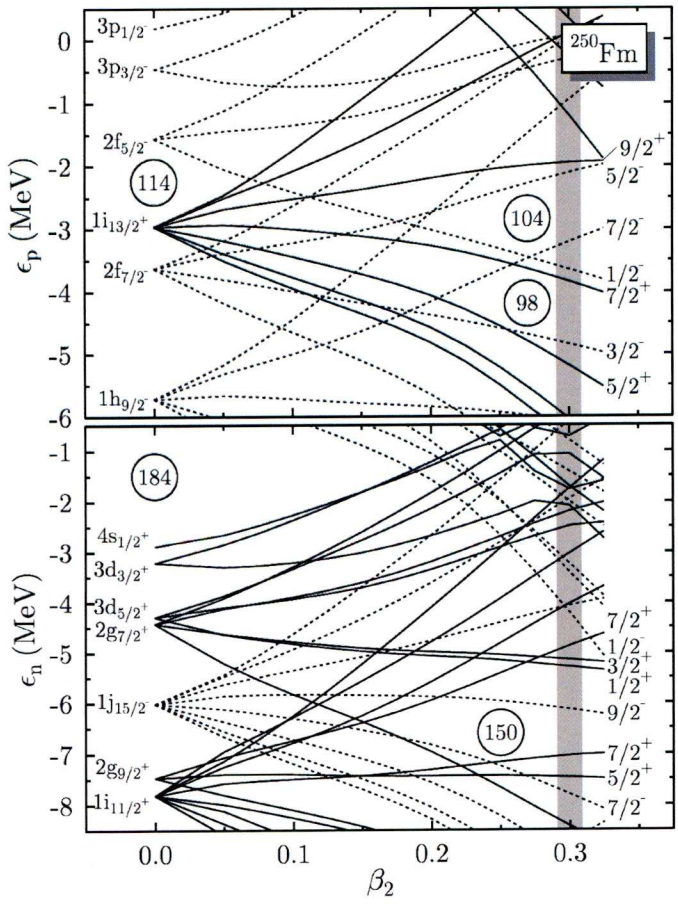

Figure 7.7: The single-particle diagrams of ^{250}Fm for protons (top) and neutrons (bottom) using HFB calculations with the Skyrme SLy4 interaction [Ch06]. The shaded band marks the deformation of the ^{250}Fm nucleus.

Chapter 8

Summary and Conclusion

Two excited bands and two isomers of ^{250}Fm have been identified using recoil-isomer tagging techniques. The 1.93(5) s isomer is found to be the band head of a $K^{\pi}=8^{-}$ band, which decays via an unobserved 22 keV transition to a $K^{\pi}=2^{-}$ side band (23%) and also decays directly to the ground-state band through a 682 keV transition (77%). Four in-band γ transitions are observed in the $K^{\pi}=2^{-}$ band, as well as the interband decays from the 2^{-} band to the ground-state band. One of the decays within the $K^{\pi}=2^{-}$ band is assumed to have E2 multipolarity, whilst the others are assumed to have dipole multipolarity. A signature-split rotational band is also observed, which is built on top of the 8^{-} isomer. Twelve decays observed in the 8^{-} band are assigned as E2 transitions, whilst three decays have mixed E2/M1 multipolarity. The intensity ratios of the different multipolarity γ decays are used to determine the g_K values of the $K^{\pi}=2^{-}$ and $K^{\pi}=8^{-}$ bands. The experimental values are compared to g_K values and intensity ratios calculated for single-particle configurations. The $K^{\pi}=2^{-}$ band is found to be dominated by the $\left\{\frac{9}{2}^{-}[734]_{\nu} \otimes \frac{5}{2}^{+}[622]_{\nu}\right\}^{2-}$ configuration, but can also be formed by a 2^{-} octupole vibration which accounts for the low-energy of the band. The experimental results for the 8^{-} band have led to the conclusion that it is formed by the $\left\{\frac{7}{2}^{+}[624]_{\nu} \otimes \frac{9}{2}^{-}[734]_{\nu}\right\}^{8-}$ configuration.

In comparing the new ^{250}Fm data to the N=150 isotones, from Z=94 to 102,

remarkable similarities are observed. Studies of ^{252}No, ^{248}Cf, ^{246}Cm and ^{244}Pu nuclei have found bands with $K^{\pi}=2^{-}$ and 8^{-}, at energies close to those observed in ^{250}Fm. In addition, isomers of ^{252}No and ^{246}Cm have been observed with γ decay structures closely resembling that found in ^{250}Fm. The consistent results for the N=150 nuclei support the conclusion that the $K^{\pi}=2^{-}$ and 8^{-} bands are caused by the same two-neutron quasiparticle excitations as ^{250}Fm. This is in contrast with the two-proton quasiparticle excitations of ^{254}No, which only differs from the N=150 isotone ^{252}No by two extra neutrons. Experimental data for N=152 isotones is growing, with excited states observed in ^{250}Cf and ^{248}Cm. The excited states of ^{252}Fm have not been studied as yet, a spectroscopic study would complete the N=152 systematic data. The experimental data across the N=150 and N=152 isotones indicates that shell gaps occur at N=152 and Z=100 for deformed nuclei. The ^{250}Fm analysis adds to the growing experimental information for this region, which informs the theoretical calculations for the deformed shell closures. The energies and single-particle assignments of the excited bands along with the new information about the isomers can be used as tests for theoretical studies. Furthermore, the systematic data not only aids the theories describing nuclei in the deformed region around the shell closures, but constrains the calculations for nuclei around the next spherical shell gaps.

Abbreviations

ADC	Analogue-to-Digital Converter
CFD	Constant-fraction discriminator
DSSD	The double-sided silicon strip detector
ECRIS	Electron Cyclotron Resonance Ion Source
GREAT	Gamma Ray Electron Alpha Tagging
HFB	Haretree-Foch-Bogolyubov
IC	Internal conversion
JYFL	The University of Jyväskylä Accelerator Laboratory
LDM	Liquid-drop model
MWPC	Multi-wire proportional counter
RDT	Recoil-decay tagging
RITU	Recoil Ion Transport Unit
SHN	Superheavy nuclei
TOF	The time-of-flight between detectors

Appendix A
Nilsson diagrams

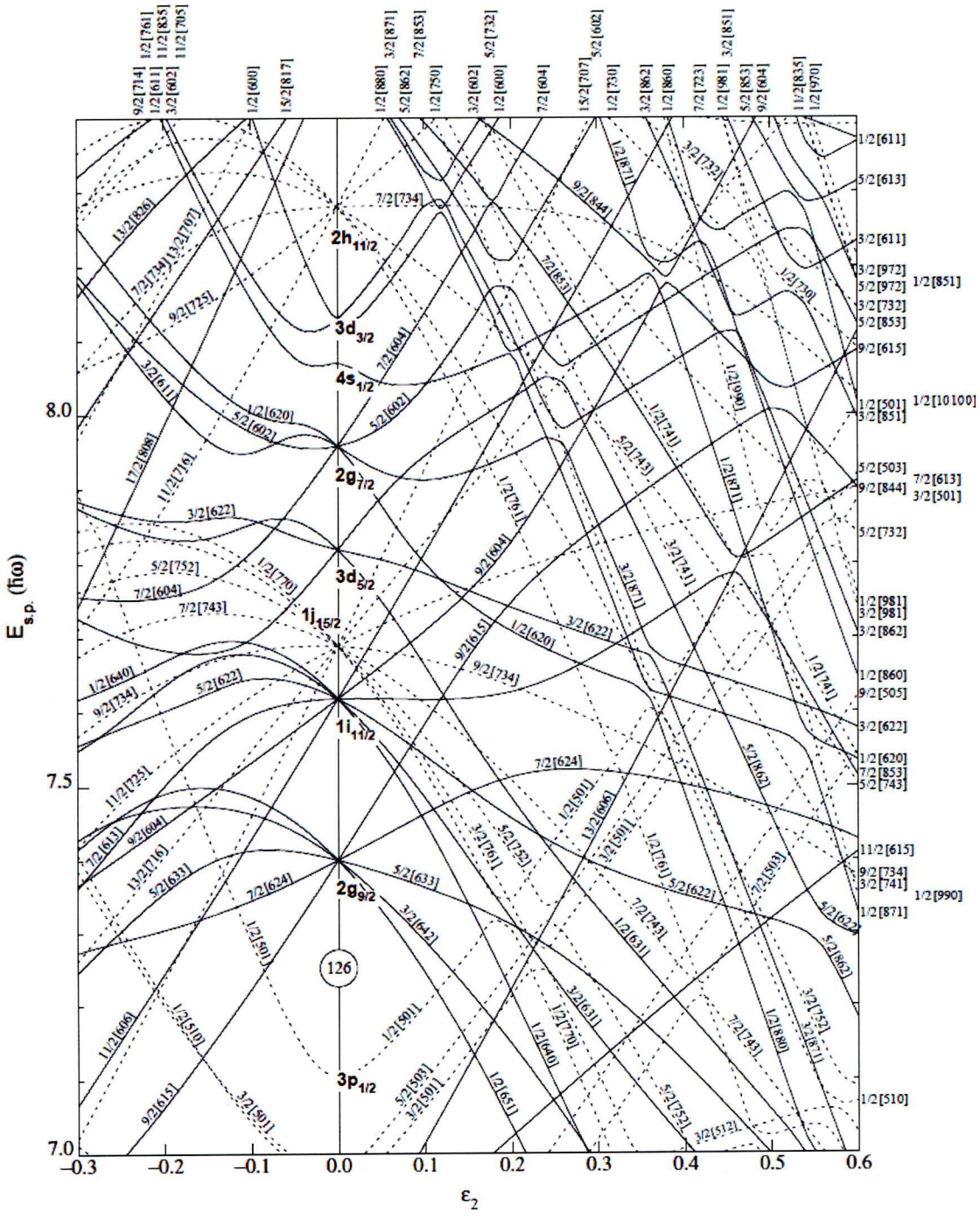

Figure 1: Nilsson diagram for neutrons, $N \geq 126$, taken from [Fi96].

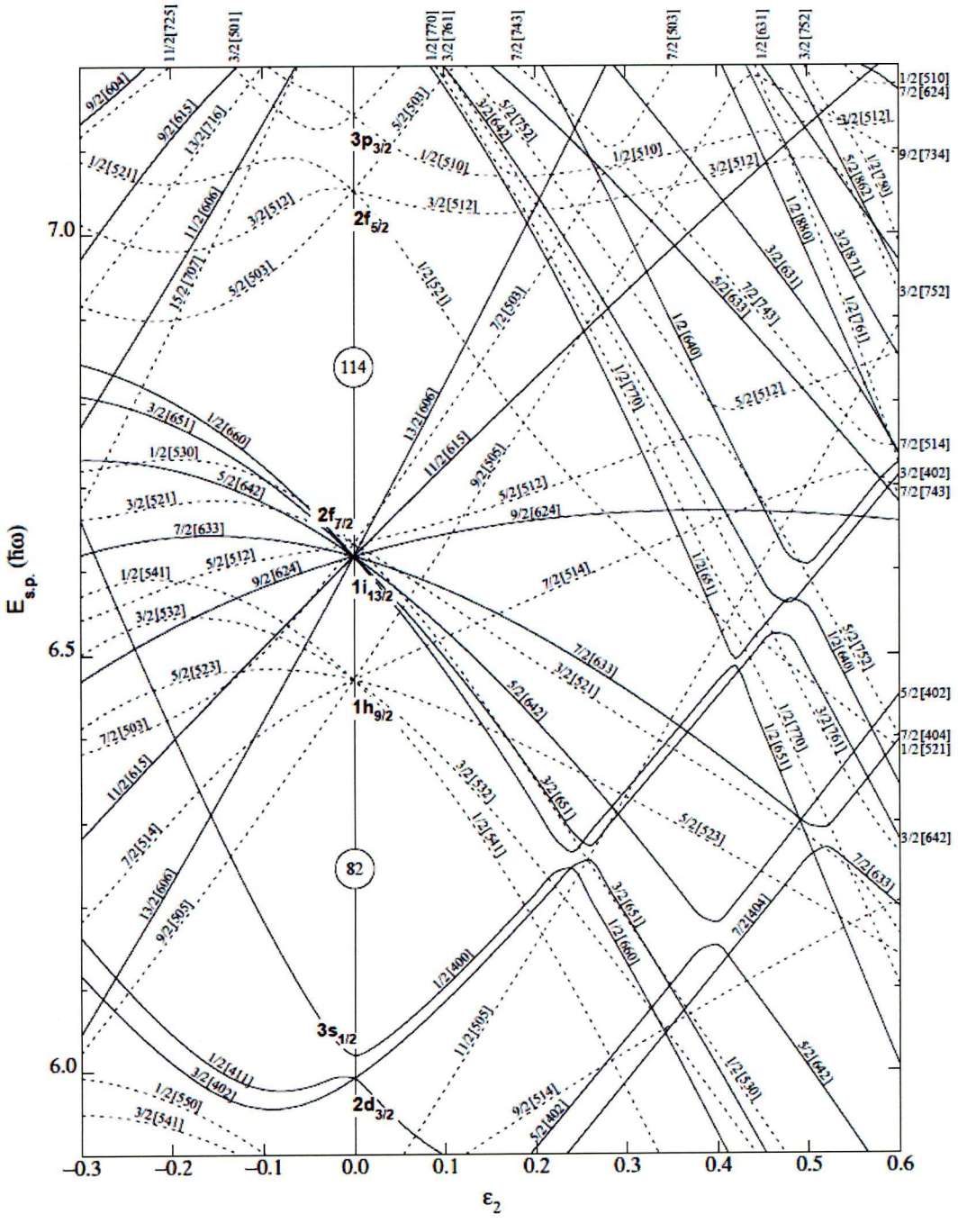

Figure 2: Nilsson diagram for protons, $Z \geq 82$, taken from [Fi96].

Bibliography

[Al55] G. Alaga, K. Alder, A. Bohr and B. R. Mottelson, "Intensity rules for beta and gamma transitions to nuclear rotational states", *Dan. Mat. Fys. Medd.* **29** (1955) 9

[An04] A. N. Andreyev *et al.*, "GEANT Monte Carlo simulations for the GREAT spectrometer", *Nucl. Instrum. Meth.* A **533** (2004) 422

[Ba06] J.E. Bastin *et al.*, "In-beam gamma ray and conversion electron study of ^{250}Fm", *Phys. Rev.* C **73** (2006) 24308

[Be01] M. Bender, W. Nazarewicz, P.-G. Reinhard, "Shell stabilization of super- and hyperheavy nuclei without magic gaps", *Phys. Lett. B* **515** (2001) 42

[Bo99] A. Bohr and B. R. Mottelson, "Nuclear Structure Volume II", *World Scientific* (1999)

[Bu96] P. A. Butler *et al.*, "Conversion Electron Cascades in ^{254}No", *Phys. Rev. Lett.* **89** (2002) 202501

[Ch06] A. Chatillon *et al.*, "Spectroscopy and single-particle structure of the odd- Z heavy elements ^{255}Lr, ^{251}Md and ^{247}Es", *Eur. Phys. J.* A **30** (2006) 397

[Ćw94] S. Ćwiok, S. Hofmann and W. Nazarewicz, "Shell structure of the heaviest elements", *Nucl. Phys.* A **573** (1994) 356

[Ćw96] S. Ćwiok et al., "Shell structure of the superheavy elements", *Nucl. Phys.* A **611** (1996) 211

[Ćw87] S. Ćwiok, J. Dudek, W. Nazarewicz, J. Skalski and T.Werner, "Singleparticle energies, wave functions, quadrupole moments and g-factors in an axially deformed woods-saxon potential with applications to the two-centre-type nuclear problems", *Comp. Phys. Comm.* **46** (1987) 379

[De06] J.-P. Delaroche *et al.*, "Structure properties of even-even actinides at normal and super deformed shapes analysed using the Gogny force", *Nucl. Phys.* A **771** (2006) 103

[Dö83] F. Dönau and S. Frauendorf, "High angular moment properties of nuclei", *Proceedings of the Conference on High Angular Momentum Properties of Nuclei, Oak Ridge, 1982*, edited by N. R. Johnson (Harwood Academic, New York, 1983) p. 143

[Dö87] F. Dönau, "Electromagnetic radiation of rotating nuclei", *Nucl. Phys.* A **471** (1987) 469

[Ej89] H. Ejiri and M. J. A. de Voigt, "Gamma-ray and electron spectroscopy in nuclear physics", *Oxford University Press* (1989)

[Fi96] R. B. Firestone, "Table of Isotopes 8th edition", *John Wiley and Sons Inc.* (1996)

[Gh71] A. Ghiorso *et al.*, "Defence of the Berkeley work on alpha-emitting isotopes of element 102", *Nature* **229** (1971) 603

[Gh73] A. Ghiorso *et al.*, "Isomeric States in ^{250}Fm and ^{254}No", *Phys. Rev.* C **7** (1973) 2032

[Gr08] C. Gray-Jones, "Isomer Spectroscopy of ^{254}No", *University of Liverpool, PhD thesis* (2008)

[Gr04] P. T. Greenlees *et al.*, "In-beam spectroscopy at the RITU gas-filled recoil separator", *Eur. Phys. J.* A **20** (2004) 87

[Gr09] P.T. Greenlees *et al.*, "High-K Structure in ^{250}Fm and the Deformed Shell Gaps at N=152 and Z=100", *Phys. Rev.* C **78** (2008) 2

[Ha89] H. L. Hall *et al.*, "Beta-delayed fission from Es-256(M) and the level of Fm-256", *Phys. Rev.* C **39** (1989) 1866

[Ha63] P. G. Hansen, K. Wilsky, C. V. K. Baba and S. E. Vandenbosch, "Decay of an isomeric state in Cm244", *Nuc. Phys.* **45** (1963) 410

[He06] R.-D. Herzberg *et al.*, "Nuclear isomers in superheavy elements as stepping stones towards the island of stability", *Nature* **442** (2006) 896

[He08] R.-D. Herzberg and P. T. Greenlees, "In-beam and decay spectroscopy of transfermium nuclei", *Progress in Particle and Nuclear Physics* **61** (2008) 674

[Ho84] R. W. Hoff *et al.*, "Levels of ^{244}Cm populated by the beta decay of 10-h ^{244}Am^{g} and 26-min ^{244}Am^{m}", *Phys. Rev.* C **29** (1984) 618

[Ho01] S. Hofmann *et al.*, "The new isotope (270)110 and its decay products (266)Hs and (262)Sg", *Euro. Phys. J.* A **10** (2001) 5

[Jo02] G.D. Jones, "Detection of long-lived isomers in super-heavy elements", *Nucl. Instrum. Meth.* A **488** (2002) 471

[Ka08] K. Katori, I. Ahmad and A. M. Freidman, "Two-quasineutron states in Cf-248(98) and Cf-250(98) and the neutron-neutron residual interactions", *Phys. Rev.* C **78** (2008) 014301

[Ki08] T. Kibdi *et al*, "Evaluation of theoretical conversion coefficients using BrIcc", *Nucl. Instrum. Meth.* A **589** (2008) 202

[Kr88] K. S. Krane, "Introductory Nuclear Physics", *John Wiley & Sons* (1988)

[La01] I. H. Lazarus *et al.*, "The GREAT triggerless Total Data Readout method", *IEEE Transactions on Nuclear Science* **48** (2001) 567

[Le95] M. Leino, "Gas-filled recoil separator for heavy element studies", *Nucl. Instrum. Meth.* B **99** (1995) 653

[Le97] M. Leino, "In-flight separation with gas-filled systems", *Nucl. Instrum. Meth.* B **126** (1997) 320

[Lo68] K. E. G. Löbner, "Systematics of absolute transition probabilities of K-forbidden gamma-ray transitions", *Phys. Let.* B **26** (1968) 369

[Ma49] M. G. Mayer, "On closed shells in nuclei. II", *Phys. Rev.* **75** (1949) 1969

[Mo87] K. J. Moody *et al.*, "New nuclides: neptunium-243 and neptunium-244", *Z. Phys.* A **328** (1987) 417

[Mö97] P. Möller, J. R. Nix and K.-L. Kratz, "Nuclear properties for astrophysical and radioactive-ion-beam applications", *At. Nuc. Dat. Tab.* **66** (1997) 131

[Mu76] L. G. Multhauf *et al.*, "Collective excitations in Cm-246 and decay of Am-246(M)", *Phys. Rev.* C **13** (1976) 2

[Ne70] K. Neergärd and P. Vogel, "On microscopic description of nuclear vibrations when phonons occur at relatively low energy octupole states of even deformed nuclei with a greater than or equal to 222", *Nucl. Phys.* A **149** (1970) 217

[Ni55] S G. Nilsson, Dan. Mat. Fys. Medd. **29**, 16 (1955)

[Ni69] S. G. Nilsson *et al.*, "On nuclear structure and stability of heavy and superheavy elements", *Nucl. Phys.* A **131** (1969) 1

[No94] P. J. Nolan, F. A. Beck and D. B. Fossan, "Arrays of Escape-Suppressed Gamma-Ray Detectors", *Ann. Rev. Nucl. Part. Sci.* **45** (1994) 561

[Og06] Yu. Ts. Oganessian *et al.*, "Synthesis of the isotopes of elements 118 and 116 in the Cf-249 and Cm-245+Ca-48 fusion reactions", *Phys. Rev.* C **74** (2006) 9

[Pa03] R.D. Page *et al.*, "The GREAT spectrometer", *Nucl. Instrum. Meth.* B **204** (2003) 634

[Pe06] D. Peterson *et al.*, "Decay modes of ^{250}No", *Phys. Rev.* C **74** (2006) 014316

[Pa95] E. S. Paul *et al.*, "In-beam γ-ray spectroscopy above ^{100}Sn using the new technique of recoil decay tagging", *Phys. Rev. C* **51** (1995) 78

[Pa09] E. S. Paul, *private communication*, esp@ns.ph.liv.ac.uk

[Pr06] A. Pritchard, *University of Liverpool, PhD Thesis* (2006)

[Ra07] P. Rahkila, "Grain - A Java Analysis Framework for Total Data Readout", *Nucl. Instrum. Meth.* A **595** (2008) 637

[Ri80] P. Ring and P. Schuck, "The Nuclear Many-Body Problem", *Springer-Verlag Inc.* (1980)

[Ro08] A. P. Robinson *et al.*, "$K^{\pi}=8^{-}$ isomers and $K^{\pi}=2^{-}$ octupole vibrations in N = 150 shell-stabilized isotones", *Phys. Rev.* C **78**, 034308 (2008)

[Se05] D. A. Seddon, private communication, das@ns.ph.liv.ac.uk

[TD09] Website: *http : //npg.dl.ac.uk/GREAT/Technical_Description.pdf*

[St68] V. M. Strutinsky, "Shells in deformed nuclei", *Nucl. Phys.* A **122** (1968) 1

[Su07] B. Sulignano *et al.*, "Identification of a K isomer in No-252", *Eur. Phys. J.* A **33** (2007) 327

[Su08] Y. Sun, G.-L. Long, F. Al-Kudair and J. A. Sheikh, "γ-vibrational states in superheavy nuclei", *Phys. Rev.* C **77**, (2008) 044307

[Ta06] S. K. Tandel *et al.*, "K Isomers in ^{254}No: Probing Single-Particle Energies and Pairing Strengths in the Heaviest Nuclei", *Phys. Rev. Let.* **97** (2006) 082502

[Ta09] U. Tandel *et al.*, *in preparation.*

[Th93] J. Theuerkauf, S. Esser, S. Krink, M. Luig, N. Nicolay, O. Stuch and H. Wolters, *Institute for Nuclear Physics, Cologne* (1993)

[Th75] R. C. Thompson, J. R. Huizenga and Th. W. Elze, "Collective states in ^{230}Th, ^{240}Pu, ^{244}Pu and ^{248}Cm excited by inelastic deuteron scattering", *Phys. Rev.* C **12** (1975) 1227

[To49] C. H. Townes, H. M. Foley and W. Low, "Nuclear quadrupole moments and nuclear shell structure", *Phys. Rev.* **76** (1949) 1415

[Wa99] P. Walker and G. Dracoulis, "Energy traps in atomic nuclei", *Nature* **399** (1999) 6731

[Wa05] P. M. Walker,"High-K structures under extreme conditions", *Acta Physica Polonica* B **36** (2005) 4

[Wa94] P. M. Walker, G. D. Dracoulis, A. P. Byrne, T. Kibédi and A. E. Stuchbery, "$K^{\pi}=6^{+}$ and 8^{-} isomer decays in Hf-172 and ΔK=8 E1 transition rates", *Phys. Rev.* C **49** (1994) 3

[We51] Weisskopf, V. F., "Radiative transition probabilities", *Phys. Rev.* **83** (1951) 1073

[Xu04] F. R. Xu, E. G. Zhao, R. Wyss and P. M. Walker, "Enhanced stability of superheavy nuclei due to high-spin isomerism", *Phys. Rev. Lett.* **92** (2004) 25

[Ya75] S. W. Yates *et al.*, "Particle-phonon interactions in ^{248}Cf and ^{249}Cf", *Phys. Rev.* C **12** (1975) 2